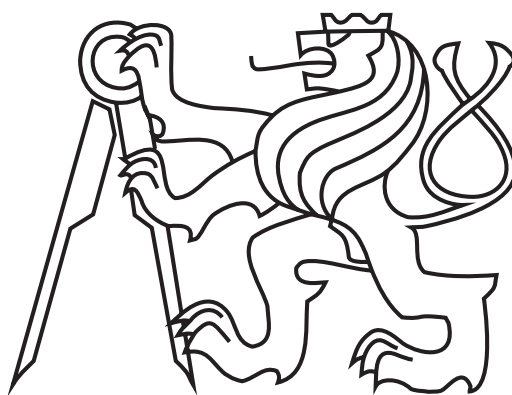


CZECH TECHNICAL UNIVERSITY IN PRAGUE



DISSERTATION THESIS

Czech Technical University in Prague
Faculty of Nuclear Sciences and Physical Engineering
Department of Physics

Mitja Majerle

**Monte Carlo methods
in spallation experiments**

Dissertation Thesis

Prague, 2009

Declaration

I confirm that this dissertation thesis was done in the internal and combined forms of postgradual study at the Department of Physics at the Faculty of Nuclear Sciences and Physical Engineering at Czech Technical University in Prague. This thesis is the result of my own work unless explicit references are made to the work of others; it has not been submitted for another qualification to this or any other university.

Aspirant: **Mitja Majerle**

Postgradual study program: Application of Natural Sciences

Study field: Nuclear Engineering

Supervisor: **RNDr. Vladimír Wagner, CSc.**

Affiliation: Department of Nuclear Spectroscopy

Nuclear Physics Institute

Academy of Sciences of the Czech Republic

public research institution

250 68 Řež near Prague

Acknowledgments

At first I have to thank my excellent supervisor and teacher Vladimir and my colleagues Antonin and Ondřej for their help and support during my studies, even more for their friendship and atmosphere in our "team". I am grateful also to our whole department for welcoming me so well and for being such a great department.

Something that I will always remember from Prague are the years that I spent in our dormitory and all the friends from there, especially my roommate Dragan with our common friend Dostojevski. And of course - Martina.

And finally, I would like to dedicate this dissertation to my parents for their hope that I would once finish it.

I am grateful to all colleagues of the Energy Plus Transmutation collaboration for cooperation during experiments and for sharing their ideas.

This work was carried out under support of the Grant Agency of the Czech Republic (grant No. 202/03/H043) and under support of the Grant Agency of the Academy of Sciences of the Czech Republic (grant No. K2067107).

The access to the METACentrum computing facilities provided under the research intent MSM6383917201 is appreciated.

Abstract

In the frame of international projects spallation experiments are performed at the Joint Institute of the Nuclear Research in Dubna. The experiments with relativistic protons (\approx GeV) directed to thick targets are mainly focused on the research of the transmutation capabilities of spallation neutrons, but they also provide valuable data for benchmark tests of different spallation codes.

In this work, Monte Carlo codes MCNPX and FLUKA are used to simulate two experimental setups (Phasotron and Energy Plus Transmutation). The influence of uncertainty in experimental parameters on the results is studied exploiting simulations, and the usability of the experimental data as benchmark tests is discussed.

Keywords:

spallation reactions, accelerator driven transmutation of nuclear waste, Monte Carlo simulations, MCNPX, FLUKA

PACS:

- 25.40.Sc
- 28.65.+a
- 24.10.Lx

Abstrakt

V rámci mezinárodních projektů se ve Spojeném ústavu jaderných výzkumů Dubna provádějí experimenty studující tříštivé reakce. Experimenty s relativistickými protony (\approx GeV) dopadajícími na tlusté olovené terče jsou především zaměřeny na výzkum transmutačních schopností spalačních neutronů. Poskytují však také užitečná data pro testování různých simulačních programů.

V této práci jsou využity Monte Carlo programy MCNPX a FLUKA k simulování dvou experimentálních sestav (Phasotron a Energy Plus Transmutation). Simulace jsou používány ke studiu vlivu neurčitostí experimentálních parametrů na výsledky a užitečnosti naměřených dat pro benchmark testy.

Contents

Introduction	1
1 Overview	3
1.1 Accelerator driven systems (ADS)	4
1.1.1 Spallation	4
1.1.2 Accelerator	7
1.1.3 Subcritical reactor	8
1.2 Experimental ADS	8
1.2.1 European research	8
1.2.2 Research outside Europe	10
1.2.3 Russian research	11
1.3 Simulations	13
1.3.1 Spallation reaction	15
1.3.2 High energy cross-section libraries	18
1.3.3 MCNPX	18
1.3.4 FLUKA	19
1.3.5 TALYS	20
1.4 Motivation for Dubna ADS experiments and this work	20
2 Neutron activation analysis	23
2.1 The production and detection of radioisotopes	24
2.2 Detection of radioisotopes	26
2.2.1 Experimental calibration	28
2.2.2 Full peak efficiency - $\epsilon_P(E)$	28
2.2.3 Total efficiency - $\epsilon_T(E)$	30
2.2.4 Geometrical correction factor - C_g	31
2.2.5 Self-absorption of gamma photons in the activation foils - C_s	33
2.2.6 Cascade coincidences	34
2.3 Production of radioisotopes	38
2.3.1 Spectra of produced particles and cross-sections	38

2.3.2	Influence of other particles	40
2.3.3	Dimensions of the foils	40
3	Phasotron experiment	47
3.1	Experimental setup and results	47
3.1.1	Experimental setup	47
3.1.2	Experimental data - beam parameters	49
3.1.3	Experimental data - spatial distribution of neutron field	50
3.1.4	Experimental data - transmutation of iodine	52
3.2	Simulations - systematic uncertainties of experimental results .	52
3.2.1	Influence of the setup parts and experimental conditions	53
3.3	Simulations - comparison of code predictions with experimen-	
	tal results	59
3.3.1	Determination of beam parameters by simulations	59
3.3.2	Simulations of neutron fluences in foils on top of setup	60
3.3.3	Simulations of neutron fluences in iodine samples	64
4	Energy Plus Transmutation	67
4.1	Experimental setup	68
4.2	Simulation procedure	70
4.3	Influence of setup parts and experimental conditions	71
4.3.1	Polyethylene box and cadmium layer	71
4.3.2	Other setup parts (metal parts, wood)	73
4.3.3	Activation foils	75
4.3.4	Beam parameters	76
4.4	Isotope production in reactions with protons, pions and photons	77
4.5	Parameters of simulations: Effects of different physics models	
	and cross-section libraries	78
4.6	Global characteristics of EPT	79
4.7	Comparison of experimental data and simulation results	80
5	Summary	85
5.1	Simulations for gamma spectroscopy	85
5.2	Simulations of simple lead target	86
5.3	Simulations of complex setup	87
	Bibliography	89
	Appendix	95

Introduction

With new inventions in accelerator technologies, spallation process is being reconsidered as an intensive source of neutrons. Apart from using spallation neutrons in basic research, some decades old idea of transmuting nuclear waste and catalyzing nuclear reactions is actual again - Accelerator Driven Systems. Computer Monte Carlo simulations are the essential part at the design of spallation sources and experiments. The spallation process and subsequent high energy neutron transport are not yet studied in detail, and the computer codes are still under development.

The research on ADS is performed worldwide and covers topics from neutron distribution measurements to accelerator and target research. Important spallation experiments on thick targets are performed also in the Joint Institute for Nuclear Research in Dubna (JINR), Russia. Our group, one of the participants in the experiments, uses neutron activation detectors to obtain data about spatial distribution of produced neutrons, and provides Monte Carlo simulations of the experiments.

So far, the systematical uncertainty of the spallation experiments and of our experimental method have not been properly studied. This work presents some of our experimental results (for two different setups) and offers detailed studies of accuracy of the results with the help of Monte Carlo codes MCNPX and FLUKA.

The first part of this work is dedicated to the studies of the neutron activation method which was used for the measurements of neutron fluxes at experiments. Different aspects of this method (systematic uncertainty, usability, reliability) are studied with the help of MCNPX and FLUKA simulations.

The experimental and computational studies of two experiments with relativistic protons directed to thick targets are presented in the next two parts: Phasotron and Energy plus Transmutation experiments.

The first one is the experiment with 660 MeV protons directed to a bare, lead target, realized in the Laboratory of Nuclear Problems of the Joint Institute for Nuclear Research Dubna in December, 2003. Produced spalla-

INTRODUCTION

tion neutrons were probed with small activation detectors at different places around the target. Monte Carlo codes MCNPX and FLUKA were used to study the systematic uncertainties and to predict the experimental results. Both codes described successfully most of the experimental results.

The Energy plus Transmutation setup consists of a lead target with the surrounding subcritical uranium blanket. The target was irradiated with relativistic protons (0.7-2 GeV) and deuterons (1.6 and 2.52 GeV). The analysis of the systematic uncertainties and the prediction of the experimental results performed with MCNPX and FLUKA codes are presented, together with comparisons with some experimental results.

Chapter 1

Overview

The long term hazard of radioactive waste arising from nuclear energy production is a matter of continued discussion and public concern in many countries. By the use of partitioning and transmutation of the actinides and some of the long lived fission products, the radiotoxicity of the high level waste and, possibly, the safety requirements for its geologic disposal, can be reduced compared with the current once through fuel cycle. To make the technologically complex enterprise worthwhile, a reduction in the high level waste radiotoxicity by a factor of at least one hundred is desirable. This requires very effective reactor and fuel cycle strategies, including fast reactors and/or accelerator driven systems (ADS) - systems with a high power accelerator of middle energy (few hundreds MeV) coupled with the spallation target. Such setup offers an alternative method of the neutron production in the spallation process.

In the recent years, the world has registered obvious progress in the accelerator technique. The successful functioning of several high energy research accelerators (Berkeley, KEK), the construction of the LHC, etc. brought new technologies also to mid, and low energy accelerators. Advances like superconductivity for magnets and RF cavities, ion sources, etc. have led to the practical realization of high power beams.

Spallation neutrons have also huge potential in research, health service or material modifications. There are several projects related to the construction of the spallation sources for research (SNS [1], ESS [2]) and the production of medicine radioisotopes [3].

From the theoretical point of view, the description of the spallation and subsequent processes exists for many decades [4]. They are implemented in Monte Carlo codes, which are computational algorithms that rely on repeated random sampling to compute their results. The predictions of such codes show that the models describe the results of simple experiments with thin

and thick targets quite well (within 50% accuracy), but, for complex and expensive ADS systems better prediction accuracy will be necessary.

1.1 Accelerator driven systems (ADS)

The idea of the ADS was reborn in 90's with articles of C.D.Bowman and C.Rubbia, who independently proposed a new approach to the problems of radioactive waste and limited uranium resources: to introduce extra neutrons produced in spallation reaction to the core of the subcritical reactor (Fig. 1.1). They discussed this idea in two articles, C.D.Bowman in year 1992 [5] and C.Rubbia in year 1993 [6]. The main idea of their approach is to direct an intensive, relativistic proton beam to a heavy metal target, where tens of neutrons per one proton are produced in the spallation reaction. Spallation target is placed in a subcritical reactor core, where extra neutrons are used for sustaining the chain reaction, transmuting radioactive waste to short-lived and stable isotopes and breeding the fuel from ^{238}U , ^{232}Th and other isotopes. Heat from the reactor is used to produce energy, part of this energy (ca. 30%) is used to power the accelerator, and part (ca. 70%) can be sent to the electric grid - the cycle is closed. The articles are different in some technical details, Bowman suggested a thermal reactor, on the other hand, Rubbia considered fast reactor to suit better transmutation purposes, however, both demand a special accelerator, which is today the main obstacle in realizing the ADS technology. Apart from the accelerator (or possibly another intensive high energy neutron source), the detailed studies of spallation reactions and transport of neutrons of energies >20 MeV are needed.

1.1.1 Spallation

Spallation is a nuclear reaction that can take place when two nuclei collide at very high energy (typically 500 MeV per nucleon and up), in which the involved nuclei are either disintegrated into their constituents (protons and neutrons), light nuclei, and elementary particles, or a large number of nucleons are expelled from the colliding system resulting in a nucleus with a smaller atomic number (Fig. 1.2). A spallation reaction can be compared to a glass that shatters in many pieces when it falls on the ground. The way how the kinetic energy is distributed over the different particles involved in a spallation reaction is otherwise well understood, but from the point of view of the ADS the spallation process is not described enough accurately.

In the frame of the ADS, the spallation reaction in heavy nuclei (lead, bismuth) serves as the source of neutrons - proton with 1 GeV energy impinging

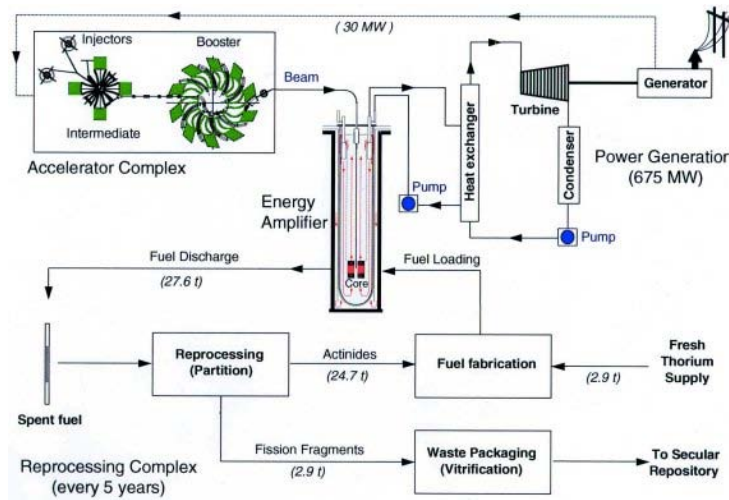


Figure 1.1: Closing the nuclear cycle with the Energy Amplifier, a sub-critical device with a $\text{Th-}^{233}\text{U}$ fissile core fed with a supply of spallation neutrons. There is no criticality, no plutonium and no problem of actinide waste. At the end of the cycle, ^{233}U and the other uranium isotopes are recycled to serve as the initial fissile part of a new load of fuel. Thorium is an abundant resource (much more than uranium) and supplies could last thousands of years [7].

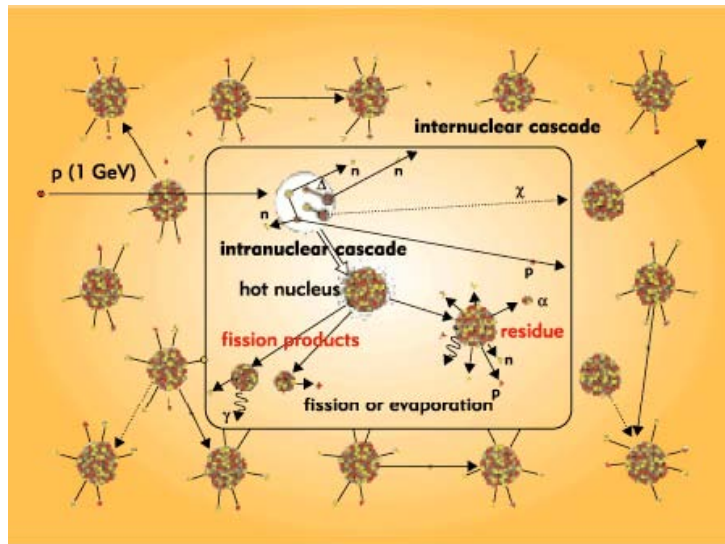


Figure 1.2: Representation of the spallation process caused by a proton interacting with heavy nuclei [8].

to a thick target of Pb-Bi alloy produces ca. 30 neutrons in spallation.

Phases of the spallation reaction

Spallation is usually described as a two-step reaction:

- The intranuclear cascade

One can consider that the first step of the reaction consists in individual collisions between the nucleons. The wavelength $\frac{\lambda}{2\pi}$ of an incoming nucleon with few hundreds of MeV is about 10^{-14} cm and thus smaller than the distance between nucleons which is about 1 fm = 10^{-13} cm. The incoming nucleon "sees" the substructure of the nucleus, i.e. a bundle of nucleons.

The interaction leads to the ejection of some of the nucleons and to the excitation of the residual nucleus which will cool down in the next step. The typical duration of the intranuclear cascade is 10^{-22} sec.

- The deexcitation

When the last nucleon has been ejected in the intranuclear cascade, the nucleus is being left in an excited state. The deexcitation of the residual nucleus can proceed in two main ways: evaporation and fission. The typical duration of the deexcitation process is 10^{-16} sec.

Evaporation is the dedicated deexcitation mode for non or hardly fissile nuclei which have been excited above the energy required for the separation of one neutron. In this case, the excited nucleus emits nucleons or light nuclei such as D, T, ^3He , α , Li, Be, etc.

Fission is the second important deexcitation channel. During the fission process, the nucleus changes its shape to reach firstly the so called saddle point at which the fission is due to occur, then a second point, the scission point, at which the nucleus is cut into two fragments with different masses.

Emission of photons is also possible. The nucleus emits the particles until its energy of the excitation is above the binding energy of the last nucleon. At this state, about 8 MeV are remaining. They will be emitted out of the nucleus as the gamma radiation.

The end of gamma emission does not mean that the deexcitation process is at the end. The resulting nucleus after gamma decay is often a radioisotope which will decay until the corresponding stable nucleus is reached.

1.1.2 Accelerator

Different beam performance levels are envisioned to satisfy the requirements of an XADS (experimental) facility and an ADS (industrial scale) plant. In the XADS facility, the blanket power needs to be high enough to be representative of a full scale ADS burner; a value between 80 MW_{th}¹ and 100 MW_{th} is considered adequate. Nominal parameters for the accelerator driving such an XADS facility are a beam power of 5 MW to 10 MW at an energy of 600 MeV or more, so that subcritical multiplier operation over a large range of k_{eff} can be evaluated [9, 10].

On the other hand, the nominal fission power for an industrial scale ADS plant would be about a factor of 10 greater than in XADS, between 500 MW_{th} to 1 500 MW_{th} per burner. The ultimate beam specifications for both an XADS facility and ADS industrial systems will be dependent on the range of k_{eff} desired for operation of the subcritical assemblies.

The optimum proton energy for production of neutrons by spallation in a heavy metal target, in terms of costs, target heating, and system efficiency, lies in the range from 600 to 1 000 MeV. Although specific neutron production efficiency (neutrons per unit of beam power) continues to increase up to about 1.5 GeV, a minimum cost, performance optimized facility is generally obtained at somewhat lower energies due to other factors, such as the beam current, the accelerating gradient, and the accelerator electrical efficiency. For XADS power levels, the optimum energy in terms of minimizing the accelerator cost would be about 400 MeV, but target considerations drive the practical lowest beam energy up to 600 MeV. The power deposition density in the spallation target is too high at lower beam energies, and the energy loss in the beam entrance window becomes significant. For the industrial ADS plant, the range 800 MeV to 1 000 MeV is optimum, with lower energies matched to lower beam powers and vice versa.

Two completely different kinds of machines can be considered for acceleration of high currents of protons: linear accelerators and cyclotrons. For an industrial scale ADS system, the logical accelerator choice would be a linear accelerator. The present status of cyclotron technology extrapolates to maximum beam powers and energies for a single cyclotron to about 10 MW at 1 GeV. Linear accelerator beam theory and recent technology advances have confirmed that a linear accelerator capable of delivering up to 100 MW at 1 GeV is a relatively direct extension of existing technology. Another factor favoring a linear accelerator is that the system reliability and fault minimization will lead to a design requirement that will require the accelerator operating point to be well below its maximum limits.

¹MW_{th} - thermal power

1.1.3 Subcritical reactor

A subcritical reactor is a nuclear fission reactor that produces fission without achieving criticality. Instead of a sustaining chain reaction, it uses additional neutrons from an outside source.

While originally thought that an ADS would be a part of a light water reactor design, other proposals have been made that incorporate an ADS into generation IV reactor concepts. One such proposal calls for a gas cooled fast reactor that is fueled primarily by plutonium and americium. Americium is difficult to use in any critical reactor due to its neutronic properties that tend to make the moderator temperature coefficient more positive, decreasing stability. The inherent safety of an ADS, however, would allow americium to be safely burned.

1.2 Experimental ADS

In the 90's, mainly optimistic views about ADS existed, and several ambitious projects of subcritical systems and accelerators were planned. But, in the 21st century the same technical, physical, and financial problems as 20 years ago exist. They make a considerable progress in this field impossible. The most important ADS activities are mentioned in next paragraphs.

1.2.1 European research

In European scale, the research is coordinated within special framework programmes [11]. "The Fifth Framework Programme - Euroatom" was a part of the FP5 programme, which was concerned also about the research in ADS, and within it the following activities concerning ADS research were performed:

- MEGAPIE (CERN), the project has recently fulfilled its goal and demonstrated the feasibility of safely running a liquid heavy-metal Pb-Bi target in the 1 MW proton beam [12].
- THORIUM CYCLE (Holland), CONFIRM (Sweden) projects were focused on the nuclear data for thorium-cycle reactors and for ADS construction materials.
- PDS-XADS (France) was a theoretical study focused on realization, safety, licensing and price of the construction of European XADS facility.

- ADOPT (Belgium) network was created to coordinate research activities of the whole Fifth framework programme.
- Experimental project HINDAS (Belgium) used several European accelerators in order to obtain experimental cross-section data needed for ADS experiments.
- nTOF (CERN) was another project focused on the cross-sections measurements for materials which are supposed to be used in ADS.
- MUSE experiments were performed in order to provide basic understanding of the behavior of subcritical systems driven with the outside neutron source.

The "Sixth Framework programme - Euroatom" which followed after the closing of the previous one was focused on the research of nuclear fission and radiational protection. Its main activities were:

- EUROPART (EUROpean Research Programme for the PARTitioning of Minor Actinides)
- EUROTRANS (EUROpean Research Programme for the TRANSmutation of High Level Nuclear Waste in an Accelerator Driven System)
- RED IMPACT (Impact of Partitioning, Transmutation and Waste Reduction Technologies on the Final Waste Disposal Project).
- EFNUDAT (European Facilities for Nuclear Data Measurements) The main objective of EFNUDAT is to promote the coherent use and integration of infrastructure related services via networking, transnational access to the participating facilities for nuclear data measurements and joint research activities.

Research centers CIEMAT (Centro de Investigaciones Energéticas, Medioambientales y Tecnológicas), project ESS (European Spallation Source) and research center ITEP in Moscow are also involved in the program of developing ADS and obtaining data needed for their functioning.

The experimental facilities directly connected to ADS which currently exist or are planned in Europe are the following:

- Project IREN - Intensive Resonance Neutron Source is being built in the JINR Dubna. It should be used as a neutron source for a large spectrum of applications, some of them concerning ADS.

- MYRRHA (Multi-purpose hYbrid Research Reactor for High-tech Applications) is an experimental ADS being built in Mole (Belgium). It is composed of the proton accelerator (350 MeV), liquid Pb-Bi target and a subcritical blanket in which are in a hexagonal lattice inserted 45 rods with MOX fuel (30% Pu), with $k_{eff} \bar{0}.95$.
- YALINA in Minsk is composed of a subcritical uranium-polyethylene target-blanket to which high intensive neutron generator NG-12-1 (14 MeV, intensity 10^{10} - 10^{12} n/s) provides neutrons. The system is used for the studies of subcritical systems with external source.
- TRASCO (TRAsmutazione SCOrie), prepared following C. Rubbia's suggestions, was focused on the studies of physics and technologies needed for ADS development. It consists of a linear proton accelerator (1 GeV) and Pb-Bi target, and was used for the research in ADS fields connected with accelerators, spallation and transport of neutrons.
- TARC (Transmutation by Adiabatic Resonance Crossing), which was running in years 1996-1999, demonstrated the efficiency of the "Adiabatic Resonance Crossing" method in the liquidation of Long Lived Fission Fragments in the ADS. It was sited at the CERN PS accelerator and precise measurements of distributions of spallation neutrons were performed in the lead cube with 3m side.
- TRADE (TRiga Accelerator Driven Experiment) came with an interesting idea - to couple existing, well studied, low-power reactor with the spallation target and accelerator. The core of the reactor is supposed to have k_{eff} in the range between 0.9-0.99 and a constant proton beam (few hundred μA) will be provided by accelerator to Pb target. The project was stopped in December 2004.

1.2.2 Research outside Europe

In the USA the program Advanced Accelerator Applications (AAA) was funded for the research of nuclear problems connected to energetics and waste, which is supposed to manage different projects connected to accelerator technologies as for example: Accelerator Production of Tritium (APT) and Accelerator Transmutation of Waste (ATW). The program has three main aims:

- The transformation of the APT project to the Accelerator Demonstration Facility (ADF).

- The construction of the ADF.
- Testing and study of technologies connected to transmutation systems.

The project Spallation Neutron Source (SNS) was funded in Oak Ridge, Tennessee, USA with the collaboration of six USA laboratories: Argonne, Lawrence Berkeley, Brookhaven, Jefferson, Los Alamos and Oak Ridge [1]. In May, 2006, it produced first neutrons after 7 years of construction. It is supposed to provide the world's most intensive neutron beams for scientific research and industrial use.

ADS research in Japan is integrated into the broad programme of fundamental and applied nuclear physics. From October, 1988, the research on partitioning and transmutation in Japan has been conducted in the frame of OMEGA programme². The research is focused on the development of high power accelerators: a superconducting high intensity proton accelerator with energy 1 - 1.5 GeV, and the current several tenths of mA is under development. The accelerator is expected to be supplemented by an experimental transmutation facility and taken into operation after the year 2008.

South Korea has a long term research project in progress at KAERI (Korean Atomic Energy Research Institute) since 1992. The aim is the development of a method for reducing the radiotoxicity of high level waste [14]. This programme comprises the evaluation of data, the study of the possibility of transmuting heavy actinides in pressure water reactors, the development of codes for the calculation of transmutation rates and the design of transmutation systems. Conventional reactors, fast reactors and hybrid systems consisting of a subcritical reactor and an accelerator are being studied. After 1997, the programme was reviewed and ADS research became one of KAERI's main areas of work.

1.2.3 Russian research

Since 1994, several Russian research institutes have been involved in the ADS research. The studies have comprised the realization of a linear proton accelerator to drive a specially designed subcritical transmutation core as well as reprocessing processes which can be applied in an integrated transmutation facility. The studies on the liquid lead-bismuth target and the subcritical core with two zones brought important results: the recommendation to use lighter material for the proton beam window (titanium and graphite), and the conclusion that problems with the accumulation of ²¹⁰Po in lead-bismuth

²OMEGA stands for "Options for Making Extra Gain of Actinides and fission products generated in the nuclear fuel cycle") [13]

targets are less important than previously believed. The focus of some other running projects is on cross-section measurements for reaction induced by neutrons and protons in energy ranges from GeV down to meV.

The Joint Institute for Nuclear Research in Dubna (JINR) has a long term tradition of cross-section measurement using the Phasotron accelerator [15, 16]. In the last two decades, experiments with relativistic protons and deuterons from the Phasotron, Synchrophasotron and Nuclotron accelerators (0.66-2.5 GeV) directed on thick, lead targets were started. These experiments, which are the continuation of Dubna long term activities in the ADS filed, are described below in more detail.

Cross-section measurements

The measurements of the cross-section of 660 MeV protons with different fission products (^{129}I), natural uranium and higher actinides (^{237}Np , ^{241}Am , ^{239}Pu) were realized with specially prepared samples irradiated by the protons extracted from the Phasotron accelerator. After the irradiation, the quantity of the produced isotopes was determined by the means of the gamma spectrometry. The results contributed data to EXFOR cross-section database and are also used to check the theoretical models for cross-section predictions [15, 16].

Gamma-2

Gamma-2 was the experiment focused to the studies of the neutron production in the spallation process, and their moderation and transport in the neutron moderator. Gamma-2 consisted of a thick, lead target (diameter 8 cm, length 20 cm) surrounded by a paraffin moderator of 6 cm thickness to slow down fast spallation neutrons to resonance energies. The target was irradiated with relativistic protons from the Synchrotron accelerator. Slow neutrons were detected through (n,γ) reaction by activation detectors placed on top of the polyethylene along the whole setup. Gamma-2 was a simple setup providing very useful results for the comparison with the computer codes predictions [17, 18].

Phasotron experiment

While Gamma-2 was focused on the overall neutron production, the Phasotron experiment was mostly concerned about the spatial distribution of high energy neutrons ($E > 10$ MeV), and the transmutation of radioactive iodine ^{129}I in such neutron spectrum. The intensive beam of 660 MeV protons from the Phasotron accelerator was directed to a bare, lead target ($2r=9.6\text{cm}$,

$l=45.2\text{cm}$). Small activation detectors (metal foils $2\times 2\times 0.1\text{ cm}^3$) were placed on top of the target together with the iodine transmutation samples. The results from this geometrically simple setup were also useful for computer codes tests.

Energy Plus Transmutation

The "Energy plus transmutation" (EPT) setup consists of a thick, lead target ($2r=8.4\text{ cm}$, $l=48\text{cm}$) surrounded with an uranium blanket (206.4 kg) and placed in a polyethylene box. In series of experiments, relativistic protons and deuterons (from Synchrophasotron and Nuclotron accelerators) of energies from 0.7 to 2.52 GeV were directed to the target. Produced neutron flux and its transmutation capabilities were studied with activation, solid state nuclear track, ^3He and other detectors. Separate parts of the complex EPT setup have each their influence on the produced neutron field, and the setup is not appropriate for direct tests of model predictions. However, the possible sources of systematic uncertainties of obtained experimental data were studied, and the experimental data can be used for comparison with the results of the complex computer codes such as MCNPX and FLUKA [19, 20, 21].

Subcritical Assembly at Dubna

The Subcritical Assembly at Dubna (SAD) is a planned project that should consist of a replaceable spallation target (Pb, W) with a subcritical MOX blanket (UO_2+PuO_2). The studies of neutron production, power release, fission rates of higher actinides and transmutation rates of fission products are some of the motivations for this complicated setup [22].

1.3 Simulations

The development of an ADS program requires accurate simulation tools. The tools developed for nuclear reactors cannot be applied immediately to the externally driven subcritical systems. The spatial and energetic distributions of the neutron flux are expected to be radically different than in a nuclear reactor. While in a critical reactor the flux distribution inside the volume is determined essentially by the boundary conditions, in an ADS the effect of the initial high energy cascade is dominant. In a subcritical arrangement, the neutron flux along any radial direction starting from the center must decrease in an approximately exponential manner. Neutrons in classical reactors have energies up to 20 MeV, while in an ADS the neutron produced in spallation have energies up to the primary beam energy. The behavior of the neutrons

above 20 MeV is theoretically known, but has not yet been tested on a large scale devices as ADS.

One of the main goals of the projects mentioned in the previous section was the validation of the computer codes. Detailed comparisons of measured and simulated values were performed, and from most points of view, good agreement with simulation was obtained. This confirms in particular that the spallation process is correctly predicted and validates the reliability of the predictions of the integral neutronic parameters of experimental ADS facilities. The energetic and spatial distributions of produced neutrons are not predicted so reliably and differences between the experimental and simulated values can be up to two times. These differences apply to a small part of produced neutrons (less than 10%), and therefore do not influence the integral quantities, however, they show that the knowledge of all processes is not complete. There are also significant differences between the different simulation codes. Continuously, new validation tests are performed and simulation tools are developed.

Computer programs used for neutron multiplying systems fall into two broad categories: (a) deterministic and (b) Monte Carlo codes.

- **Deterministic codes** are based on the solution of the neutron transport equations. To make the problem amenable to a computer solution, a discretisation is introduced both in space and in energy. These codes operate on a spatial grid and on a fixed number of energy "groups". While this approach has shown its viability in many applications, and is widely used to simulate critical reactors, it suffers from some drawbacks that become important in the case of a subcritical device coupled to a particle accelerator, but the main problem is that the required complete analytical model would not provide a solution in a time shorter than with a well implemented Monte Carlo.

In summary, deterministic codes are well adapted to the simulation of relatively well known critical systems, but they cannot be easily used in their present form to explore the new domain of subcritical accelerator driven systems. They are usually useful after tuning as they tend to represent a parametrization of the system rather than a true simulation.

- **Monte Carlo codes.** The second major type of approach to the simulation of nuclear fission systems is the Monte Carlo method. When point-wise cross-sections are used, the Monte Carlo is free from almost all the drawbacks of deterministic codes, but its precision varies inversely with the square root of the number of events processed. This represents a potentially large problem of CPU time, particularly when

the simulation must span the entire lifetime of a power producing system.

Fully analogous Monte Carlo simulations with point-wise cross-sections however provide a host of information not easily available to deterministic codes: "infinite" spatial resolution; full treatment of resonances (correct account of selfshielding effects) and "on line" full 3D calculation of activation and spectrum dependent transmutation effects.

The main limitations of the Monte Carlo method are:

- The correctness of the neutron cross-sections, but this is common to all transport codes.
- The physical model used, but for low energy neutron transport this is mainly expressed by the partial reaction cross-sections, double differential cross-sections, etc.
- Its intrinsic imprecision, due to the random nature of the generated events. This imprecision may be reduced by increasing the number of trial events, now possible with the help of fast parallel computers which can generate many events simultaneously.

A number of Monte Carlo and deterministic codes are available for the purpose of ADS simulations and some details on their functioning are given below.

1.3.1 Spallation reaction

Most existing codes used for high energy ion-nucleus reactions are based on the intranuclear cascade (INC) model for the first stage of the reaction, the final steps being described by an evaporation (EVAP) model [23]. The philosophies of the INC and EVAP models are very different: The INC calculations follow the history of individual nucleons in a classical or semi-classical manner, while the EVAP calculations follow the deexcitation of the whole nucleus while it decays from one nuclear level to a lower one. The connection between the two approaches is the delicate point of the simulations of ion-nucleus reactions. In principle the single particle approach of INC should be justified as long as the wavelength of the incident nucleon is smaller than the nucleon radius ($\lambda \leq r_{nucleus}$ or $E > 160$ MeV). On the other hand, the evaporation approach is valid as long as the energy of the nucleon does not exceed too much the nuclear potential depth (≈ 40 MeV [24, 25]). Thus, the transition energy between the INC and EVAP calculations cannot be specified rigorously. For that matter several codes have added an intermediate

step whose domain of validity is expected to overlap on the INC and EVAP domains. This step is the preequilibrium phase.

- During the **Intranuclear cascade (INC)** - $E \geq \approx 160$ MeV - the incident particle collides with one or several nucleons of the target nucleus. The struck nucleons collide with the unperturbed nucleons and the cascade develops. The INC calculation for a specific nucleon stops whenever its energy falls below a specified value, related to the depth of the nuclear potential well (≈ 40 MeV).
- **Preequilibrium phase:** The INC model lacks justification for nucleon energies (inside the nucleus) below around 160 MeV. Preequilibrium models have, since long, been used in nuclear physics in this energy domain. These models follow a population of quasi particle excitations of the nuclear Fermi gas by means of a master equation. Quasi particle states are characterized by their particle escape and damping widths. Angular distributions are associated to the escaping particles. In a sense, preequilibrium models allow an easier phenomenological adjustment of angular distributions than does the intranuclear cascade. There are many versions of preequilibrium models, but, unhappily, no clear criteria to choose among them, except their ability to reproduce experimental data.
- **Evaporation phase** - $E \leq \approx 40$ MeV: The compound nucleus is formed and the energy is uniformly distributed throughout it. The nucleus is in a highly excited state and losses its energy by evaporating neutrons, by fission or γ emission. The most important ingredients of the calculations of this phase are the level densities. It is important to account for the influence of shell effects on the level density parameters and of their washing out with nuclear temperature.

Modelling of intranuclear cascade

The INC model, first proposed by Serber [26], is used to describe the interaction between high energy hadrons (pions, protons, anti-protons...) or light nuclei with a target nucleus. The nucleus is considered under a statistical point of view. When the nucleus is at rest, it is regarded as a degenerated Fermi gas at zero temperature. All the particles which are scattered or produced during the cascade are treated in the field of the classical mechanics, they are defined by their velocity and their position. Every scattering which would lead to an already occupied energy level is forbidden because the nu-

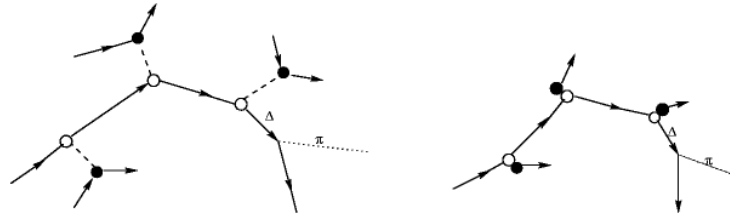


Figure 1.3: The two approaches of the INC model: left Cugnon approach, right Bertini approach. These two models describe how an incoming nucleon interacts with the nucleons inside of the target nucleus. The incoming nucleon is represented by a white circle, the nucleons of the target nucleus are represented by black circles. Note that pions and delta particles may be produced during the cascade (noted p and D) [30].

cleons are fermions. As a matter of fact, only one fermion can be in a given state according to the Pauli exclusion principle.

There are two main approaches to describe the intranuclear cascades (see fig. 1.3). In the Bertini approach [4, 27], the incoming particle hits the target material (target nuclei) which is regarded as a continuous medium. The particles have a specific mean free path $\lambda = (\rho\sigma)^{-1}$ in this medium (i.e. inside a target nucleus). After each path, the particle scatters on a nucleon with which it exchanges energy. In the Cugnon approach [28, 29], the incoming particle is propagating freely in the target material (i.e. inside a target nucleus) until it is at its minimum distance of approach from a nucleon d_{min} . The particle is scattered if $d_{min} \leq \sqrt{\frac{\sigma_{tot}}{\pi}}$.

Modelling of deexcitation

In the deexcitation phase three processes compete: evaporation, fission, γ -emission. The last one is of negligible influence, evaporation and fission are in most cases equally probable.

There are several models of neutron evaporation which are all based on calculations of highly excited states of nucleus and deexcitations to ground state. Most often used are DRESNER [31] and ABLA [32], which is more sophisticated as it takes into account several corrections left out by Dresner model (nuclear collective states,, etc.).

Two models of fission are available for describing high-energy fission, the ORNL model (from Oak Ridge National Laboratory) [33] and the RAL model (from Rutherfords Appleton Laboratory) [34]. The ORNL model simulates only fission for actinides with $Z > 90$, while the RAL model allows fission from $Z > 71$. The ABLA fission-evaporation model uses its own fission model.

The γ -emission is not very important when other deexcitation channels are open.

1.3.2 High energy cross-section libraries

While the spallation models are believed to be quite reliable above ≈ 150 MeV and, on the other hand, the behavior of neutrons with energies < 20 MeV in reactor systems is also well studied, there exist an energy gap from 20 up to 150 MeV, where we do not know how to model successfully the reactions of neutrons in different materials.

Suites of evaluated reaction cross-section files (LA150 library [35], NRG-2003 library [36]) have been developed in support of ADS design. They cover the energies from 20 MeV up to 150 MeV (200 MeV for NRG) for neutrons and from 1 up to 150 MeV (200 MeV for NRG) for protons. Evaluations are completed for isotopes of the structural, shielding, and target-blanket materials.

The primary motivation for using these evaluated data is the accuracy improvements that one can expect to obtain in the below 200 MeV energy region. In most previous transport simulations, intranuclear cascade methods have been used for neutrons above 20 MeV and for protons at all energies, even though the semiclassical assumptions do not hold at lower energies. By developing evaluated cross-section libraries, one can expect to have the most accurate possible representation of the nuclear cross-sections.

The nuclear models used for LA150 cross-sections are based on the theoretical approaches that are appropriate for the energies in the few-MeV to 150 MeV range: the Hauser-Feshbach compound nucleus theory; preequilibrium calculations based on the Feshbach-Kerman-Koonin theory or the exciton model; direct reactions calculated from the optical model using collective excitation form factors; and elastic scattering from the optical model. The GNASH code was demonstrated to be one of the most accurate codes available for model calculations below 150 MeV in a Nuclear Energy Agency code intercomparison [37]. The optical model is used for predictions of the total, reaction, and elastic scattering cross-sections, different forms of the real and imaginary parts of optical nuclear potential are used. It is particularly useful for accurate representing the angular distributions in elastic scattering, allowing more accurate neutron transport simulations.

1.3.3 MCNPX

The MCNPX code [38] is a coupling of two previous calculations codes: LAHET [39] and MCNP [40]. MCNPX only needs one input file for both codes

and avoids the transfer of large data files. It allows the treatment of transport problems in a large range of energies, from thermal energy (25 meV) to a few GeV.

For neutron and proton energies lower than 20 MeV, quite complete sets of cross-sections are available for the major part of the stable nuclei. International cross-sections libraries such as ENDF [41], JEFF [42], JENDL [43], are available and are regularly updated. To treat the transport, MCNP uses data deduced of these libraries after processing them with NJOY/ACER [44].

For energies larger than 20 MeV, there are less cross-section data. Presently the LA150 and NRG-2003 libraries, which cover around 50 isotope (most common in ADS) up to 150-200 MeV, are included with the MCNPX code package and the preparation of complete data files up to 150 MeV is in progress in several projects.

The main features of MCNPX are:

- the BERTINI [4, 27] and the ISABEL [45, 46] INC models imported from LAHET, and a third INC model: the CEM03 model [47, 48],
- the INCL4 [49] model based on Cugnon INC approach (see 1.3.1),
- a multistage preequilibrium model [50],
- DRESNER [31] and ABLA [32] evaporation models,
- RAL [34] and ORNL [33] fission models,
- a nucleon elastic scattering model,
- a gamma production model,
- the electromagnetic part of MCNPX is imported from MCNP.

MCNPX code package is the main simulation tool used in this work. Several beta version of MCNPX 2.6 that were released during the realization of this work were used in simulations, but the features that would affect the results were not changing.

1.3.4 FLUKA

FLUKA [51, 52] is a general purpose tool for calculations of particle transport and interactions with matter, covering an extended range of applications spanning from proton and electron accelerator shielding to target design, calorimetry, activation, dosimetry, detector design, ADS, cosmic rays, neutrino physics, radiotherapy etc.

FLUKA can simulate with high accuracy the interaction and propagation in matter of about 60 different particles, including photons and electrons from 1 keV to thousands of TeV, neutrinos, muons of any energy, hadrons of energies up to 20 TeV (up to 10 PeV by linking FLUKA with the DPMJET code) and all the corresponding antiparticles, neutrons down to thermal energies and heavy ions.

The PEANUT (PreEquilibrium Approach to Nuclear Thermalization) [53] is used for the simulation of hadron-nuclear interactions from GeV region down to 20 MeV, through more steps (Generalized intranuclear cascade, Preequilibrium stage, FLUKA evaporation model). The cross-section libraries used in FLUKA are imported from ENDF/B-VI [41]. The FLUKA2008 version was used in this work.

1.3.5 TALYS

TALYS [54] is a software package for the simulation of nuclear reactions that is used to calculate total and partial cross-sections, for the detector materials used in our experiments. TALYS is a deterministic code, it implements various physical models and can quite reliably reproduce various cross-sections in the energy range 1keV-250 MeV.

In this work, partial cross-sections for reaction channels (n,xn) , (n,α) , (n,fis) for detector materials (Au, Al, Bi, I...) are calculated with TALYS 1.0 from 1-150 MeV. From 150 MeV, the cross-sections calculated with MCNPX code package and CEM03 nuclear model normalized to TALYS values at 150 MeV were used.

1.4 Motivation for Dubna ADS experiments and this work

The existing studies on the neutron production on lead targets [55, 56] are focused either on the overall neutron production in thick targets or on the angular distribution of spallation neutrons in thin targets. The current Dubna ADS program combines both - thick targets in which the spatial distribution of neutrons is studied. This is the intermediate level between the pure spallation studies and the studies of spallation together with the transport and moderation of neutrons. These experiments present a step towards the real ADS devices, and enable the studies of materials, detectors, and simulation models under ADS working conditions.

Two experimental setups are presented below in more detail: a bare, lead target which was irradiated with 660 MeV protons from the Phasotron

accelerator in November, 2003; and a complex setup Energy Plus Transmutation, which was from the year 2003 several times irradiated with protons (0.7-2 GeV) and deuterons (1.6 and 2.52 GeV) from Synchrotron and Nuclotron accelerators. Around 10^{13} incident particles were directed to the targets during few hours. The neutron fluxes in different places of the setups were probed with many types of detectors: solid state nuclear track detectors, nuclear emulsions, ^3He detector, and the activation detectors which are discussed in this work. Thin foils ($2 \times 2 \times 0.1 \text{ cm}^3$) of monoisotopic materials (Al, Au, Bi, In, Ta, etc.) with masses around 1 g were activated during the irradiation and measured with the HPGe detectors after the experiment (explained in Chapter 2. The experimental results carry information about the total number and about the spatial and energetic distribution of produced neutrons.

By the time of the beginning of this PhD, the detailed Monte Carlo simulation studies of these two setups did not exist. I have personally implemented the setups into the MCNPX code, simulated the experimental values and performed other simulations to estimate the uncertainties of the experimental data. For this purpose I used a method of modifying the simulation parameters within the accuracy of the measured experimental parameters. The systematical uncertainties of experimental results can be approximated with the difference in the simulated values with such modified setups. I also compared the simulations with different spallation models (the setups were also implemented in the FLUKA code) compared to experimental values.

In the first part of the work I studied the accuracy of the neutron activation analysis method with the help of Monte Carlo simulations.

In the next part, I analyzed the experimental results from the Phasotron experiment (I did not participate at its planning and realization) and provided Monte Carlo simulations to the experiment.

In the last part, I analyzed the Energy Plus Transmutation setup with the help of the MCNPX code and performed the detailed studies of the systematical uncertainties. My main task in the collaboration is to provide simulations, however, I was personally present at the planning and realization of the experiments with 0.7 GeV protons and with 1.6 and 2.52 GeV deuterons. The analysis of these experiments was performed by Ondřej Svoboda. I compared the experimental values from these and other experiments (protons at 1 GeV is given as an example in this work) with simulations.

Chapter 2

Neutron activation analysis

Neutron activation detectors are one of the best options for the measurements of the produced neutron field characteristics in the spallation experiments. Their main advantage is their small size and they are very useful in the measurements of the spatial distribution of the neutron field. At the Dubna experiments, the neutron activation detectors were mainly used in the form of thin foils and shall be from now on referred to as activation foils to avoid confusion with semiconductor detectors.

The detection of neutrons with activation foils occurs in two steps:

- the neutrons interact with the foil material,
- the activity of radionuclides produced by neutrons in the foil during the irradiation is analyzed.

In the first step, foils are irradiated and part of their material is activated through e.g. (n,xn) , (n,α) , and (n,γ) interactions. The new isotopes are usually unstable, decaying (β^+ , β^- , EC) and emitting characteristic gamma photons. These photons are registered with semiconductor detectors (usually HPGe) in the second step. The amounts of produced isotopes are calculated from the measured activities. The information about the neutron field can also be obtained, providing that the mechanisms of the isotope production are well known.

Gamma spectroscopy is part of many research methods and applications and is covered in several textbooks (for e.g. [57]). However, there exist some specific problems connected to the use of activation foils in spallation experiments, which I am studying in this chapter. For complete understanding, I am showing the derivation of basic spectroscopy equations from the scratch at the beginning. In the rest of this chapter, I am exploiting Monte Carlo simulations to study the processes around the production and detection of

radioisotopes and the accuracy of the neutron activation analysis method in spallation experiments.

2.1 The production and detection of radioisotopes

Nuclear reactions where neutrons are produced (spallation, direct reactions) usually do not produce monoenergetic neutrons, but time and space dependent neutron flux with the energy distribution $\Phi(E)$.

The space distribution of the neutron flux can be measured with small foils placed at different places. The time structure of single neutron production reaction is usually not measured with this technique, the irradiation should be stable in time (the irradiation is connected with the accelerator output, the correction for unstable accelerator output is discussed in last paragraphs).

To probe the energetic distribution of neutrons, one has to choose a foil material in which different radioisotopes (each at different neutron energy) are produced.

If an activation material is placed in the neutron flux, a specific radioisotope is produced with the rate P , and is at the same time decaying with the decay constant $\lambda = \frac{\ln(2)}{\tau_{1/2}}$. The rate P is proportional to the number of available nuclei for the reaction (N_0) and the neutron flux $\Phi(E)$ folded with reaction cross-section $\sigma(E)$:

$$P = N_0 \int \Phi(E)\sigma(E)dE. \quad (2.1)$$

The amount of produced radioisotope is described with the equation:

$$\frac{dN}{dt} = P - \lambda N. \quad (2.2)$$

The number of produced radioisotopes is zero at the beginning of the irradiation, $N(0) = 0$, and the solution to the equation is:

$$N(t) = \frac{P}{\lambda}(1 - e^{-\lambda t}). \quad (2.3)$$

At the end of the irradiation, there is $N(t_{irr})$ produced radioisotopes:

$$N(t_{irr}) = \frac{P}{\lambda}(1 - e^{-\lambda t_{irr}}). \quad (2.4)$$

After the irradiation, the measurements with the HPGe detectors start. The activated material is measured during the time interval $(t_0, t_0 + t_{real})$, where t_0 is the time from the end of the irradiation. The number of radioisotopes that decay during this time interval is:

$$\begin{aligned} s &= N(t_0) - N(t_0 + t_{real}) = N(t_{irr})(e^{-\lambda t_0} - e^{-\lambda(t_0+t_{real})}) = \\ &= \frac{P}{\lambda}(1 - e^{-\lambda t_{irr}})e^{-\lambda t_0}(1 - e^{-\lambda t_{real}}). \end{aligned} \quad (2.5)$$

Photons from part of the decayed radioisotopes are detected by the HPGe detector as a gamma peak with the surface S , which is:

$$S = s \cdot \epsilon_P(E) \cdot I_\gamma(E) \cdot \text{COI} \cdot C_g \cdot C_s \cdot C_t \cdot \frac{t_{live}}{t_{real}}, \quad (2.6)$$

where $\epsilon_P(E)$ is the peak efficiency of the HPGe for gamma photons of energy E , $I_\gamma(E)$ is the gamma emission probability (probability that the photon of energy E emitted in the decay), $\frac{t_{live}}{t_{real}}$ is the correction for the dead time of the HPGe detector, COI is the correction for the decay cascade effect, C_g is the geometrical correction, C_s is the correction because of self-absorption of gamma photons in activation foil material, and C_t is the correction for the beam instabilities during the irradiation. The rate P is expressed from equations (2.5) and (2.6) as:

$$P = \frac{S \cdot \lambda}{\epsilon_P(E) \cdot I_\gamma(E) \cdot \text{COI} \cdot C_g \cdot C_s \cdot C_t} \frac{t_{real}}{t_{live}} \frac{e^{\lambda t_0}}{(1 - e^{-\lambda t_{irr}})(1 - e^{-\lambda t_{real}})} \quad (2.7)$$

The number of the produced radioisotope A per one gram of the material and per beam particle is called the production rate $B(A)$ and is commonly used in the spallation physics. The production rate $B(A)$ can be connected directly with the rate P (the connection between the neutron flux per time and the neutron flux per beam particle is $\Phi'(E) = \Phi(E) \frac{t_{irr}}{N_p}$):

$$B(A) = \frac{1}{m} \int_E \Phi'(E) \sigma(E) dE = \frac{1}{m} \int_E \Phi(E) \frac{t_{irr}}{N_p} \sigma(E) dE = \frac{t_{irr}}{m N_p} P, \quad (2.8)$$

where t_{irr} is the irradiation time, m is the mass of the activation foil, and N_p is the total number of protons.

So far, the irradiation was assumed to be continuous and constant in time. Some accelerators monitor the time structure of their output in regular intervals, and in cases when the output is not constant in time, the time dependency of $P(t)$ needs to be included in (2.2):

$$\frac{dN}{dt} = P(t) - \lambda N. \quad (2.9)$$

The solution is:

$$N(t) = e^{-\lambda t} \int_0^t e^{\lambda t'} P(t') dt'. \quad (2.10)$$

The time structure of the irradiation can be approximated with n bunches of the beam intensity r_i , constant in the time intervals $[t_i, t_{i+1}]$. With this approximation, the integral in equation 2.10 is simplified to:

$$N(t_n) = \frac{e^{-\lambda t_n}}{\lambda} \sum_{i=1}^n P_i (e^{\lambda t_i} - e^{\lambda t_{i-1}}) \quad (2.11)$$

The ratio between the number of produced radioisotopes for stable (2.3) and not stable irradiation (2.10) is the correction for the beam instability C_t :

$$C_t = \frac{\frac{P}{\lambda} (1 - e^{-\lambda t_{irr}})}{\frac{e^{-\lambda t_n}}{\lambda} \sum_{i=1}^n P_i (e^{\lambda t_i} - e^{\lambda t_{i-1}})} \quad (2.12)$$

By realizing that P is proportional to the number of protons in a time interval ($P = C \frac{N_p}{t_{irr}}$, $P_i = C \frac{N_i}{t_i - t_{i-1}}$ and $t_{irr} = t_n$) and by introducing $W_i = \frac{N_i}{N}$ (number of protons in the bunch i divided by the total number of protons), factor C_t can be expressed as:

$$C_t = \frac{1 - e^{-\lambda t_n}}{t_n \sum_{i=1}^n \frac{W_i}{(t_i - t_{i-1})} e^{-\lambda(t_n - t_i)} (1 - e^{-\lambda(t_i - t_{i-1})})}. \quad (2.13)$$

2.2 Detection of radioisotopes

Emitted gamma photons are detected with HPGe detectors. Photons interact with the detector active material (ca. 120 cm²) mainly by photoeffect, Compton scattering and pair production, and can deposit in the detector material their full energy or just a part of it. The response of the detector consists of the peaks at the energies of the emitted photons and the continuum below this energy (Compton edge, escape peaks), see Figure 2.8.

The probability that the photon deposits its entire energy in the detector is called full peak efficiency - $\epsilon_P(E)$, the probability that it deposits any non zero part of its energy (up to its entire energy) is called total efficiency $\epsilon_T(E)$. In the equation 2.7 acts only peak efficiency $\epsilon_P(E)$, total efficiency $\epsilon_T(E)$ is

however hidden in the COI correction (see Section 2.2.6), which can range up to ten percents.

The response of HPGe detectors can be reliably predicted with the Monte Carlo codes. The details of the detector inner structure are often company secrets and mainly for this reason the simulated predictions have limited accuracy. In the Figure 2.1 is shown the detector geometry as it was implemented in the MCNPX code package for the simulations of $\epsilon_P(E)$ and $\epsilon_T(E)$ efficiencies. The energy deposited in the detector (F8 tally) at incident photons energies in the keV-MeV range was studied. The efficiencies were defined as the ratio between the number of simulated histories at which full/partial energy was deposited in the detector and the number of all histories.

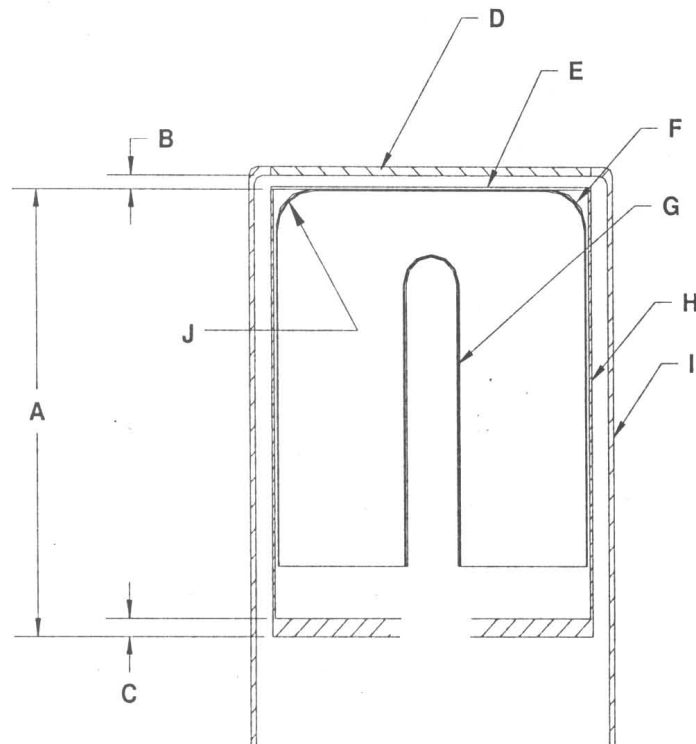


Figure 2.1: Extract of the ORTEC GMR-20190-R detector schematics (side cross-section). The crystal diameter is 56.8 mm (E), the length 51.3 mm (H), beryllium window is 0.5 mm thick (D) and the distance from the window to the detector is 3 mm (B). Other dimensions are company private.

2.2.1 Experimental calibration

The detectors are experimentally calibrated with radioactive isotope standards. The calibration samples are in the form of small dots of the radioactive isotope, doped on the glass, isotropically radiating photons in all directions. Both the full peak efficiency and the total efficiency are determined at the calibration. The $\epsilon_T(E)$ can be determined only with the calibration radioisotopes that have one single line in the decay scheme.

The calibration samples with the activity A_0 measured at time $t=0$ will undergo s decays during the calibration time interval $[t_0, t_0 + t_{real}]$:

$$s = N(t_0) - N(t_0 + t_{real}) = \frac{A_0}{\lambda} e^{-\lambda t_0} (1 - e^{-\lambda t_{real}}). \quad (2.14)$$

The measured peak and the detector efficiency $\epsilon_P(E)$ are connected with the relation (2.6), and we can write:

$$\epsilon_P(E) = \frac{S \cdot \lambda \cdot e^{\lambda t_0}}{A_0 \cdot I_\gamma \cdot COI \cdot C_g} \cdot \frac{t_{real}}{t_{live}} \cdot \frac{1}{1 - e^{-\lambda t_{real}}}. \quad (2.15)$$

The measurement times ($t_{real} \approx$ hours) are much smaller than the lifetimes of standard isotopes ($\tau \approx$ years), therefore, $e^{-\lambda t_{real}} \ll 1$. The last two factors from the previous equation can be simplified by writing $e^{-\lambda t_{real}}$ as Taylor series and keeping only the first terms:

$$\frac{t_{real}}{t_{live}} \cdot \frac{1}{1 - e^{-\lambda t_{real}}} = \frac{1 - (1 - \lambda t_{real})}{1 - (1 - \lambda t_{live})} \cdot \frac{1}{1 - (1 - \lambda t_{real} - \dots)} = \frac{1}{1 - e^{-\lambda t_{live}}}. \quad (2.16)$$

Because calibration samples are a good approximation of point source ($C_g = 1$), $\epsilon_P(E)$ can be written as:

$$\epsilon_P(E) = \frac{S \cdot \lambda \cdot e^{\lambda t_0}}{A_0 \cdot I_\gamma \cdot COI} \cdot \frac{1}{1 - e^{-\lambda t_{live}}}. \quad (2.17)$$

Total efficiency $\epsilon_T(E)$ is calculated in the same manner, however all counts in the detector up to the peak energy are taken for S instead of the counts in the peak.

2.2.2 Full peak efficiency - $\epsilon_P(E)$

The peak efficiencies were simulated at approximate distances where the samples are measured during the experiments, see Figure 2.2. The simulated peak efficiencies for the 4.1 cm position are shown in the Figure 2.3, together with



Figure 2.2: The holder for foil samples with the detector. The samples are measured at ca. 1.2, 2.4, 4.1, 6.5, 9.9, 14.7, 21.6, 31.1 cm from the detector.

the experimentally determined efficiencies (measured with standard calibration radioisotopes). Above 100 keV, the peak efficiencies are reliably fitted with higher order exponential function of the form:

$$\epsilon_P = e^{a+b \ln(E)+c \ln^2(E)+d \ln^3(E)+\dots} \quad (2.18)$$

There are few percent discrepancies between the fitted curve and the measured values. This differences have three different origins: inaccurate placement of the samples (ca. 1 mm inaccuracy), the inaccuracy in the measured activity of the calibration samples (about 2%) and absolute intensity of the gamma line (1%), and the error of the gamma peak fit (1-3%).

The maximum difference between the simulated and fitted experimental curve is below 10% up to the energy 2000 keV. This means that the detector is well modelled and that the following simulated results are reliable.

At the measurements of the activation foils with small intensity the close placement of the foil to the detector cannot be avoided. The inaccuracy of the placement has the biggest impact in these positions. The simulations with the samples placed at 4.0 cm and 4.2 cm from the detector predict for ca. 3% different results according to the simulation at 4.1 cm. In the position 2.4 cm, the displacement of the source for 1 mm changes the peak area for 4%, and further positions are less sensitive (6.5 cm \approx 2%, further $<$ 1%).

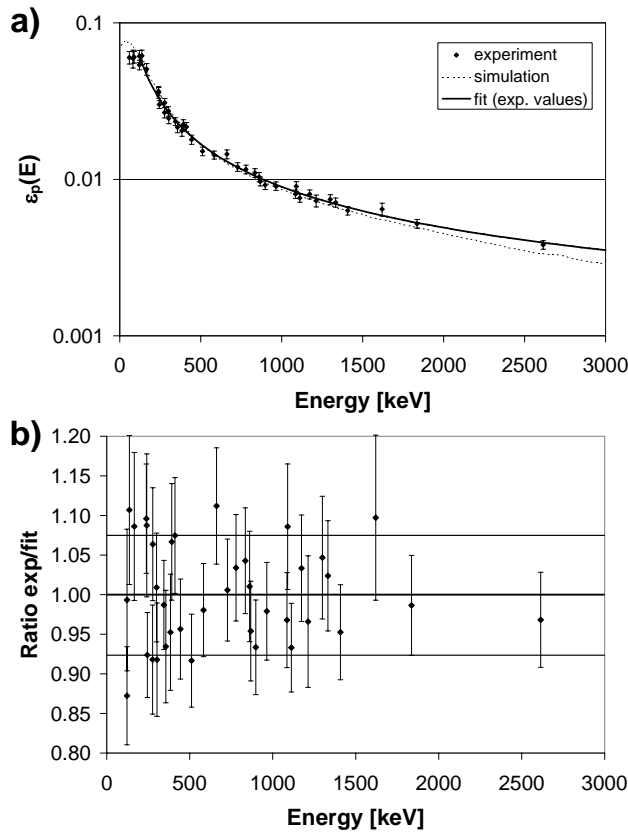


Figure 2.3: a) Simulated full peak efficiency ($\epsilon_P(E)$) curve for the ORTEC HPGe detector with experimentally determined efficiencies (the distance from the detector was 4.1 cm) and fitted curve (3rd order). b) Ratios between experimental data and the value calculated with the fitted curve. Uncertainties include the inaccuracy of the placement, of the measured activity and peak fit.

2.2.3 Total efficiency - $\epsilon_T(E)$

The Figure 2.4) shows the simulated $\epsilon_T(E)$, experimentally determined values and the experimental fit for the position 4.1 cm from the detector. The data are again fitted with higher order exponential function, usually less factors are needed than for $\epsilon_P(E)$.

The isotopes with only one gamma line in the spectrum (or two gamma lines provided that they are close together, eg. ^{57}Co) can be used for the experimental determination of ϵ_T . Only few calibration samples meet these requirements. The efficiency $\epsilon_T(E)$ is calculated from the equation 2.17, taking for S the sum of the signal in all channels up to and including the

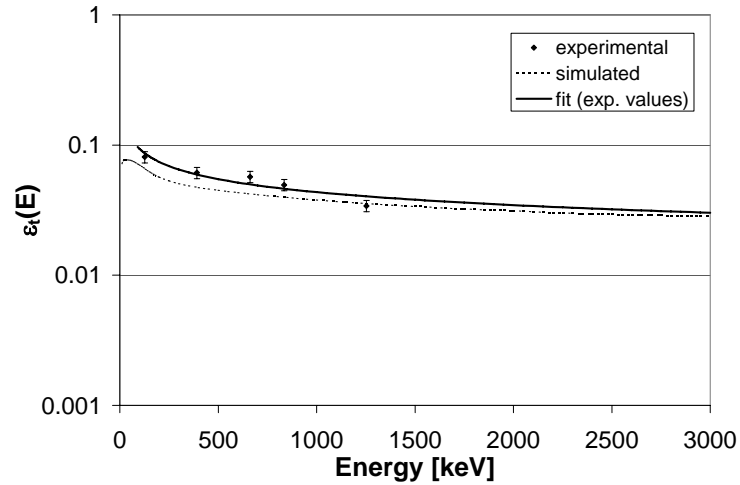


Figure 2.4: Simulated total efficiency ($\epsilon_T(E)$) with experimentally determined efficiencies and the fit of experimental values (1st order). The distance from the detector was 4.1 cm.

channels where the peak is registered. In case of longer calibration measurements (for low intensity calibration sources or positions far from the detector) the contribution from the background needs to be subtracted from this value.

The uncertainty of the fitted $\epsilon_T(E)$ curve is around 15%, because of fewer fitting points and the procedure with the background subtraction. Total efficiency is present in (2.7) through the cascade coefficient factor (see Section 2.2.6), which is usually below 5% (10% in rare cases). The $\epsilon_T(E)$ inaccuracy therefore contributes through the cascade coefficient factor $15\% \cdot 10\% \approx 1\%$ inaccuracy in the overall $B(A)$ calculation. The difference between the simulated and fitted experimental curve are 30% around 100 keV and decrease to 10% around the energy 3000 keV.

2.2.4 Geometrical correction factor - C_g

The calibration samples are pointlike dots of radioactive material packed in the sample holder. On the other hand, the activation foils are in the form of the foils with dimensions $2 \times 2 \text{ cm}^2$ and from 50-1000 μm thick (see Section 2.3.3), with the radioactivity distributed in the foil volume. As the photons from the edges of the foil have smaller solid angle covered by the detector, the detector response to the activation foil will be smaller than to the calibration sample with the same activity. The geometrical correction

2. NEUTRON ACTIVATION ANALYSIS

factor, which accounts for that difference, is:

$$C_g = \frac{\epsilon_P(\text{foil})}{\epsilon_P(\text{point})}, \quad (2.19)$$

where $\epsilon_P(\text{foil})$ is the efficiency for the activation foil and $\epsilon_P(\text{point})$ is the efficiency for the pointlike source with the same activity.

MCNPX simulations with sources in form of Al, Au and Bi foils (Al - $2 \times 2 \times 0.05 \text{ cm}^3$, Au - $2 \times 2 \times 0.005 \text{ cm}^3$, Bi - $2.5 \times 2.5 \times 0.1 \text{ cm}^3$) and with pointlike sources were compared to estimate the geometrical correction factor. In the simulation both types of radioactive sources were placed at the detector positions on 1.2, 2.4, 4.1, 6.5, 9.9, 14.7, 21.6, 31.1 cm (see Fig 2.2), and the simulated efficiencies ϵ_P were compared. In the Figure 2.5 is seen that the geometrical correction factor for larger distances from the detector is 1. At closer distances it can be as low as 0.92 for the largest Bi activation foils.

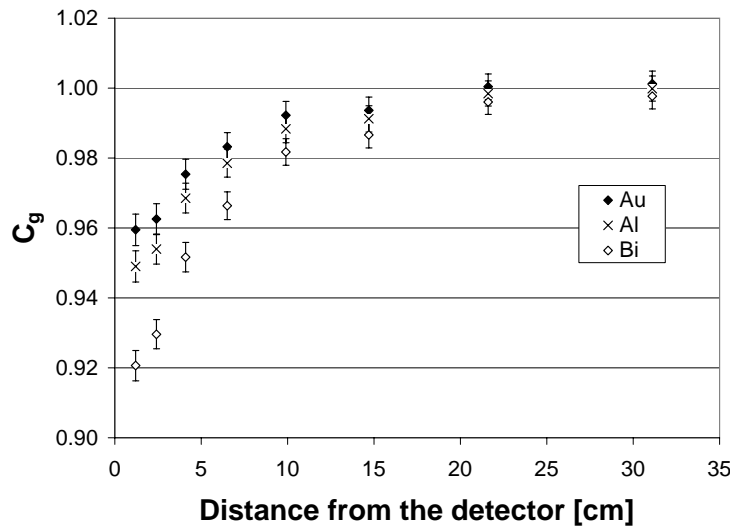


Figure 2.5: Geometrical correction factor (C_g) in the dependency of the distance from the detector for different foil dimensions.

The correction factors can be as well determined experimentally. The same radioactive source has to be measured in the furthest position, where the $C_g=1$, and at the distance, where the C_g is needed. Such measurements were performed for Al foils. The expected magnitude of correction in the scale of few percents was confirmed. Detailed course was lost in 5% systematical uncertainty of the measurements.

2.2.5 Self-absorption of gamma photons in the activation foils - C_s

The mass attenuation coefficients are for activation materials at 100 keV energies in orders of few cm^2/g . This means that self-absorption in even less than mm thick foils is significant.

The C_s factor accounts for self-absorption and can be expressed as the ratio between gamma fluxes from the foil with and without self-absorption:

$$C_s = \frac{\int_0^l \frac{I_0}{l} e^{-\mu x} dx}{\int_0^l \frac{I_0}{l} dx} = \frac{1 - e^{-\mu l}}{\mu l}, \quad (2.20)$$

where l is the foil thickness and μ is the factor of attenuation coefficient and foil density. It is assumed that the foil is placed perpendicular to the detector axis and enough far from the HPGe crystal that only photons emitted parallel to the detector axis reach the crystal.

The effect was also studied with the MCNPX simulations. The cases with and without self-absorption were in simulation approximated with the foils which volume was filled with the material and with air. The source of photons was distributed homogeneously in the foil volume. The efficiency $\epsilon_P(E)$ of the HPGe detector was simulated for energies of gamma photons ranging from 50-2000 keV and thickness 10-1000 μm of the foil material. The foil with dimensions $2 \times 2 \text{ cm}^2$ was placed 2.4 cm away from the detector.

In the Figure 2.6 are shown the ratios between the results for foils filled with material and air at different photon energies and foil thicknesses. The examples of some simulated results for the gold activation foils used at the experiments ($2 \text{ cm} \times 2 \text{ cm} \times 0.05 \text{ mm}$) are shown in the Table 2.1.

Table 2.1: Simulated factors C_s in gold foils. The foil dimensions used in simulation were $2 \text{ cm} \times 2 \text{ cm} \times 0.05 \text{ mm}$.

Radioisotope	Energy [keV]	C_s
^{195}Au	98.85	0.762
^{193}Au	186.17	0.945
^{194}Au	293.545	0.981
^{196}Au	332.983	0.985
^{198}Au	411.80205	0.990
	above 420	>0.990

The results of C_s calculation from the equation 2.20 and the MCNPX simulation were identical within statistical errors for all isotopes usually observed in activation foils at spallation experiments.

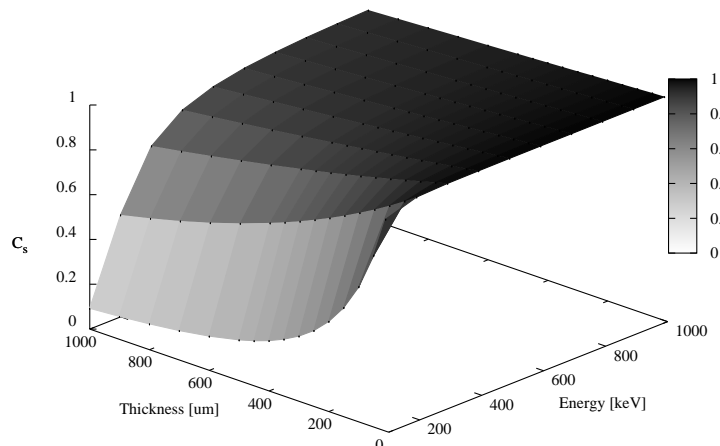


Figure 2.6: MCNPX simulation of the self-absorption coefficient C_s for gold activation foil. On X axis is the thickness of the foil, on Y axis is the energy of the gamma photons, and on Z axis is the self-absorption coefficient.

2.2.6 Cascade coincidences

The γ -decay of excited nucleus goes through several excited levels, emitting photons or conversion electrons at each step. At a single decay, more photons can be emitted at different angles and they can also deposit their energy in the detector simultaneously. This effect is known as cascade coincidence.

True coincidences occur when two or more cascading photons - emitted in the decay of a radionuclide with negligible time delay - give rise to a total or partial energy deposition in the detector.

Two or more photons registered in the detector can be also from different decays - false coincidences. Unless the intervals between the hits are smaller than the detector dead time (few μs , activities in orders of MBq), such coincidences are negligible.

The probability that more photons are emitted to solid angle towards the detector decreases with the distance from the detector, and true coincidences are significant only at small source to detector distances.

Cascade coincidences can change the area under gamma peaks in two ways:

- More photons from the decay deposit their energy in the detector. The area of the observed peaks is smaller (for a factor L), the energy is deposited in channels corresponding to higher energies. Smaller peaks and corresponding background arise at the sum of the energies of photons, see Fig. 2.8.

- The nucleus can decay from one state to another directly by emitting one photon or in several steps, emitting photons at each step. The sum of the energy of photons corresponds to the energy of the photon in the single step. If all photons fully deposit their energy in the detector, the peak area of the single step photon will be increased (for a factor S).

Corrections for cascade coincidences can be avoided if the same radioactive isotopes are used for the calibration and for the measurement. The correction can also be determined experimentally with the measurements at different distances from the detector. The cascade coincidences at large distances are negligible (the probability that two photons from the same decay are emitted into the solid angle towards the detector is small).

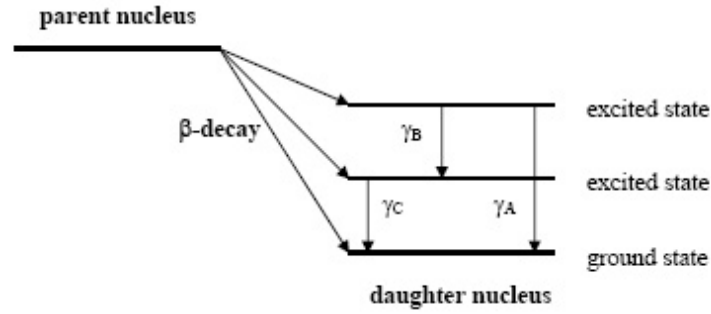


Figure 2.7: Decay scheme with lines A, B and C.

The basic calculation procedure of the correction factor is described elsewhere [58, 59]. In brief, the correction factor for the example shown in the Figure 2.7 is given as:

$$COI = (1 - L)(1 + S), \quad (2.21)$$

where coefficients L and S are:

$$L(B) = a_C c_C \epsilon_T(C), \quad (2.22)$$

$$S(A = B + C) = \frac{I_B}{I_A} a_C c_C \frac{\epsilon_P(B) \epsilon_P(C)}{\epsilon_P(A)}. \quad (2.23)$$

Factor $c_C = (\alpha_C + 1)^{-1}$ is the probability that the photon will be emitted at the transition (conversion electron is another possibility, α_C is the conversion coefficient and is the ratio between the irradiation probabilities of the conversion electron and gamma photon), and a_C the probability that the transition C will happen from all possible transitions from a given state

The simulations of cascade coincidences with the FLUKA Monte Carlo code

For the simulations of the cascade coincidences, the source which emits more photons in a single history needs to be implemented in the code. The implementation to MCNPX seems very difficult, while the FLUKA code already contains subroutines, which were only slightly changed to emit more photons in one history. The electromagnetic part of the FLUKA code is almost identical to the one in the MCNPX code, what was also verified with some simulations from previous sections that were repeated with FLUKA and the same results within statistical uncertainties were obtained.

For cascade coincidence related simulations, the detector was simplified with a Ge cylinder with 4 cm diameter and 5 cm length. Both efficiencies (ϵ_T and ϵ_P) were simulated for few distances of the radioactive source from the detector (1, 5, 10 cm), and calculated efficiencies were fitted with appropriate exponential functions (Sections 2.2.2 and 2.2.3).

In the next step, FLUKA subroutine *source.f* was modified to release in each history one of the photons from the studied radioactive decays (radioactive isotopes ^{60}Co and ^{133}Ba were studied). The probabilities of the choice of the emitted photon energy were set to absolute intensities of the gamma lines, taken from the ENDL database [61]. The spectrum of the energy deposited in the detector corresponds to the theoretical case where there are no cascade effects (Figure 2.8).

The subroutine *source.f* was then modified to emit more photons in the same history (as in the real radioactive decay) and the response of the detector was simulated. Two cases were simulated, the first one with both photons emitted isotropically (without the correlation between their directions) and the second with the correlation between the angular distribution of emitted photons. The distribution of solid angles between the photons is generally defined by the equation:

$$W(\theta) = \sum_{\nu} A_{\nu}^{(1)} A_{\nu}^{(2)} P_{\nu}(\cos \theta), \quad (2.30)$$

where P_{ν} are Legendre polynomials, and coefficients $A_{\nu}^{(1)}$ and $A_{\nu}^{(2)}$ are functions of multiplicities and spins of the radiations. The detailed explanation of the angular distribution correlation is beyond the scope of this work, and can be found in textbooks, eg. [62]. For example, in the decay of isotope ^{60}Co two photons are emitted and the distribution of the solid angle

between them is correlated with the following function:

$$\begin{aligned}
 W(\theta) &= 1 + A_2 P_2(\cos \theta) + A_4 P_4(\cos \theta) = \\
 &= 1 + 0.1020 \cdot \frac{1}{2}(3 \cos^2(\theta) - 1) + \\
 &+ \frac{0.0051}{8}(35 \cos^4(\theta) - 30 \cos^2(\theta) + 3) \quad (2.31)
 \end{aligned}$$

The spectra from different simulation steps were compared to the spectrum with one photon in each decay, and the correction for the cascade effects was defined as:

$$COI = \frac{S_1}{S_r}, \quad (2.32)$$

where S_1 is the area under the peak obtained with the simulation where one photon was emitted in the history, and S_r is the same area for the simulated realistic decay.

At the closest distance of the radioactive source from the detector (1 cm), the correction for cascade effects was up to 12%. The factors simulated with angular correlation differ for less than 1% from the factors without angular correlation. The simulation with angular correlation was repeated with the first multiplier (A_2) set to 0.3 instead of 0.1020. For the big majority of decays 0.3 is the upper limit for this multiplier [63]. The factors calculated with $A_2 = 0.3$ differ for 2% from the correction factor without angular correlation.

The COI corrections at the distance 5 cm are less than 5% and at the distance 10 cm less than 2%. The numbers calculated with FLUKA code were compared to the numbers obtained by two analytical calculation procedures mentioned in previous paragraphs. Simulated ϵ_T and ϵ_P were used in equation 2.21-2.29. For both studied isotopes (^{60}Co and ^{133}Ba) the identical results (comparing to FLUKA simulation without angular correlation) for COI corrections were obtained within 0.5%. It should be noted that analytical procedures do not include angular correlations between emitted photons, but the corrections because of these correlations are small ($\approx 1\%$).

2.3 Production of radioisotopes

2.3.1 Spectra of produced particles and cross-sections

Beside neutrons, the following particles are produced in the spallation reaction: protons, photons, pions and heavier fragments (d,t ...). These particles all contribute to the production of the measured radioisotopes and it is important to have a figure on their influence.

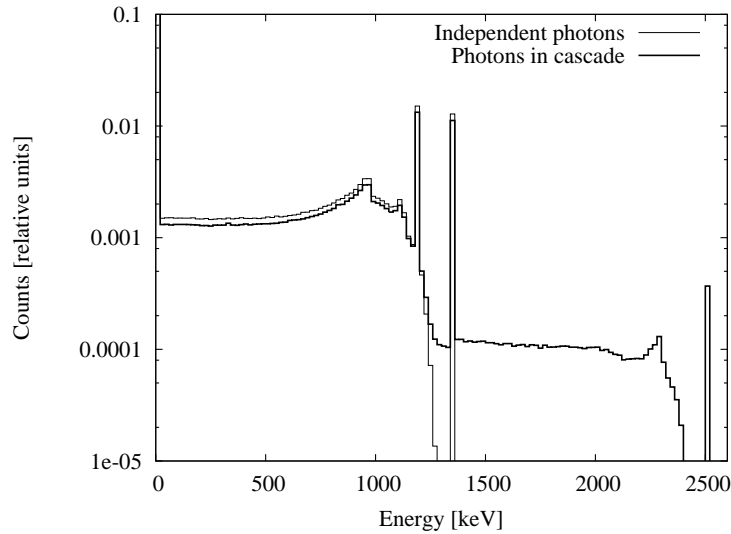


Figure 2.8: FLUKA simulation of the detector response to the ^{60}Co source placed 1 cm from the detector front. For the case when two photons are in cascade, the area under the peaks is decreased (for the factor COI) and another peak at the sum of the energies of both photons appears.

The example of the calculated spectra of the particles produced in the spallation is seen in the Figure 2.9. The spectra of neutrons, protons, deuterons, charged pions and photons were calculated with MCNPX, with 1 GeV deuteron beam directed to the lead target of 50 cm length and 5 cm radius. Another simulation with the same target surrounded by 2 m of water (moderator) is referred as "water bath" case. At experiments, targets are placed in the moderating environment (concrete walls, soil), and neutron spectrum obtained in the "water bath" simulation should be closer to the reality than in the bare target case. The influence of the moderator on the spectra of other particles is negligible. From the Figure 2.9 it is seen that mostly neutrons are produced, the production of protons and photons is suppressed for one order of magnitude (protons - Coulomb barrier, photon emission competes with neutron emission only in the last phase of the spallation reaction), the production of pions is strongly suppressed in our beam energy range.

The produced neutrons interact with the activation material through (n,xn) and (n,γ) reaction channels, protons through $(p,p(x-1)n)$... An example of the cross sections for $^{197}\text{Au}(n,2n)^{196}\text{Au}$ reactions (and their equivalents that produce the same radioisotope with protons, pions and photons) are shown in Figure 2.9. Reactions (n,xn) with higher x have similar shape

of the cross sections, but the threshold is placed towards higher energies (thresholds for (n,2n), (n,3n), (n,4n) reactions are 8.1 MeV, 14.8 MeV, 23.2 MeV). Another reaction with similar shape of the cross sections is (n, α) in Al with the threshold at 3.2 MeV. Low energy neutrons ($0.1 \text{ eV} < E_n < 0.1 \text{ MeV}$) which are not produced in the spallation reactions in large quantities (but there is always plenty of them as a result of the moderation in the shielding materials or moderator) interact with the activation material with (n, γ) reactions.

2.3.2 Influence of other particles

The production rates $B(A)$ are obtained by folding the spectra and appropriate cross sections from Figure 2.9. The particles other than neutrons will give small but not negligible contribution to the total production rate. At the typical (for spallation experiments) beam energy of 1 GeV, the contribution from photons and pions can be usually neglected, as they contribute less than 1%. On the other hand, protons and deuterons (in the case when deuteron beam is used) can contribute few percents. These contributions are strongly dependent on the placement of the activation foil. A test simulation was performed which shows that in certain conditions, proton influence can reach tens of percents.

In the simulation, the target was divided to two parts (15 cm + 35 cm) with 1 mm gap between them. 1 GeV narrow, deuteron beam was directed to the target and spectra sampled in the gap were folded with the appropriate cross sections. It was found out that e.g. 20% of radioisotope ^{192}Au was produced with protons, 5% with deuterons, while pion and photon contributions were below 1%.

Therefore, the contributions to $B(A)$ from the reactions with other secondary particles should always be considered at the spallation experiments. The same is valid for reactions of type (n,f), (n, α) ... in other activation materials. The exception is (n, γ) reaction, which is sensitive to low energy neutrons only ($0.1 \text{ eV} < E_n < 0.1 \text{ MeV}$).

2.3.3 Dimensions of the foils

The minimal mass of the foil material is determined by the number of activated nuclei that can be detected with the HPGe detector. The gamma peak from the radioisotope should be visible in the spectrum background, which usually increases with the rate about at least 1 count/minute in a channel around the energy 500 keV.

In our commonly used conditions, after one hour of the background measurement, the expected number of counts in that channel will be with 98% probability $60 \pm 3\sigma = 60 \pm 3\sqrt{60} = 60 \pm 23$. The count rate from the radioactive isotope in one channel should be more than 23 counts per hour if it should be distinguishable from the background. Because the energy resolution of the detector is around 2-3 keV, the peak can be registered in the neighbor channels covering 2-3 keV range, what is around 10 channels in our case. In these channels more than 23 counts per hour are required, in total ≈ 230 counts (for this estimation the peak is approximated with a step function and not with the Gaussian function).

The background usually grows much faster when the radioactive material is measured. Setting at least 1000 counts per hour in the peak for the lowest detectable limit is a realistic estimation in our case.

The peak efficiency of the HPGe detector around the energy 500 keV is around 1% (Section 2.2.2). If a photon is emitted at every decay of the radioactive isotope and 1000 counts should be registered during one hour, approximately $2 \cdot 1000 \cdot \frac{1}{1\%} = 200000$ nuclei need to be activated, assuming that $\tau_{1/2}=1$ hour¹. In practice, there are more foils to be measured with the HPGe detector, and most of them are not measured immediately after the irradiation, but few decay periods after it. Usually, one order of magnitude higher number of activated radioisotopes during the irradiation is necessary for the reliable measurement.

For example, at the spallation experiments performed in the JINR, $B(A)$ rates are in orders of 10^{-6}p^{-1} and proton integrals are 10^{13} . This means that in 1 g of the material 10^7 radioisotopes will be produced during the irradiation, what is easily measured. The activation material is in the form of thin foils with sides 2×2 cm² and thickness from 50 μm up to 1 mm. The masses of such foils are 0.4-6 g.

Small foils

The foil is supposed to be small, so that the measured quantity does not change considerably in different parts of the foil. The simulations of the experiments discussed in [64, 65] showed that the changes in the neutron flux on the cm scale can be as high as 50%. This is much more than the accuracy of the activation method and foils with the dimensions on the cm scale cannot be considered as small. The foils on the mm scale are small at such experiments.

In the simulations the foil dimensions can be implemented and the neu-

¹counts=decays $\cdot\epsilon_P$, decays= $N_0 - N_0e^{-\lambda\tau_{1/2}} = \frac{1}{2}N_0$

2. NEUTRON ACTIVATION ANALYSIS

tron flux can be averaged over the whole place of the foil. That compensates for the fact that the foils are not small when simulated values are compared with experimental results. As more foils are usually placed next to each other in experiments, the measured values can also be interpolated.

Thin foils

The foils should be thin enough not to disrupt the measured neutron fluxes. In general, even 1 mm thick activation foils are thin enough for MeV neutrons (cross sections for (n,xn) reactions are maximally in orders of barns), but not also for low energy neutrons (cross sections for (n, γ) reactions are up to thousands of barns).

The simulation with the neutron spectrum from the Figure 2.9 (water bath case) directed to the gold activation foils with thicknesses from 10 μm up to 1 mm was performed. The neutron spectra sampled in the gold foil were folded with cross sections for (n,xn) and (n, γ) reactions. While in the case of (n,xn) reactions the obtained production rate did not change, in the case of (n, γ) reaction the production rate decreased significantly with the thickness, see Figure 2.10. Again, the absorption is taken in account in the simulations if the foil dimensions are properly implemented. For experimental data, the factor for which the production rates are lower due to absorption can be calculated. This conclusion can be applied also to other reactions which have similar cross sections to (n, γ), for example (n,f) reactions.

Transport of activated material out of foil

In the case of very thin foils, the loss of activated material from the foil can also become significant and needs to be discussed. At the (n,xn) reaction, the activated nucleus can obtain the kinetic energy up to few tenths of MeV. Such nuclei can have the range of few μm in the detector material, can move out of the foil material during the irradiation.

The electronic stopping power of Au in Au reaches maximally ca. 40 MeV/(mg/cm²) at 10 MeV (Figure 2.11). Assuming that this value does not change at slowing down, the distance travelled by radioisotope is $\frac{E}{S_p} \approx 0.1\mu\text{m}$. Therefore, with the thickness of the foils, which is minimally 50 μm , we can estimate that less than 1% percent of radioisotopes escape from the Au foils.

The irradiation of the 50 μm gold foils with quasimonoenergetic neutron beam of 36 MeV at the NPI Cyclotron showed that this presumption is an overestimation. The foil was wrapped in thick paper and scotch tape envelope, which should stop all the escape radioisotopes. The paper and the foils were measured separately and the number of the nuclei in the foil was 4

orders of magnitude lower than in the paper. The escape of the radioisotopes can be therefore considered as negligible. In any case, it can be avoided by packaging the foils in envelopes that stop the escaping fragments.

2. NEUTRON ACTIVATION ANALYSIS

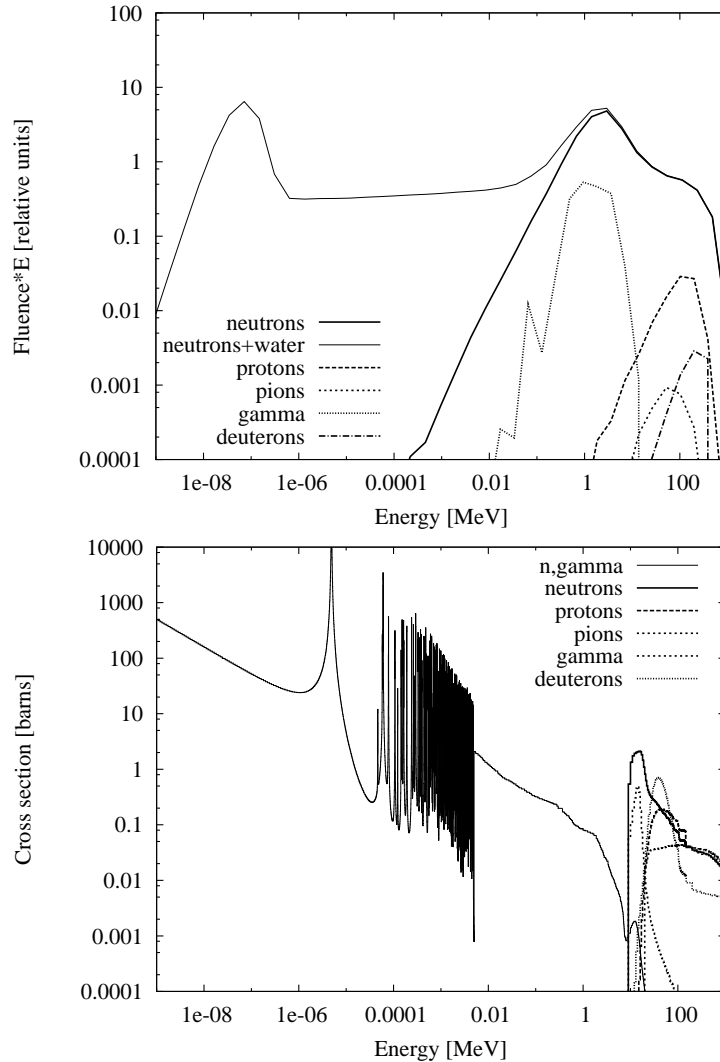


Figure 2.9: Spectra of produced secondary particles in the spallation reaction (above). The beam of 1 GeV deuterons was directed to the lead target (length 50 cm, radius 5 cm). The neutron spectrum simulated with the target surrounded by 2 m of water is referred as "neutrons+water".

Cross sections for reactions with neutrons, protons, photons, pions and deuterons in which ^{196}Au is produced (below). The energy scale (X axis) corresponds to the spectra presented above. Cross sections were calculated with TALYS 1.0 code, with the exception of pions (MCNPX code, CEM03 model) and data for (n,γ) reaction[41].

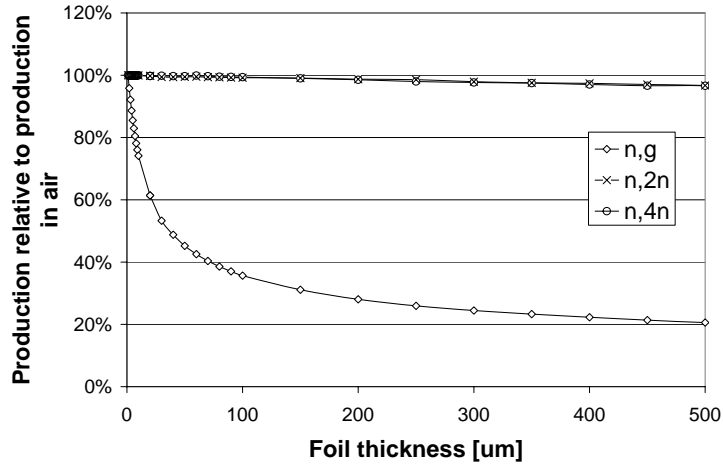


Figure 2.10: Ratio between the production rates for (n,xn) and (n,γ) reactions in the gold foils with different thicknesses and the production rates in the foils filled with air (no absorption). The neutron spectrum from the Figure 2.9 (water bath case) was used in the simulation.

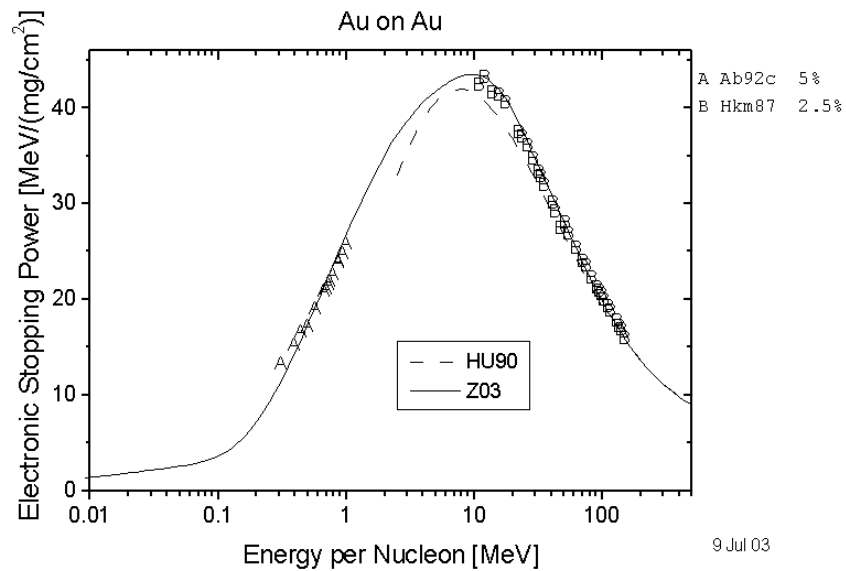


Figure 2.11: Electronic stopping power for Au in Au [66, 67].

Chapter 3

Phasotron experiment

The experiment on a bare, lead target, which was performed in November 2003, was focused on the spatial distribution of high energy neutrons ($E > 10$ MeV), and the transmutation of radioactive iodine ^{129}I in such neutron spectrum. The intensive beam of protons and short irradiation time allowed the studies short living isotopes produced with high order (n,xn) reactions in activation foils and samples. Relatively simple setup provided a set of useful data about the spallation on a thick target for simulation benchmarks.

I performed the analysis of the experimental data using the method explained in the previous chapter. I then implemented the setup to MCNPX and FLUKA codes, studied the accuracy of obtained experimental results and compared them to simulated values.

3.1 Experimental setup and results

3.1.1 Experimental setup

The setup consisted of a cylindrical lead target with the radius 4.8 cm and length 45.2 cm, placed at the end of the concrete corridor with length of 20 m, height and width 2 m and 2 m thick walls (Figure 3.1). The target was separated in two cylindrical parts (with lengths 12.3 cm and 32.9 cm) and 0.7 cm air gap between them. Both parts were made of smaller segments (in cm: 4.7, 3.8, 3.8, gap 0.7, 3.3, 4.6, 4.3, 4.2, 3.9, 4.8, 3.8, 4).

Activation detectors, made of Al, Au, and Bi thin foils (dimensions $2\text{ cm} \times 2\text{ cm} \times 0.05\text{ mm}$ for Al and Au foils and $2.5\text{ cm} \times 2.5\text{ cm} \times 1\text{ mm}$ for Bi foils), were placed on top of the setup along its whole length. Au and Al foils were placed every 2 cm from the beginning of the target and Bi foils were placed on the 1st, 9th, 21st, 31st, and 43rd cm. Five sets of Al and Au

3. PHASOTRON EXPERIMENT

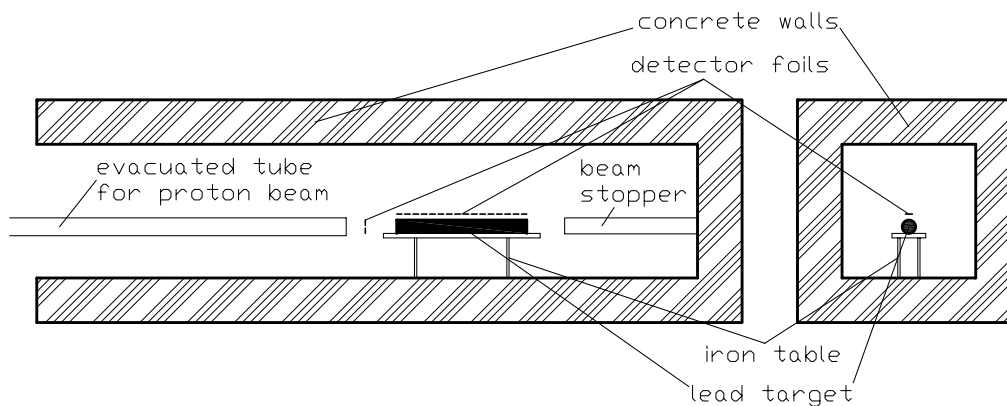


Figure 3.1: The layout of the Phasotron experimental setup. Longitudinal (left) and transverse (right) cross-sections.

activation foils were placed in the gap, one foil set on the target central axis and four sets around it, forming a cross with ca. 3.5 mm space between the foils, as seen in Figure 3.3a¹. In front of the target were placed foils for the measurement of the beam integral made of bigger Al and Cu foils (8 cm × 8 cm × 0.1 mm).

High energy neutrons produced during the irradiation were at the same time used for the studies of transmutation of radioactive isotope iodine ¹²⁹I. Four iodine samples were placed on top of the setup, two samples at 9th cm and other two samples at 21st cm. Each pair of the samples contained a sample with natural iodine (¹²⁷I) and another with iodine from the nuclear waste (mixture of 17% ¹²⁷I and 83% ¹²⁹I) in the form of NaI. ¹²⁷I samples were in the form of solid cylindrical tablets (with radius and thickness: $r = 1.05$ cm, $h = 0.3$ cm), and ¹²⁹I samples were prepared from NaI powder packed in Al shielding [68]².

After 10 minutes of irradiation with the proton beam of approximate intensity (10^{13} protons/s), the foils and samples were collected from the setup. Their gamma spectra were measured with the HPGe spectrometers. The foils were measured twice, soon after the irradiation for a short time, and after the decay of short living isotopes for a longer time. The iodine samples were measured ≈ 10 times. Gamma spectra of radioisotopes with decay times from few minutes up to some days were registered. The spectra were analyzed us-

¹Shortly before the experiment, these foils were manipulated and it is possible that they were not centered after that.

²The aluminum shielding was remodeled for this experiment to provide reasonable safety at the minimum of Al used.

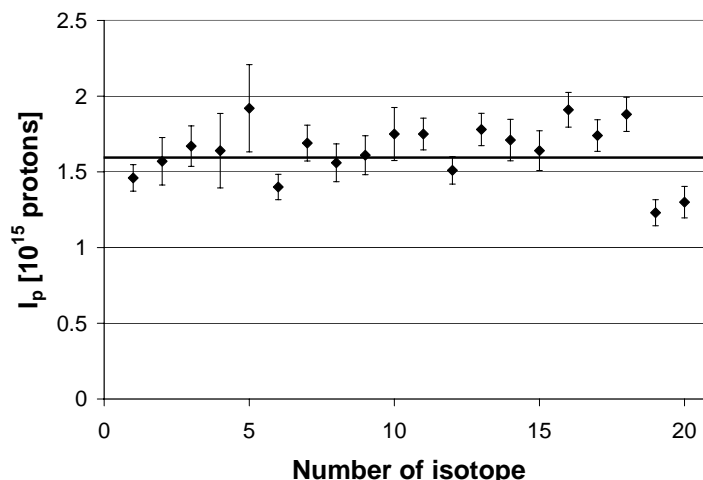


Figure 3.2: The integral proton flux results from different radioisotopes produced in Al and Cu foils. For radioisotope numbers see Appendix, Table 1.

ing the method described in Part 2 and the amount of activated/transmuted material in the foils was determined. The quantity introduced as the production rate $B(A)$ - the mass of activated isotope A per one incident proton and per 1 g of foil material - is used to present the results.

3.1.2 Experimental data - beam parameters

During the irradiation, the beam was monitored with the wire chamber placed at the end of the beam tube. The wire chamber showed that after ten minutes of constant irradiation, the beam centered to the central target axis, with the intensity of ca. 10^{13} protons/s and with horizontal and vertical diameters of 1.6 cm and 1.9 cm was produced.

Independently, the beam integral was measured with the activation foils, big Al and Cu foils, placed in front of the target. Their analysis showed that isotopes ^{24}Na (not used for the determination of the beam integral, part of it is produced by neutrons) and ^7Be are found in Al foils and ^7Be , ^{24}Na , ^{42}K , ^{43}K , ^{44}Sc , ^{44m}Sc , ^{46}Sc , ^{47}Sc , ^{48}Sc , ^{48}V , ^{51}Cr , ^{52}Fe , ^{52}Mn , ^{54}Mn , ^{55}Co , ^{56}Co , ^{57}Co , ^{58}Co , ^{57}Ni in ^{nat}Cu foil. From the production rates and the cross sections for this isotopes (taken from EXFOR [69] and extrapolated to 660 MeV if necessary) the number of protons was calculated. Mean weighted average value of the integral proton flux was determined to be $1.58 \cdot 10^{15}$ protons with the accuracy of 6% (cross-section uncertainties), see Figure 3.2.

The beam diameter and displacement from the central axis were measured with the cross of five sets of Al and Au foil sets placed in the gap between

3. PHASOTRON EXPERIMENT

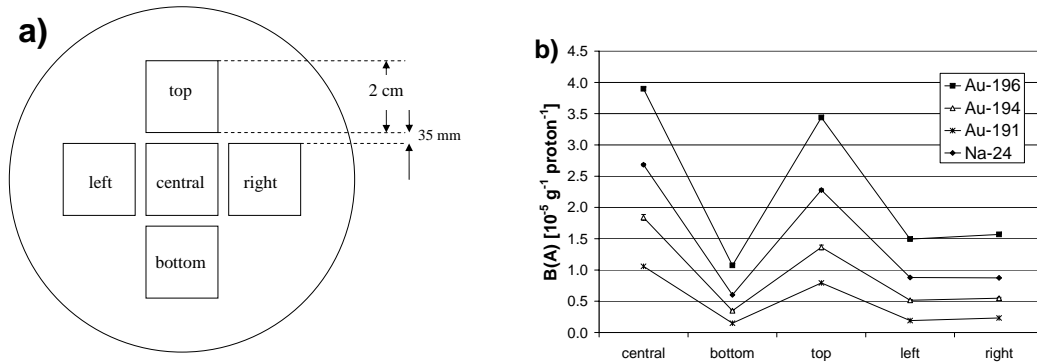


Figure 3.3: The placement of the five sets of Al and Au foils in the gap (a) and production rates (b) for ^{24}Na in Al foils and $^{191,194,196}\text{Au}$ in Au foils in them (uncertainties of the fitting of gamma peaks are not seen on this scale).

the target sections. The production rates are shown in the Figure 3.3b. Comparing the rates in different foils, one can conclude that the beam had the elliptical shape (the ratio between the horizontal and vertical axis was around 0.6:1) and that the center of the beam was somewhere between the central and the top foil. Shortly before the experiment the whole cross with the fixed foils was manipulated and was possibly displaced from the target center (discussed in the Section 3.3.1). The information about the beam position from the foils is therefore not reliable, however, the beam profile information is valid and is in the agreement with the data from the wire chamber.

3.1.3 Experimental data - spatial distribution of neutron field

In the foils used for the measurement of longitudinal distribution of high energy neutrons were found the following isotopes: in Al foils ^{24}Na , in Au foils ^{189}Au - ^{196}Au , ^{198}Au and in Bi foils ^{201}Bi - ^{206}Bi . The production rates against the position along the target are plotted in Figures 3.4a, 3.4b, and 3.4c for all three types of foils. The error bars are only statistical uncertainties of the gamma peak approximation with Gaussian curve.

The graphs show the specific shape: the maximum at around the 8th cm, and the point near the 30th cm, where the neutron field starts to decrease faster. The second point coincides with the range of 660 MeV protons in lead - protons with such energy are stopped due to ionization losses after 31 cm of lead material according to calculation (Fig. 3.4d) [70]. After ca. 30 cm of the lead, there is no more spallation by primary particles, what is seen as a

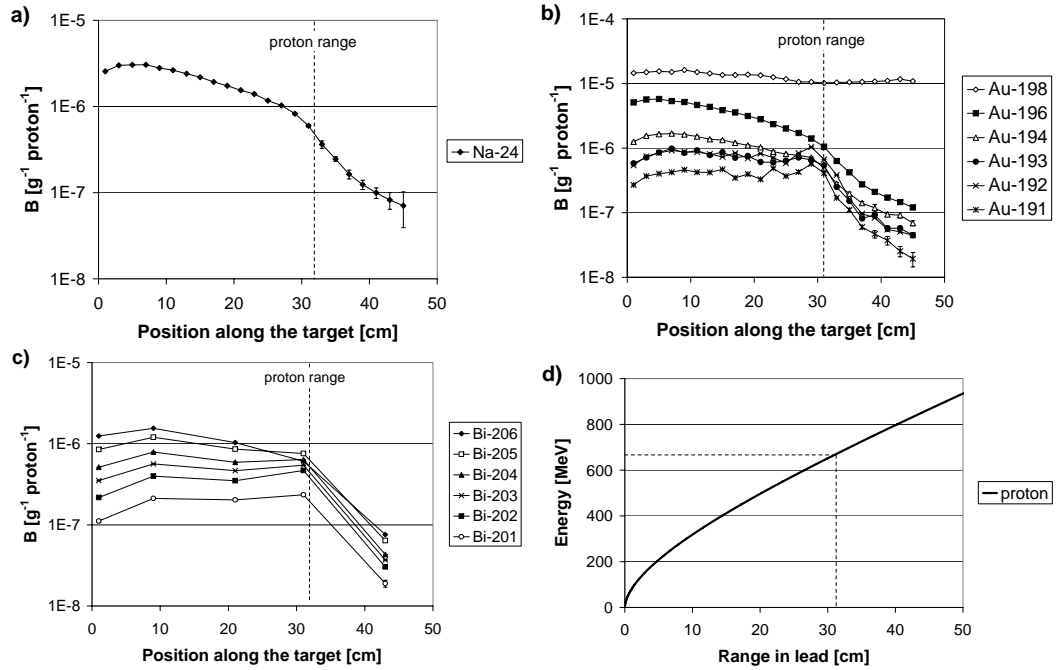


Figure 3.4: B-values for ^{24}Na in Al foils (a) and different isotopes in Au (b) and Bi (c) foils along the target (uncertainties in the graphs are only the uncertainties of the fitting of gamma peaks). The values from the graphs are printed in the Appendix, Tables 2,3, and 4. In (d) is shown the proton range in lead in dependency of the energy [70].

fast decrease of production rates after this point.

The graph for ^{198}Au , which is produced through (n, γ) reaction channel by low energy neutrons shows almost constant production along the target. The neutrons that contribute to the ^{198}Au production are neutrons from the spallation and the neutrons that are moderated by concrete walls and partly reflected back. The reflected neutrons create an almost homogenous low energy neutron field around the target, contributing to the ^{198}Au production from 20% at the beginning of the target up to 95% near the end of the target (discussed in section 3.2.1). With the subtraction of the homogenous background (95% of the $B(A)$ near the end of the target) from experimental ^{198}Au values, the low-energy neutron distribution from the target only is obtained, which is similar to the threshold reactions distributions, eg. ^{189}Au - ^{196}Au .

3. PHASOTRON EXPERIMENT

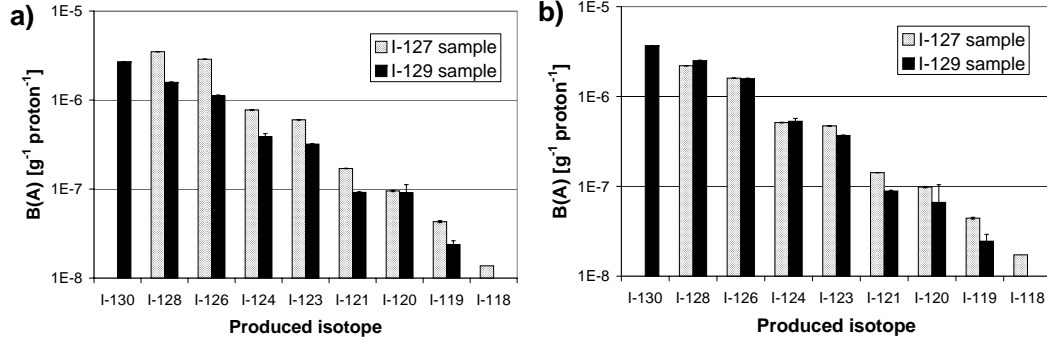


Figure 3.5: B-values for different isotopes in ^{127}I and ^{129}I . Samples were placed at the 9th (a) and 21st cm (b).

3.1.4 Experimental data - transmutation of iodine

The main interest in the experiment was to measure the production rates of higher order reactions in iodine - $(n,5n)$, $(n,6n)$,... reactions. Actually, the yields of produced isotopes up to ^{118}I - $(n,10n)$ - were determined with the accuracy of 10%, and the products decayed from iodine isotopes up to ^{116}I - $(n,12n)$ - were detected. The yields of produced isotopes for ^{129}I were calculated with the subtraction of ^{127}I contribution in the samples with the mixture of radioactive and stable iodine.

The graphs in Fig. 3.5 show the production rates of measured iodine isotopes at the 9th cm and the 21st cm for ^{127}I and ^{129}I . The production rates lie in the range between $10^{-8} \text{ g}^{-1} \text{ proton}^{-1}$ and $10^{-5} \text{ g}^{-1} \text{ proton}^{-1}$.

3.2 Simulations - systematic uncertainties of experimental results

To obtain the idea about possible systematic uncertainties of obtained data, the detailed simulation of the experiment was performed. The experimental setup was simulated using the MCNPX and the FLUKA code. In the simulations, the target was approximated with the lead cylinder with its real dimensions and the concrete with 2 m thick walls. The beam tube, the beam stopper and the table on which was placed the setup were approximated with an evacuated iron tube ($r = 10 \text{ cm}$, $d = 0.5 \text{ cm}$, ends 30 cm before the target), full iron tube ($r = 10 \text{ cm}$, starts 55 cm after the target) and iron plate (1 cm thick, $1 \text{ m} \times 0.5 \text{ m}$), respectively. The activation foils were approximated with thin foils with realistic dimensions and the samples were approximated with realistic thin cylinders (enveloped in aluminum shielding

- ^{129}I samples).

In the simulations with the MCNPX code package two cascade models (CEM03, INCL4/ABLA) and LA150 libraries were used. In FLUKA, the preequilibrium-cascade model PEANUT and FLUKA's own cross section libraries (for materials used at this experiments imported from ENDF/B-VI) were used.

Neutron and proton fluences in the foils and iodine samples binned in 1 MeV energy intervals (1-150 MeV, 50 MeV bins above 150 MeV) were calculated. These fluences were convoluted with the (n,xn) cross sections calculated with the TALYS-1.0 code (and MCNPX code using CEM03 model for energies higher than 150 MeV) in order to obtain the production rates $B(A)$.

3.2.1 Influence of the setup parts and experimental conditions

In the first step, the MCNPX (CEM03 cascade model) simulation was done with the narrow, central beam and the obtained results were compared to the experimental measured values. Most experimental values were described well, with the two points mentioned in 3.1.3 (maximum at 10th cm and faster decrease of production rates after 30th cm) at the right places, and with the differences between experimental and simulated production rates which were within 30%.

In the next step, a set of MCNPX simulations with changed setup parameters was performed in order to study the influence of the setup parts such as concrete walls and iron components on the experimental results, and to estimate the systematic uncertainty of the experimental results (mainly because of the beam parameter uncertainties).

Concrete walls and iron parts

Concrete walls moderate neutrons coming from the target and reflect part of moderated neutrons back to the setup place, thus they produce an almost homogenous field of low energy neutrons around the target. Calculated neutron spectra along the target for the case with the walls included and for the case without walls are seen in the Figure 3.6 together with the ratios between them. It is important to stress that the high energy part of the produced neutron spectrum is not changed due to the walls (the ratio between the spectra is 1 within the error bars), there is no physical mechanism how high energy neutrons could be reflected back to the setup. The same conclusion applies also to protons. Calculations of production rates of threshold reactions for

3. PHASOTRON EXPERIMENT

the setup with and without walls confirmed that the results do not differ outside the statistical uncertainties which were 2%. One can conclude that the walls have no influence on high energy neutron field (and on production rates in threshold foils).

However, the walls change significantly the neutron field for neutrons with energies < 100 keV. These low energy neutrons around the target have two sources: the spallation process in the target, and the moderation, reflection in the concrete walls. The spatial distribution of the spallation neutrons is the same as for neutrons with energies > 1 MeV, however, the neutrons scattered from the concrete walls create a homogeneous low energy neutron field along the target length. The reflected neutrons are outnumbered by the neutrons coming from the target, but, the cross-section for ^{198}Au production decreases very fast with the energy. In terms of ^{198}Au production, this means that the small number of reflected neutrons contributes from 20%-95% to the production rates (at the beginning and at the end of the target, respectively), as seen in the Figure 3.7a and 3.7b.

The comparison of simulated and experimental values shows that the simulations underestimate the ^{198}Au production for the factor of 1.5-3 as seen in the Figure 3.11. This is due to unsatisfactory description of the background produced by neutron scattering on the concrete walls. Due to inaccurate description of the walls, the simulation underestimates this background. However, we assume that the prediction of the homogeneous background is correct. The constant contribution from the walls was therefore added to the simulated values and the corrected values describe the experimental values quite well. Figure 3.8 shows another comparison of the experimental $B(^{198}\text{Au})$ values with the subtracted background and the simulation of the ^{198}Au production rates on a bare target.

In the iron parts of the setup, a mechanism that could change the high energy neutron field exists. Heavy Fe nuclei can scatter neutrons, and additionally, in spallations or (n,xn) reactions in iron, more neutrons can be produced. Calculations were performed to estimate the importance of these effects. A simulation was performed with the iron parts approximated as described in the introduction of Section 3.2, and another where iron parts were replaced with air. It was found out that iron parts have negligible influence on threshold and (n,γ) reactions. With the iron parts included, the production rates after 30th cm are 5% lower than without iron (statistical uncertainties are 5%).

3.2. Simulations - systematic uncertainties of experimental results

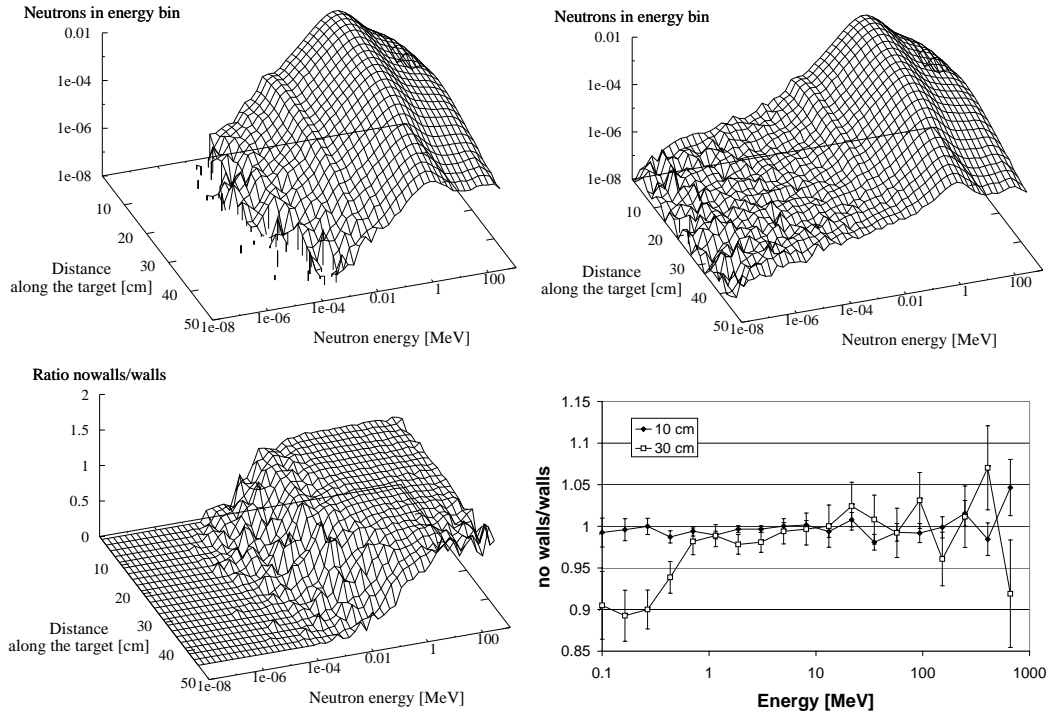


Figure 3.6: The neutron spectra along the target length calculated with MCNPX CEM03. The left upper figure shows the case without the concrete and the right upper figure shows the case, where concrete walls moderated fast neutrons and reflected part of them back to the setup creating almost homogenous low energy neutron background. On the lower figures are plotted the ratios between the calculated spectra for the setup without and the setup with concrete walls. On the left are the ratios for the whole energy spectrum along the target, and on the right are shown the ratios between spectra at energies 0.1-660 MeV at positions 10 cm and 30 cm from the beginning of the target. Concrete walls have no influence on the neutron spectra in the energy range 1-660 MeV.

3. PHASOTRON EXPERIMENT

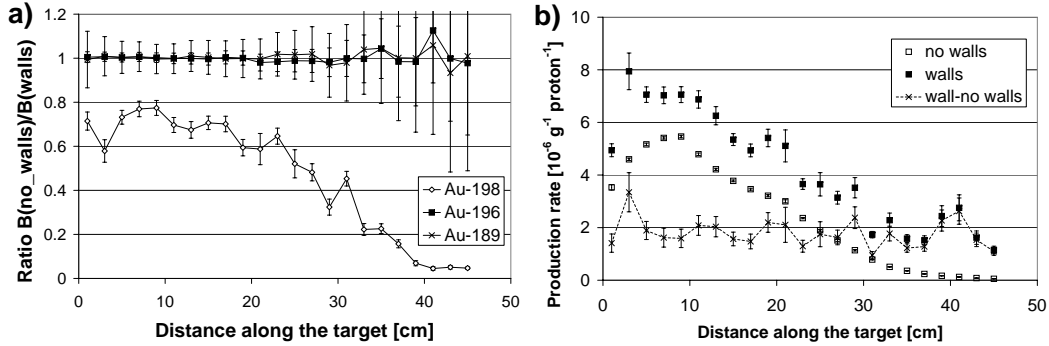


Figure 3.7: a) The ratios of the production rates of ^{198}Au , ^{196}Au and ^{189}Au along the target simulated with MCNPX for the cases with and without concrete walls. ^{198}Au is produced from 20-90% by the moderated neutrons from the concrete walls, but $^{196-189}\text{Au}$ are produced only by neutrons from the target, concrete walls have no influence on their production rates. b) The production rates of ^{198}Au along the target simulated with MCNPX for the cases with and without walls. It can be seen that the contribution of the neutrons reflected from the concrete walls is more or less homogenous.

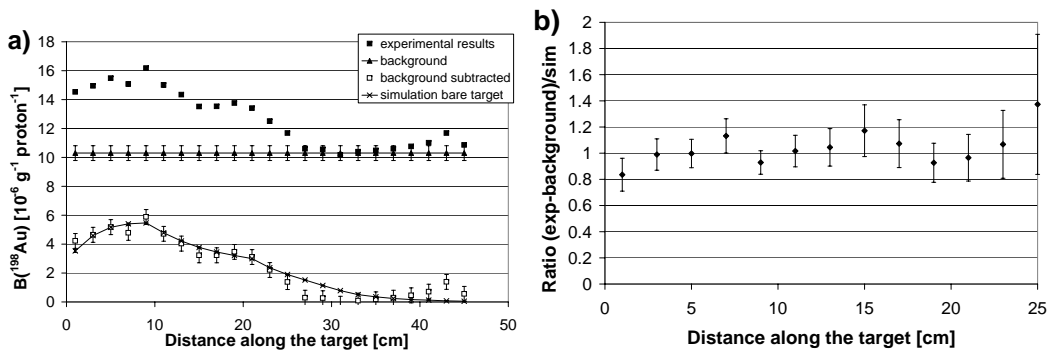


Figure 3.8: (a) Experimental and simulated B-values for ^{198}Au along the target. The background is approximated with a value near the end of the target. The experimental values with subtracted background are close to the simulation with a bare target (without concrete walls). In (b) are shown the ratios of the experimental values with background subtraction and simulated values. The ratios are up to 25th cm, from that point the ^{198}Au production is dominated by the neutrons from the concrete walls and the subtraction procedure does provide accurate values.

Beam parameters

Several simulations with miscentered beams and different beam profiles were compared. The beam was at first approximated with a point beam, directed to the center of the target. In the following five simulations, the beam was displaced every time for 0.3 cm upwards. This direction should have the biggest influence on the results - it is the direction towards the foils placed on top of the target. In the foils on top of the setup and iodine samples the increase in production rates for non-threshold reaction (n,γ) was 10% for each displacement. For the threshold reactions, the increase at every displacement was 10% and 15% for $(n,2n)$ and $(n,10n)$ reactions, respectively. The differences are significant only up to the 30th cm, which is the range of the proton beam.

Then another direction of the displacement was chosen, the beam was displaced to the left. It was found out, that displacement to the left has much lower influence on the results: the displacement of the beam for 1.5 cm lowered the production rates (threshold and non-threshold reactions) for less than 10%.

Finally, the calculations with the beam approximated with the Gaussian profile with $\text{FWHM} = 2$ cm and $\text{FWHM} = 4$ cm were compared to the first simulation with the point beam. The production rates increased with the width of the beam. For the beam with $\text{FWHM} = 4$ cm, the increase is 15% and 40% for $(n,2n)$ and $(n,10n)$ reactions respectively. The changes are significant only in the foils at the beginning of the target, after the 10th cm, the changes are much smaller. For the beam with the $\text{FWHM} = 2$ cm (the experimental beam had smaller FWHM than 2 cm), no changes were observed from the point beam. The beams with the cylindrical shape behave similarly as those with the Gaussian profile.

As the profile and horizontal displacements of the beam do not influence the experimental results significantly, the only source of systematic uncertainty is the beam displacement on the vertical axis. The accuracy of the beam position was 3-4 mm what brings 15% systematic uncertainty in the experimental results of the top foils and iodine samples.

Foils and samples displacement

The calculation with the foils displaced to the left for 0.3 cm was performed. The production rates did not differ from the production rates for not displaced foils within the limits of statistical uncertainties (5%). The displacement of the foils upwards for 2 mm produces for ca 5% lower production rates in foils at the beginning of the target, the difference decreases to 0 around

3. PHASOTRON EXPERIMENT

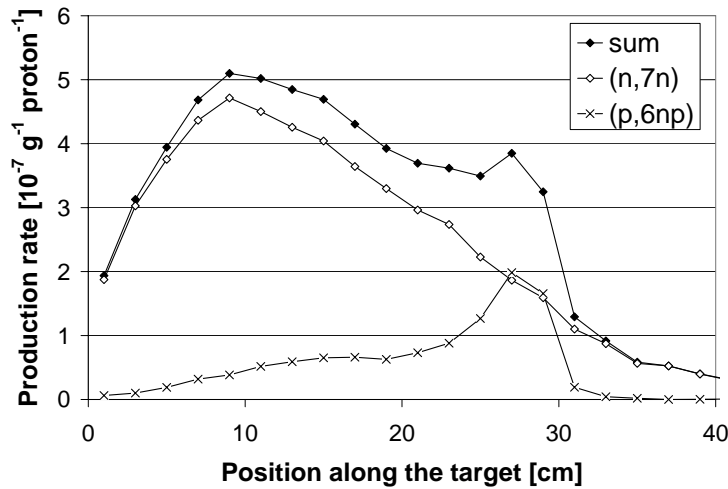


Figure 3.9: The production rates for $^{197}\text{Au}(n,7n)^{191}\text{Au}$ and $^{197}\text{Au}(p,6np)^{191}\text{Au}$ reactions (and their sum) along the target calculated with MCNPX. Around the 30th cm, the protons contribute 50% to the total production rate. Scale on Y axis is linear, so that the second peak is better seen. Statistical errors (ca. 15%) are not shown on the graph.

the 20th cm.

Another calculation with the foils displaced for 0.3 cm along the target showed that in the foils placed far from the 30th cm, the production rates are not sensible to such displacement. For the isotopes produced through (n,xn) and (p,(x-1)np) reactions with $x > 4$, there is another peak in production rates around the 30th cm, see Figure 3.9. It is caused by primary protons, which are deviated from their initial direction by coulomb interactions and reach the target surface around this point. They contribute up to 50% to the production of isotopes from higher (n,xn) reaction. The peak maximum moves to the neighbor foil if foils are displaced along the target for 0.3 cm. This is also observed if the target is simulated with extra 0.5 mm air gaps inserted between the segments. The production rates in the peak change for 50% when foils are displaced along the target or the target is extended with gaps between segments comparing with the normal setup.

Apart from the foils near the 30th cm, the foils are not sensible to small displacements along the target. The foils and target positions are known with the accuracy ca. 1 mm, the systematic uncertainty is below 5%.

Similar calculations were performed for iodine samples. The accuracy of placement of these samples was not so good and 0.5 cm displacement along the target or in the upward direction are possible. The systematic uncertainty of the experimental results in the iodine samples was calculated to be 30%.

Proton and pion induced reactions

Part of the radioactive material in the foils is produced by protons and pions (only in threshold reactions). The calculations showed that the production of radioisotopes in reactions with pions is at least three orders of magnitude lower than the production in reactions with neutrons and thus negligible. Protons influence mainly the production rates of (n,xn) reactions with higher x , and their influence is the biggest around the 30th cm of the target (the point of the rapid decrease of the neutron field). Around the 30th cm also the protons from the primary beam reach the surface of the target as was mentioned in the previous paragraphs. At that point the proton contribution to the total production rate was 10% for $(n,2n)$, 40% for $(n,6n)$, and 50% for $(n,9n)$ reaction, see Figure 3.9.

3.3 Simulations - comparison of code predictions with experimental results

3.3.1 Determination of beam parameters by simulations

The exact conclusions about the beam shape and position were not possible from the experimental data. Few MCNPX simulations (CEM03 cascade model) with different beams were performed to find the approximation of the beam, that would produce the production rates in the monitor foils and in the top foils close to the experimental ones.

The beam characteristics were measured with two independent sets of detectors: the wire chamber and the cross of the monitor activation foils in the gap between the two target sections.

The beam data from the cross of monitor foils suggested that the beam was displaced upwards, so that the center is somewhere between the central and the top foil, and that the beam FWHM is 0.7 and 0.8 cm in the X and Y direction (this corresponds to the beam diameters 1.6 and 1.9 cm from the wire chamber). Such a beam describes the production rates in the monitors well, but predicts 1.6 times higher values in the top foils (Fig. 3.10).

The data from the wire chamber show that the beam was centered to the target axis. The simulation with the centered beam (FWHM in the X and Y direction were 0.7 and 0.8 cm) predicts the values in the top foils well. It predicts well also the values in the cross of the monitor foils, assuming that the cross was displaced downwards for 0.5-1 cm.

The data from the wire chamber and from the cross of monitor foils do

3. PHASOTRON EXPERIMENT

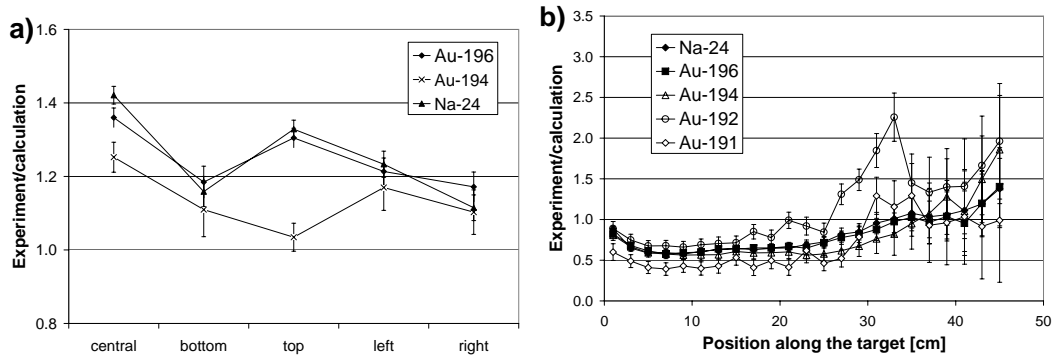


Figure 3.10: a) Ratios between experimental and simulated B-values in beam monitor foils placed in the gap. The beam in this simulation was approximated with the Gaussian profile with FWHM in the X and Y direction 0.7 and 0.8 cm and displaced for 1.1 cm upwards and 0.1 to the right. b) Ratios between experimental and simulated B-values in Au and Al foils placed along the target. INCL4/ABLA models were used to simulate B-values. The uncertainties are the sum of the statistical uncertainties of the simulation and the uncertainties of the gamma peak fit.

not agree. The determination of the beam position was based only on the wire chamber data, because the cross with the monitor foils was probably misplaced. The comparison of the simulated and experimental data from other foils show that the beam was centered. The beam position uncertainty was estimated to be ca. 3 mm. The simulations from the section 3.2.1 concerning the beam parameters showed that the systematic uncertainty of the experimental results on the top of the target is therefore 15%.

3.3.2 Simulations of neutron fluences in foils on top of setup

Simulations with CEM03 cascade model

The complete setup was then simulated with the beam parameters which were determined above. The calculations were successful in describing the spatial distributions and the absolute values of production rates along the target.

The distribution of low energy neutrons along the target which was calculated predicts an almost homogenous distribution (as the experiment), but experimental values for ^{198}Au are ca. 1.5-3 higher than calculated production rates, Figure 3.11. In the Section 3.2.1, it was explained that the distribution

3.3. Simulations - comparison of code predictions with experimental results

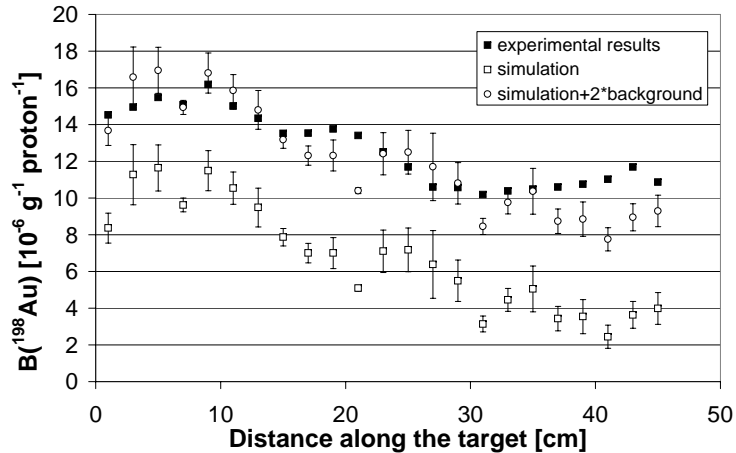


Figure 3.11: The experimental and simulated ^{198}Au production rates in the foils along the target. The background is approximated with a value near the end of the target. INCL4/ABLA models were used in the simulation. CEM03 cascade/evaporation model predicts similar, a bit lower values of ^{198}Au production rates.

of low energy neutrons responsible for the production of ^{198}Au is the sum of the spallation neutrons from the target and the homogenous field of neutrons reflected from the concrete walls. The structure details of concrete walls are not known accurately and the underestimated contribution from the walls gives rise to the disagreement between the experiment and simulation. In the Figure 3.11, the homogenous contribution from the walls was increased for the factor of three (the production rate near the end of the target was taken for the homogenous contribution value), and it can be seen that in this case the simulated values describe the experimental results quite well. The experiment was not focused to low energy neutrons, and as there is not enough information about the moderating setup parts, further discussion on this topic is not relevant.

The calculated production rates of threshold reactions (high energy neutrons) describe the experiment well: there is a maximum at around 8th cm, and near the 30th cm the values start to decrease faster. The absolute values are described well except for some isotopes (^{191}Au , ^{202}Bi), see Figure 3.12.

A sharp peak for some isotopes ($^{191-192}\text{Au}$, $^{202-205}\text{Bi}$) in experimental/calculation ratios around the 30st cm is also visible in the graph. This is the point, where the protons exit the target material and produce radioactive isotopes in the foils and the peak can be explained with the systematic uncertainties of the experimental data (see Section 3.2.1). The results around this point are very sensitive to two parameters of the setup that could not

3. PHASOTRON EXPERIMENT

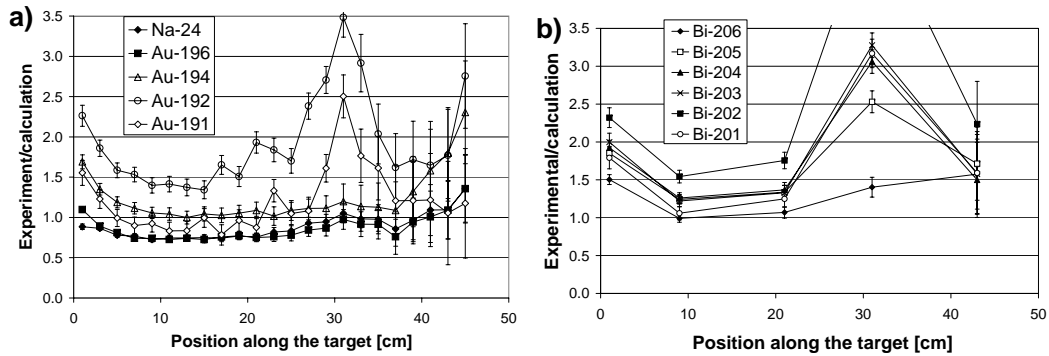


Figure 3.12: Ratios between experimental and simulated B-values in Au, Al (a), and Bi (b) foils placed along the target. CEM03 cascade/evaporation was used to simulate B-values. The uncertainties are the sum of the statistical uncertainties of the simulation and the uncertainties of the gamma peak fit.

be controlled enough precisely: the displacement of the foils along the target (uncertainty 1-2 mm) and small gaps between the target segments (1 mm). The additional simulation with extra 1 mm gaps between the target segments showed that the peak is reduced while the other ratios stay unchanged.

Simulations with INCL4/ABLA cascade model and FLUKA code

Simulations were repeated using the INCL4/ABLA model from MCNPX code package. The comparisons between the experimental and calculated values in the beam monitors and foils on top of the setup are shown in Figure 3.13. INCL4/ABLA predicts similar results as CEM03, with some ratios closer to 1 and with a bit decreased peak around the 30th cm. It should be noted that both simulations predict similar ratios for isotopes ¹⁹⁶Au and ²⁴Na, but disagree in the ratios of isotopes with higher thresholds (^{191–192}Au, Bi).

Using the same setup approximations as for the MCNPX simulations (see 3.2), the neutron and proton fluences were calculated with the FLUKA 2006.3b code. The numbers of neutrons/protons were convoluted with the same cross-sections as for MCNPX simulations.

In the Figure 3.14 it is seen that the ratios for different isotopes in FLUKA calculation are closer to 1 than in MCNPX calculations and also that the peak around the 30th cm is reduced. Only in the foils at the beginning of the target, experimental values are significantly higher than FLUKA prediction.

3.3. Simulations - comparison of code predictions with experimental results

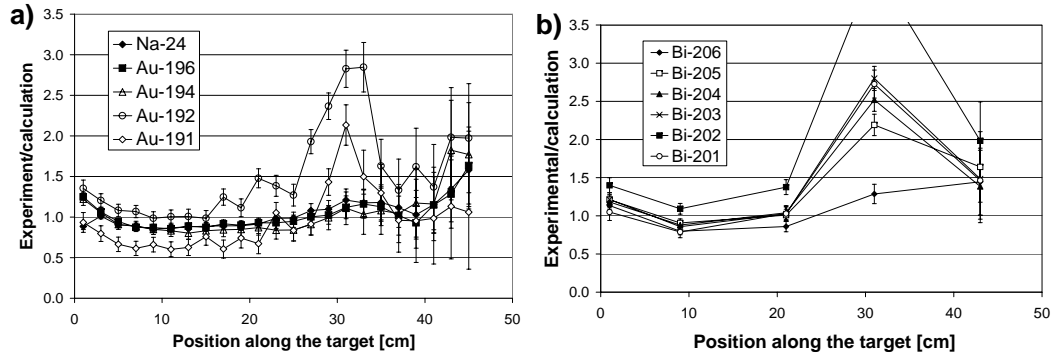


Figure 3.13: Ratios between experimental and simulated B-values in Au and Al foils (a), and in Bi foils (b). INCL4/ABLA models were used to simulate B-values. The uncertainties are the sum of the statistical uncertainties of the simulation and the uncertainties of the gamma peak fit.

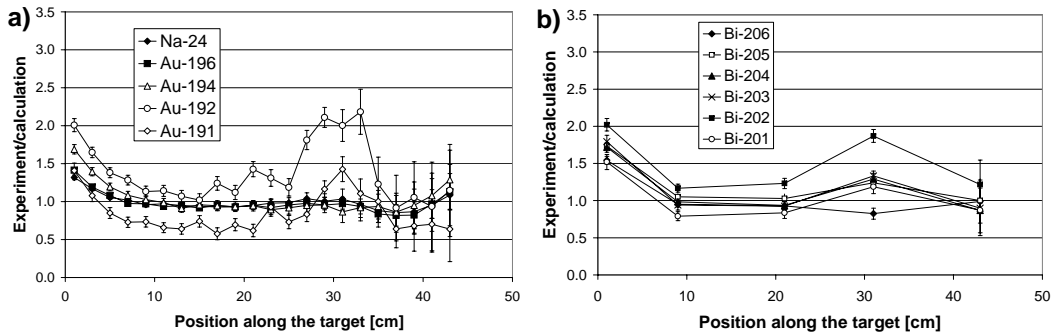


Figure 3.14: Ratios between experimental and simulated B-values in Au and Al foils (a), and in Bi foils (b). FLUKA 2006.3b code was used to simulate B-values. The uncertainties are the sum of the statistical uncertainties of the simulation and the uncertainties of the gamma peak fit.

Comparison between codes/models

The neutron and proton spectra in the foils on top of the setup were calculated with MCNPX models CEM03 and INCL4/ABLA and with the FLUKA code and were compared with each other. In the Figure 3.15 are compared the neutron spectra in the foil at the 9th cm. The biggest disagreement between spectra is in the energy region below 3 MeV and above 30 MeV and is up to 50%. This disagreement is observed in different predictions of high threshold production rates by different codes (e.g. ¹⁹¹Au in Figures 3.12, 3.13, 3.14). The neutrons with energies above 30 MeV present less than 10% of all produced neutrons. Concerning the total number of produced neutrons per one incident proton, the codes are in good agreement. The FLUKA code and MCNPX INCL4/ABLA predict values 11.8 and 11.7 produced neutrons per one primary proton and MCNPX CEM03 predicts slightly higher value 12.6 produced neutrons per one primary proton. These predictions are the same within 10%.

3.3.3 Simulations of neutron fluences in iodine samples

The neutron and proton fluences in iodine samples were calculated with the MCNPX code package using the INCL4/ABLA models. The fluences were convoluted with cross sections which were also calculated with TALYS/MCNPX. In the Figure 3.16 are shown the ratios between the experimental and simulated production rates in iodine samples. In a rude approximation, one can see that MCNPX overpredicts the production rates. It must also be noted that the systematical uncertainties of the experimental data in the samples was close to 50% because of the samples and beam position uncertainty. The simulations with other models and with the FLUKA code predict similar results.

3.3. Simulations - comparison of code predictions with experimental results

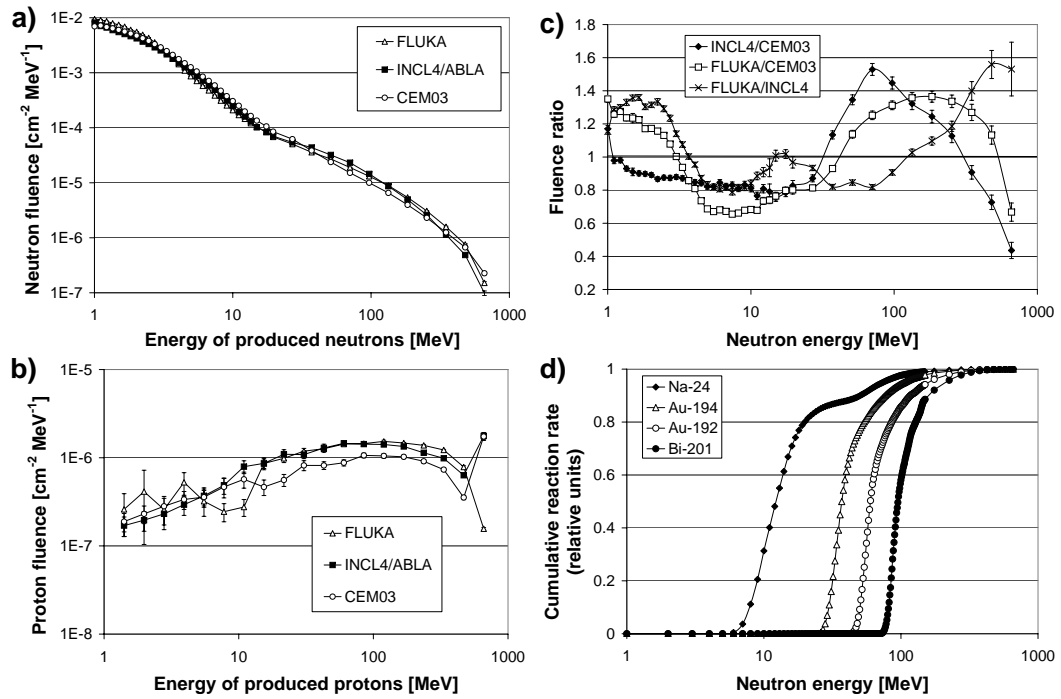


Figure 3.15: The neutron (a) and proton (b) spectra in the foil on the 9th cm calculated with the MCNPX CEM03, MCNPX INCL4/ABLA and the FLUKA code, and the ratios between the calculated neutron spectra (c). In (d) are the cumulative production rates (in relative units, normalized to 1) calculated with MCNPX CEM03. It can be seen that ^{24}Na , ^{194}Au , ^{192}Au and ^{201}Bi are produced mainly with 10, 30, 60 and 90 MeV neutrons, respectively. The uncertainties are the sum of the statistical uncertainties of the simulation and the uncertainties of the gamma peak fit.

3. PHASOTRON EXPERIMENT

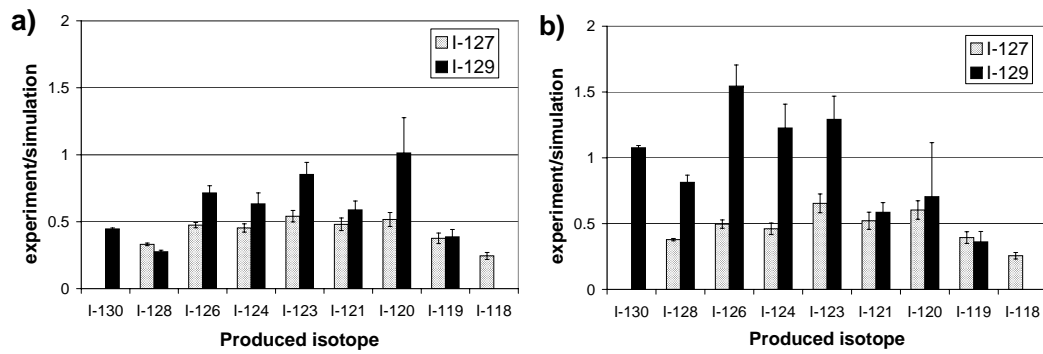


Figure 3.16: Ratios between experimental and simulated B-values for different isotopes in ^{127}I and ^{129}I . Samples were placed at 9th (a) and 21st cm (b). INCL4/ABLA was used to simulate B-values. The uncertainties are the sum of the statistical uncertainties of the simulation and the uncertainties of the gamma peak fit.

Chapter 4

Energy Plus Transmutation

The setup Energy Plus Transmutation (EPT) imitates one of the possible configurations of the ADS core. Apart from the lead target, it includes the subcritical blanket ($k_{eff} \approx 0.2$) made from natural uranium and is surrounded by neutron moderator. Spallation and other processes (neutron moderation and transport, fission in uranium) produce a complex neutron spectrum. The setup is very useful to test the general properties of an irradiated ADS subcritical core and as well provides data for the benchmark tests of Monte Carlo codes.

Within the international collaboration that performs experiments with the EPT setup, our group takes care of the measurements with the activation detectors and is providing the main part of the computer simulations. I took part in planning and realization of three experiments with this setup (0.7 GeV protons, 1.6 and 2.52 GeV deuterons). The analysis of the experimental data from these experiments was performed by O. Svoboda, earlier experiments with protons were mainly analyzed by A. Krása.

At these experiments I got well acquainted with the complex EPT setup so that I could implement it in the MCNPX code. In this work, I am using the MCNPX code to explain the functioning of the setup and to study the uncertainties of the obtained experimental data. I have simulated all EPT experiments and have compared the experimental values obtained with activation detectors, solid state nuclear track detectors and transmutation samples to simulations (the experimental results were provided by other members of our collaboration). These comparisons were mainly focused to the valuation of different spallation models implemented in the MCNPX and in FLUKA codes (the setup was implemented in the FLUKA code by our colleague Andrei Potapenko). The example of the comparison of experimental and simulated results for the experiment with 1 GeV protons is given at the end of this chapter.

4.1 Experimental setup

The target-blanket part of the EPT setup is composed of four identical sections [19, 71]. Each section contains a cylindrical lead target (diameter 8.4 cm, length 11.4 cm) and 30 natural uranium rods (diameter 3.6 cm, length 10.4 cm, weight 1.72 kg) distributed in a hexagonal lattice around the lead target. The lead target and uranium rods are enclosed in aluminum claddings of thicknesses 2 mm and 1 mm, respectively. The target and uranium rods in each section are secured in hexagonal steel container with a wall thickness of 4 mm. The front and back of each section are covered with a hexagonal aluminum plate of thickness 5 mm. The four target blanket sections are mounted along the target axis, on a wooden plate (thickness 6.8 cm) covered with 0.4 cm thick steel sheet. There are 0.8 cm gaps between the blanket sections which are used for placement of foils. The four target blanket sections mounted on the wooden plate are placed in a wooden container filled with granulated polyethylene, density of which was measured to be 0.8 g cm^{-3} . The inner walls of the polyethylene box are covered with 1 mm thick cadmium layer. The floor wall of the polyethylene box is a textolite plate of thickness 3.8 cm. The polyethylene box and cadmium are used as the biological shielding and they modify the neutron spectrum as will be discussed. The geometrical arrangements and dimensions of the EPT setup are shown in the Figure 4.1.

Several experiments have been carried out using the EPT setup and its target was irradiated with relativistic protons and deuterons of energies in the range of 0.7 to 2.52 GeV. In these experiments the neutron flux was measured using activation foils that were placed between the blanket sections. The foils were of the square with dimensions of $2 \text{ cm} \times 2 \text{ cm}$ and the thickness of ca. 0.1 mm, made of aluminum, gold, bismuth, yttrium, and other monoisotopic materials. Various nuclear reactions, e.g. (n,γ) , (n,xn) , (n,α) , occur in the foils during the irradiation.

For thermal, epithermal, and resonance neutrons, the dominant reaction is the neutron capture (n,γ) process for which cross-sections are large (in the range of hundreds to thousands of barns). The others are threshold reactions for which cross-section are in range of mbarns to barns. At the end of the irradiation, the activities of foils were measured by the HPGe detectors and the spectra were analyzed in the same way as for the Phasotron experiment (the analysis procedure is explained in detail in Part 2). The production rate $B(A)$ - the number of the produced radioisotope A per one incident proton and per 1 g of the foil material - is again used to present the results.

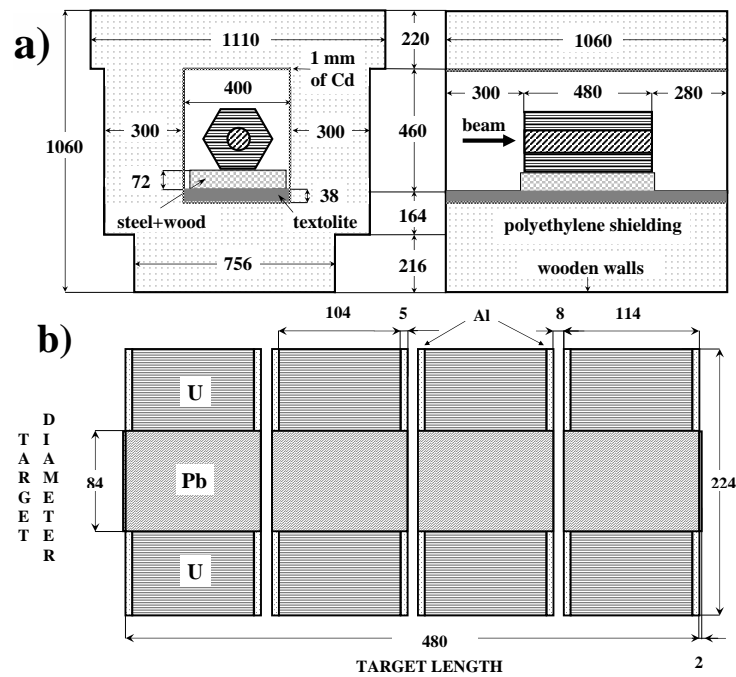


Figure 4.1: The layout of the EPT setup: a) the front cross-section and the side cross-section, b) the side cross-section of the target-blanket assembly only.

4.2 Simulation procedure

MCNPX and FLUKA Monte Carlo codes were used to simulate the behavior of neutrons and other secondary particles in the experimental setup. The simulation procedure is in more detail described in the previous part (Phasotron experiment, Section 3.2). To obtain the $B(A)$ values at different places of the setup, the simulated spectra of neutrons, protons and pions (CEM03 model was used in simulations) were folded with the cross-section for the specific reaction (TALYS+MCNPX CEM03, MCNPX libraries for n,γ). The EPT setup was defined in the codes with the characteristics given in the Figure 4.1. The Figure 4.2 illustrates the setup as seen by the MCNPX code.

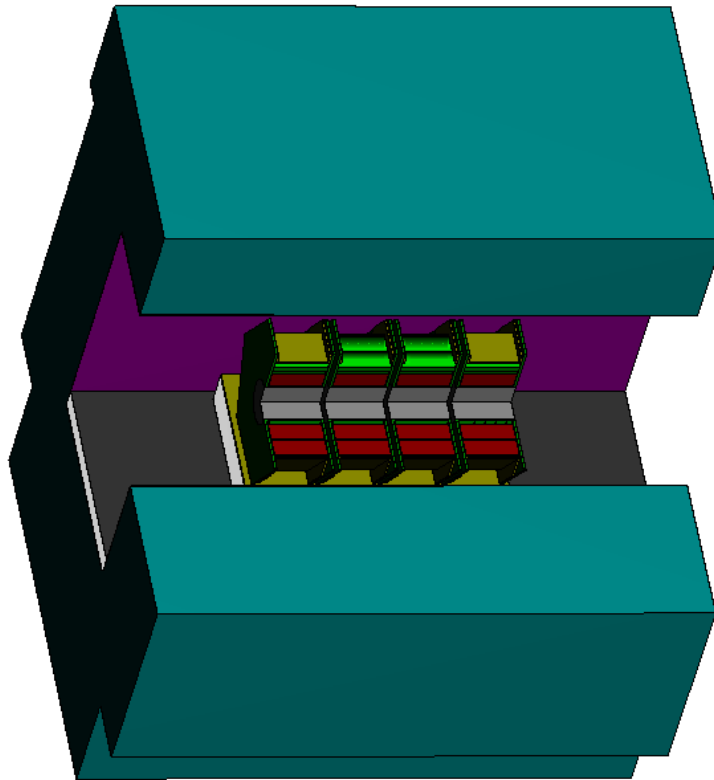


Figure 4.2: Plot of the target placed in the polyethylene box (SABRINA plot of the MCNPX input file, provided by Jaroslav Šolc).

In order to investigate the role of different parts of the experimental setup on the obtained results, MCNPX simulations with changed geometrical and physical properties of the setup were performed. The simulations were performed for the proton beam with the energy 1.5 GeV. To demonstrate the

behavior of activation foils in the setup, two reactions were simulated. The reaction $^{197}\text{Au}(n,\gamma)^{198}\text{Au}$ is sensitive to the low energy neutrons ($E_n < 0.1$ MeV) while the $^{197}\text{Au}(n,2n)^{196}\text{Au}$ reaction has a threshold energy of 8 MeV and therefore shows the behavior of the high energy neutrons ($E_n > 8$ MeV) in the EPT setup.

The simulations where the influence of the intranuclear cascade model and the cross-section libraries were studied were also performed. MCNPX was also used to simulate the criticality of the experimental setup, as well as the number of produced neutrons per one incident proton. At the end, the experimental results from the experiment with 1 GeV protons are compared to MCNPX and FLUKA simulations.

4.3 Influence of setup parts and experimental conditions

4.3.1 Polyethylene box and cadmium layer

The polyethylene box around the target-blanket assembly moderates the neutrons and reflects part of them back inside the box. The 1 mm thick cadmium sheet that covers the inner walls of the polyethylene box absorbs the reflected thermal neutrons (neutrons with the energy below the cadmium cutoff ≈ 0.5 eV). A set of simulations (without box, with box but no cadmium, and with both - box and cadmium) showed that only reflected neutrons with energies below the cadmium cutoff energy are stopped by the cadmium layer (Figure 4.3a). The box and cadmium do not affect the high energy ($E_n > 10$ MeV) part of the neutron spectrum (Figure 4.3b). From the Figure 4.3 it is evident that the low energy part of the neutron spectrum in the blanket area is produced by the combined effects of the polyethylene and cadmium around the target blanket system. The spectra shown in the Figure 4.3 were simulated on top of the second section of the target-blanket assembly.

The primary function of the polyethylene box was to reduce the emission of the high energy spallation neutrons to the environment. In simulations, the neutrons emitted to the environment were counted to study the functioning of the box as a shielding. The Figure 4.4 shows simulated neutron spectra emitted to the environment for the target-blanket assembly alone and for the target-blanket assembly placed in the polyethylene box. Two more simulations were performed, one with the front and the back added to the box (20 cm of polyethylene + 1 mm of cadmium), another with the outer walls of the box covered with 1 mm cadmium layer.

The polyethylene box essentially decreases the flux of the emitted high

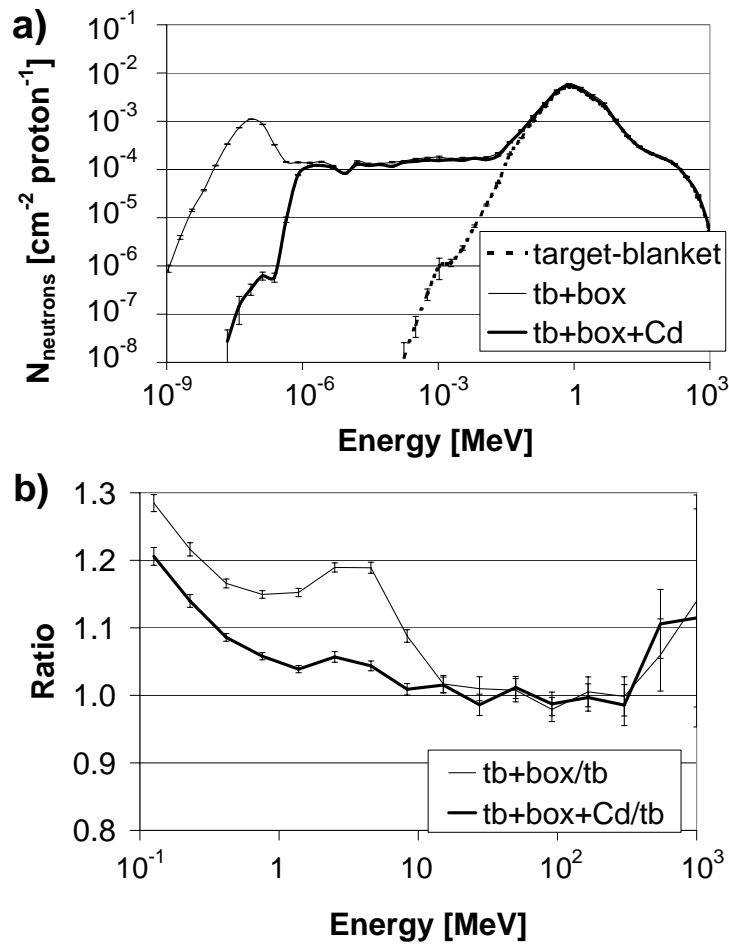


Figure 4.3: a) The simulated neutron spectra on top of the second section of the target-blanket assembly are shown for three cases: for the target-blanket assembly without the polyethylene box, for the target-blanket assembly with the box but no cadmium, and for the target-blanket assembly with both, the box and the cadmium. Small thermal peak in the case of tb+box+Cd is caused by the moderation effect of the wood.

b) The ratios of the spectra from the left figure from the energy 0.1 MeV. From these ratios it can be concluded that the polyethylene box affects significantly only neutrons with energies lower than 10 MeV. The increase of the ratios 1-10 MeV range is caused by the fission of ^{235}U with moderated neutrons.

energy neutrons by moderating them to lower energies. Simulations suggest that from ca. 50 neutrons that are produced per one proton at 1.5 GeV, 42 would escape to the environment in the hypothetical case without the shielding, but with the shielding only 10 neutrons escape, 8 from these through front and back openings in the polyethylene box. By adding the front and the back wall to the box, the number of neutrons emitted to the environment decreases to 2 neutrons per primary proton. The cadmium layer on the outer side of the box does not change these number significantly. The other parameters of the setup (k_{eff} , number of produced neutrons, Section 4.6) are not influenced by the modifications of the polyethylene box.

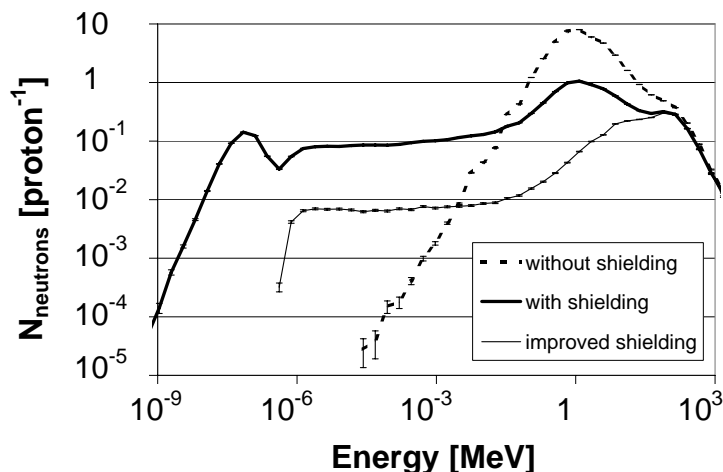


Figure 4.4: Simulated neutron spectra emitted to the environment from the target-blanket assembly only, the target-blanket assembly surrounded by the polyethylene box, and the target-blanket assembly surrounded with the improved polyethylene box with added front wall, back wall, and outer cadmium layer.

4.3.2 Other setup parts (metal parts, wood)

Experimental data have shown that at the bottom part of the target-blanket assembly there are more low energy neutrons than at its upper part [72]. To verify if this is due to the wooden and textolite plates under the target-blanket assembly, the following three simulations were performed:

1. both wooden plate and polyethylene box were present,
2. only wooden plate was present,

4. ENERGY PLUS TRANSMUTATION

3. only polyethylene box was present.

Fourteen ^{197}Au foils were placed in the first gap along the vertical axis Y in the interval of -14 to 14 and ^{196}Au , ^{198}Au production rate in each foil was determined. The wooden and textolite plates were approximated with the wood from the MCNPX materials library [73] and atomic fractions of 51%, 23%, and 26% were used for H, C and O respectively. The same density of 0.5 kg/l was used for the wood and textolite. The simulation results are shown in the Figure 4.5. In the case of the high energy neutrons, no asymmetry beyond the 5% was observed between the ^{196}Au production rates in the Au foils in +Y direction as compared to their corresponding foils in the -Y direction. However, in the case of the low energy neutrons the ^{198}Au production rate is dramatically affected by the presence of the wooden and textolite plates. The polyethylene box alone (in the absence of the wooden and textolite plates) produces almost homogenous, low energy neutron field in the first gap. This is expected due to the geometrical and material symmetry of the EPT setup in absence of wooden and textolite plates.

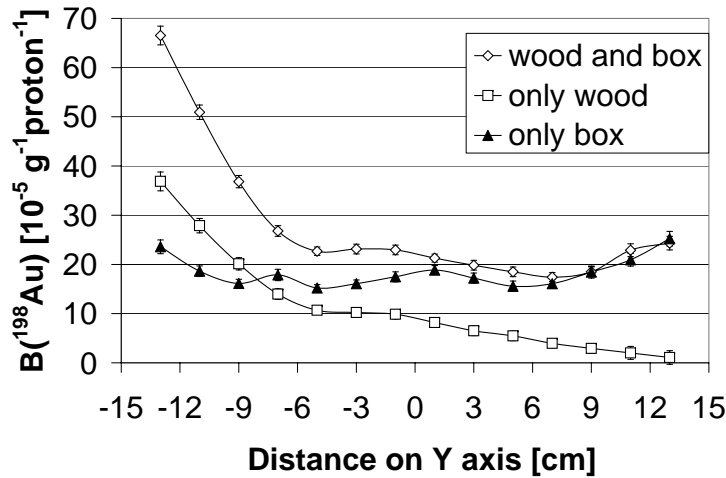


Figure 4.5: The $^{197}\text{Au}(n,\gamma)^{198}\text{Au}$ production rates in foils placed along the vertical axis, Y in the first gap. The MCNPX simulations were performed for three different material compositions of the EPT setup as shown in the figure inset.

The metallic materials (steel and aluminum) used in the target blanket sections (as described in Sec. 4.1) do not have significant effect on the neutron spectrum within the blanket. In general, the effects of these parts on the production rates in the activation foils do not exceed the statistical uncertainties of the simulations which were about 3%.

4.3.3 Activation foils

The foils that were used in the experiments had small dimensions and no significant neutron flux absorption in them is expected. However, some extreme cases where the foils could influence the experimental results were studied.

The activation foils in one gap have negligible influence on foils in other gaps or on the foils outside of the target-blanket assembly. This was proved by placing gold foils with thicknesses 2 and 4 mm in the first gap (extended over the whole gap) and simulating the production rates in the foils in the third gap. No significant effects on the production rates outside of the 3% statistical uncertainties were observed.

A gold strap of 2 cm wide and 0.1 mm thick, stretching over the whole gap was placed in front of the foils in the first gap. Subsequent simulations showed that the rate of the $^{197}\text{Au}(n,\gamma)^{198}\text{Au}$ reaction in the foils behind gold strap was reduced by up to 15%, while the rate of the $^{197}\text{Au}(n,2n)^{196}\text{Au}$ reaction did not change within the statistical uncertainties (3%). The strap should not have any significant effect on the high energy part of the neutron spectrum, as neutrons at that energy have small cross-sections for the reactions with the gold. Only the influence of the low energy neutrons with large cross-section resonances with the gold is expected.

Simulations also showed that when gold foils were covered on both sides with bismuth foils of thickness 1 mm the production rates of the threshold reactions do not change beyond the simulation uncertainties. On the other hand, absorption in gold has significant effect on reactions with low energy neutrons, i.e., ^{198}Au production rates in 50 μm thick gold foils are 50% lower due to absorption. The absorption for threshold reactions is negligible. This suggests that the threshold foils can be mounted one after another within the gaps.

In the earlier experiments with the EPT setup, the activation foils were mounted on a thick, plastic plate, and then placed in the gaps between the blanket sections. Such an arrangement may affect the low energy section of the neutron spectrum in the gaps. MCNPX simulations of the neutron spectrum in the gap in which a polyethylene plate of thickness 2 or 6 mm is inserted showed that such a plate has no effect on the high energy neutrons ($E_n > 10$ MeV), but, changes the low energy part of the spectrum, see the Figure 4.6.

Another source of the systematic experimental error is the displacement of the foils. By simulations it was estimated that a displacement of foils for 0.5 cm results in production rates that are ca. 20% different from the production rates with not displaced foils.

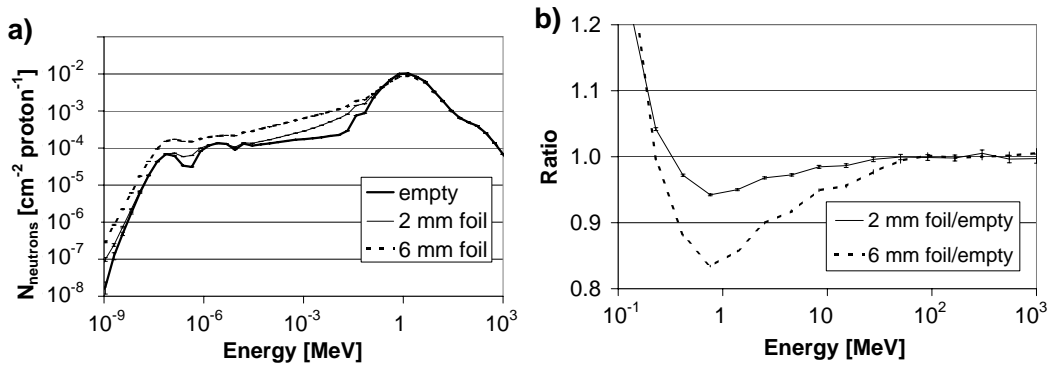


Figure 4.6: a) The neutron spectra inside the first gap when a 2 mm or a 6 mm thick polyethylene foil is inserted in it and with the empty gap (MCNPX simulation).

b) The ratio of the high energy regions of the spectra from the left figure. It is seen that the polyethylene influences significantly only neutrons with energies lower than 10 MeV.

4.3.4 Beam parameters

The beam parameters in our experiments were experimentally determined with a known uncertainty. The beam displacement is known with an accuracy of 3 mm. Its profile is described with the Gaussian function with the extending tails. To estimate the systematic uncertainty resulting from the beam displacement and the profile approximation, a set of MCNPX simulations was performed and the production rates in the control foils were computed.

Five positions in the setup were chosen for the control foils so that the results from these foils could be applied to all used activation foils. Foils 1 and 2 were placed in the first gap between the target blanket sections, at the radial distances of 3 and 11 cm from the target axis. The foils 3 and 4 were at the same radial positions as the foils 1 and 2, but in the third gap. The foil 5 was in the horizontal position on the top of the second blanket section.

To avoid the influence of the neutrons reflected from the polyethylene box around the target-blanket assembly, simulations were performed without the polyethylene box. Three simulations were made with two circular and homogenous beams of diameters 3 mm and 3 cm and with a beam of Gaussian profile for which the FWHM in both X and Y directions were 3 cm. In all three cases the beam directions were parallel to the target axis and the beams and target centers coincided. The induced production rates in the control foils for these three proton beam profiles were the same within the

statistical uncertainties of the simulations (i.e., 5%). This suggests that in our experimental setup the beam profile is not of a great importance as long as it is symmetric. The tails of the beam are for approximately three orders of magnitude less intensive than the beam central part and have negligible influence on the activation foils (but that does not apply to other types of detectors, eg. solid state nuclear track detectors with lead irradiator).

In a series of simulations without the polyethylene box, the center of the Gaussian proton beam as described above, was displaced by 3, 5, 8, and 10 mm from the target axis and along the positive direction of the Y axis. The production rates in the control foils showed a strong dependency on the beam displacement. The displacement of the beam 5 mm changes $^{197}\text{Au}(n,2n)^{196}\text{Au}$ and $^{197}\text{Au}(n,\gamma)^{198}\text{Au}$ production rates by up to 20% and 30% respectively.

With the presence of the polyethylene box (i.e., the case of the actual experiments) and as a result the contribution of the reflected low energy neutrons, the difference in the $^{197}\text{Au}(n,\gamma)^{198}\text{Au}$ reactions rates for the cases of centered and displaced beam decreases to about 10% as compared with about 30% when the box was absent. The polyethylene box has no effect on high energy induced production rates (i.e., $^{197}\text{Au}(n,2n)^{196}\text{Au}$). A beam center displacement of 3 mm results in a systematic error of up to 15%. The Figure 4.7a shows the difference between the production rates for centered and displaced proton beams (see the figure caption for details).

Another simulation was performed with the beam which was not parallel to the target axis. The beam and the target centers coincided, but the direction of the beam was deflected from the target axis for 3° upwards, exiting the target 2.5 cm from its center. Simulation showed that the deflection of the beam causes the increase of the production rates for up to 60% and 40% in reactions $^{197}\text{Au}(n,2n)^{196}\text{Au}$ and $^{197}\text{Au}(n,6n)^{192}\text{Au}$ respectively (the Figure 4.7b).

These simulations showed that the beam parameters have significant impact on the activation foil results. Because of the experimental uncertainties in the beam position and profile, the systematic uncertainty of the results obtained with the activation foils is between 20-30%.

4.4 Isotope production in reactions with protons, pions and photons

Radioactive isotopes in the foils can also be produced by other particles, mainly by protons, pions, and photons. To estimate the contributions of these particles to the production rates in activation foils, the corresponding

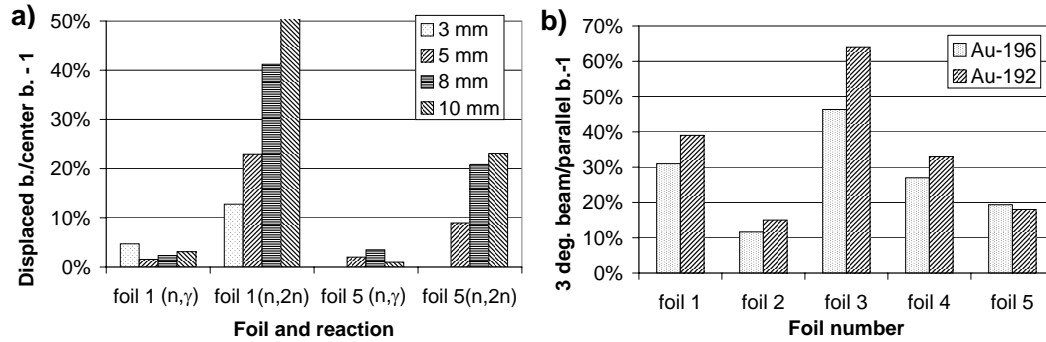


Figure 4.7: a) The difference between the production rates in control foils for centered and displaced proton beams. The proton beam was displaced along the positive Y-axis with the amount given in the figure inset, and simulations were performed when the polyethylene box was present. The abbreviation (n,2n) and (n,γ) refer to $^{197}\text{Au}(n,2n)^{196}\text{Au}$ and $^{197}\text{Au}(n,\gamma)^{198}\text{Au}$ reaction respectively.

b) The difference between the production rates for the beam parallel to the target axis and for the beam entering at 3 degrees. The abbreviation Au-196 and Au-192 refer to $^{197}\text{Au}(n,2n)^{196}\text{Au}$ and $^{197}\text{Au}(n,6n)^{192}\text{Au}$ reaction respectively.

reaction cross-sections were evaluated using the MCNPX. The neutron, proton, pion and photon spectra in the foils were simulated and folded with the evaluated cross-sections. It was found that up to 20% of reaction products could be produced by proton induced reactions, suggesting that the influence of protons cannot be neglected. Most of this contributions are proton induced reaction with protons from the primary beam. The contribution of radioisotopes produced by protons decreases very quickly with increasing radial distance and is strongly dependent on the proton beam profile and position of the beam center on the target. The same applies to deuterons in case of deuteron beam. The isotope production by pions and photons is suppressed for at least two orders of magnitude.

4.5 Parameters of simulations: Effects of different physics models and cross-section libraries

The setup was simulated with different combinations of intranuclear cascade (CEM03, BERTINI, ISABEL, INCL4) and evaporation models (DRESNER,

ABLA) included in MCNPX, in order to check if these models predict similar production rates.

In the case of $^{197}\text{Au}(n,2n)^{196}\text{Au}$ reaction, different INC models predict production rates similar within 10% when using the same evaporation model. These production rates differ for 40% from the production rates simulated with another evaporation model. The situation for the reaction $^{197}\text{Au}(n,6n)^{192}\text{Au}$ with higher threshold ($E_{thr}=39$ MeV) is inverse, only the use of different INC model changes the results significantly, while the results are not changed if another evaporation model is used.

Separate simulations with NRG-2003 and with LA150 libraries confirmed that the production rates are very weakly dependent on the choice of the cross-section libraries, the simulated production rates were the same within the statistical accuracy.

4.6 Global characteristics of EPT

Two important parameters of the EPT setup were determined with MCNPX simulations: the criticality (k_{eff}), and the number of produced neutrons per one incident proton. Using KCODE, the criticality of the EPT setup was simulated to be $k_{eff}=0.20263$. The number of decimals corresponds to the obtained statistical accuracy, however, the systematic uncertainty of the result is much bigger (\approx few percents due to not well known setup parameters). At the energy $E_p=1.5$ GeV, the overall neutron production per incident proton m , is 50 which includes neutrons from spallation process, uranium fission, and (n,xn) reactions. But in the Figure 4.8 the ratio of m/E_p is shown as a function of incident proton energy (E_p). As it can be seen the optimal energy for the neutron production in the EPT setup is around 1 GeV.

The modifications of the polyethylene box discussed in 4.3.1 have small influence on the number of produced neutrons. Compared with the bare target-blanket assembly, the number of produced neutrons increases for 2% when the box is included in simulation. This number increases for additional 4% if the cadmium layer is removed from the inner side of the box.

The factor k_{eff} is slightly more sensible to polyethylene box modifications. The k_{eff} for the bare target-blanket assembly is 0.19375, with the polyethylene box it is 0.20263 (0.20288 for the box with the front and back wall), and if the cadmium layer is removed from the inner side of the box $k_{eff}=0.26156$ (0.28606 for the box with the front and back wall). Another interesting case is the target-blanket assembly sunk into water with the $k_{eff}=0.38432$.

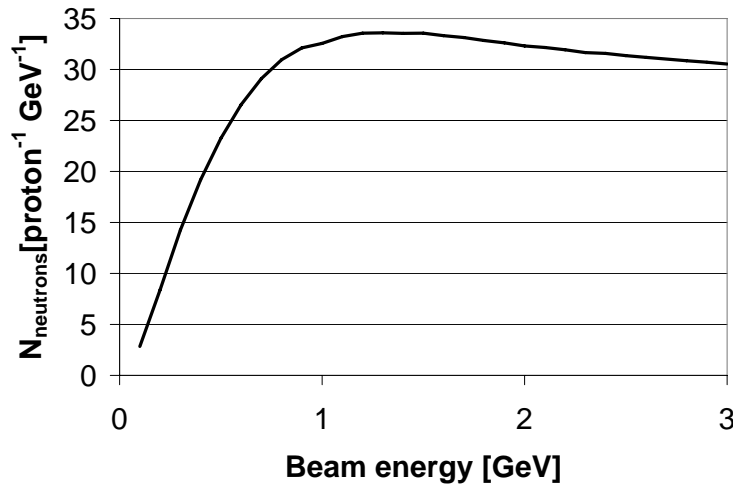


Figure 4.8: Dependency of the number of produced neutrons in the whole setup on the energy of the protons, normalized to one proton and to one GeV (MCNPX simulation).

4.7 Comparison of experimental data and simulation results

Mostly all experimental results obtained with the EPT setup by our group are published in the JINR preprints [71, 74, 75]. Detailed analysis of experimental results from proton experiments are in [76], which contains also the comparison of experimental results for different beam energies.

MCNPX and FLUKA describe most experiments successfully with the maximum disagreements between experiment and simulation around 50%. This is well seen in the case of the experiment with 1 GeV proton beam which is shown below as an example.

The Figure 4.9 shows the spatial distribution of some threshold production rates (the $B(A)$ values) in the gold activation foils at the incident proton energy of 1 GeV (the experimental data were analyzed by Antonin Krasa and are published in [74]). The gold foils were placed within the first gap at radial distances 3, 6, 8.5 and 10.7 cm, and in other gaps, as well as in front of and behind the target at the radial distance 6 cm. The threshold energy for (n, xn) reactions, ($x=2$ to 7) are in the range of 8 MeV to 40 MeV. The production rates rapidly decrease with the increasing distance from the target axis. The decrease in longitudinal direction is slower, with the maximum of the production rates in the first gap (12 cm after the beginning of the target).

4.7. Comparison of experimental data and simulation results

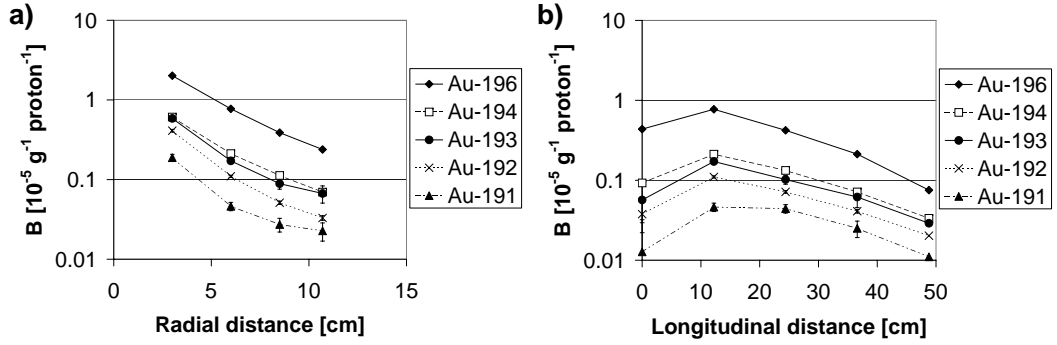


Figure 4.9: The radial (a) and longitudinal (b) distributions of the experimental production rates $B(A)$ in gold foils. The lines are drawn to guide the eyes. The statistical uncertainties of the points are not visible on this scale. The values are from the experiment with 1 GeV proton beam and are printed in the Appendix, Table 5.

The production rates were simulated with MCNPX and FLUKA codes. The INCL4/ABLA and CEM03 models and LA150 cross-section libraries were used in the MCNPX code. In the FLUKA code, the preequilibrium-cascade model PEANUT and cross-section libraries imported from ENDF/B-VI were used.

Comparison of experimental and simulated values shows similar trends that were observed in the case of the Phasotron experiment. The production rate predictions by the FLUKA code (Figure 4.12) and the INCL4/ABLA models from MCNPX code package (Figure 4.10) are very similar, and close to experimental production rates. The production rates for ^{191}Au are over-predicted by both codes. The CEM03 predictions (Figure 4.11) are more spreaded around the experimental values. Similar trends are observed also for other EPT experiments.

4. ENERGY PLUS TRANSMUTATION

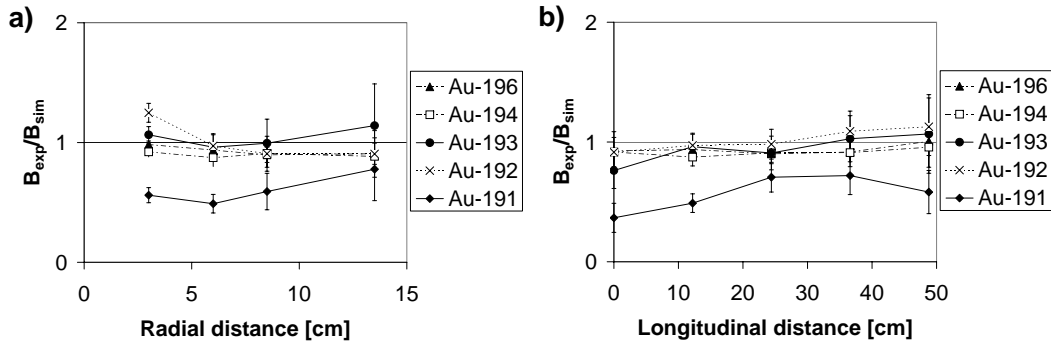


Figure 4.10: The ratios between the experimental values (gold foils) and simulated $B(A)$ in the radial (a) and in the longitudinal (b) directions from 1 GeV proton experiment. The INCL4/ABLA models from the MCNPX code package were used in the simulation.

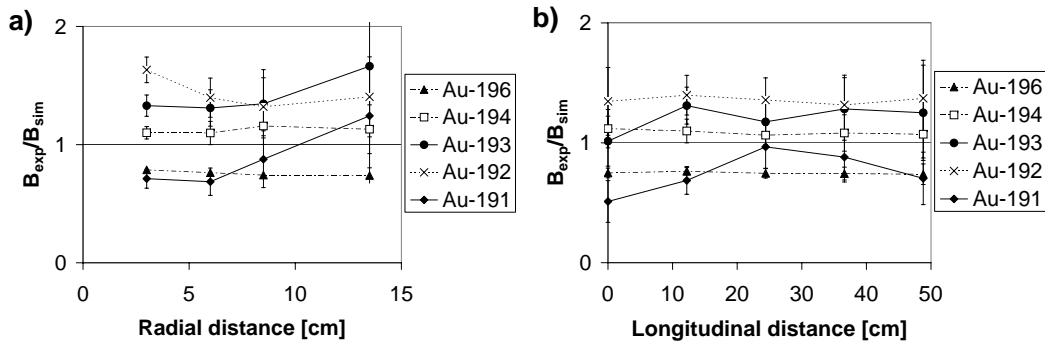


Figure 4.11: The ratios between the experimental values (gold foils) and simulated $B(A)$ in the radial (a) and in the longitudinal (b) directions from 1 GeV proton experiment. The CEM03 model from the MCNPX code package was used in the simulation.

4.7. Comparison of experimental data and simulation results

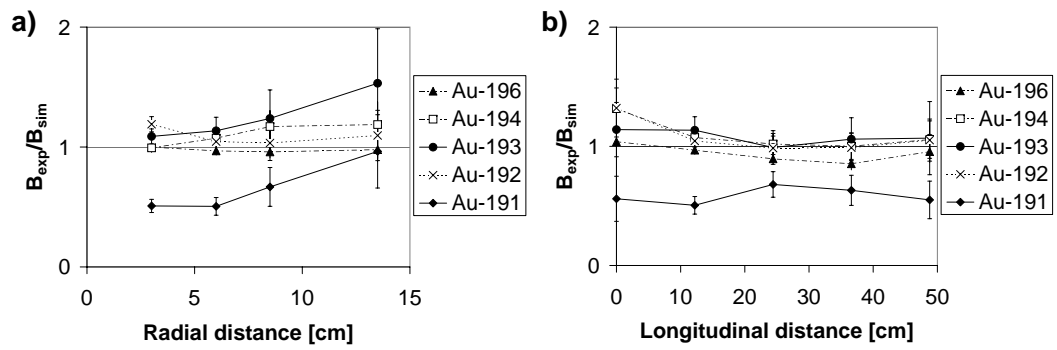


Figure 4.12: The ratios between the experimental values (gold foils) and simulated $B(A)$ in the radial (a) and in the longitudinal (b) directions from 1 GeV proton experiment. The FLUKA code was used in the simulation.

Chapter 5

Summary

In the frame of the Accelerator Driven System (ADS) research, series of experiments with simplified ADS setups were performed in the Joint Institute for Nuclear Research, Dubna. The distributions of created neutron fields were measured with different types of detectors. The experimental data are useful as the benchmark tests for different spallation codes, like MCNPX and FLUKA.

Two experimental setups are presented in more detail: a bare, lead target, which was irradiated with 660 MeV protons (Phasotron experiment), and a lead target surrounded with the uranium blanket, irradiated several times with protons and deuterons (Energy Plus Transmutation setup). The experimental data used in this work were determined with the nuclear activation detectors in the form of small foils of monoisotopic materials (≈ 1 g of material) that were irradiated by neutrons and later measured with the HPGe detectors.

The detailed studies of the systematical uncertainties of experimental data did not exist at the beginning of writing this thesis. Therefore, I implemented the experimental setups in Monte Carlo codes MCNPX and FLUKA (the Energy Plus Transmutation setup was implemented in FLUKA by A. Potapenko) and used the method of changing the simulation parameters to estimate the systematical uncertainties of obtained experimental data.

5.1 Simulations for gamma spectroscopy

The neutron activation detectors are widely used at the spallation experiments. They cover a wide energy scale from tens of MeV down to thermal energies. For their small size they can be applied almost everywhere, and the analysis of the experimental data is relatively easy. Their disadvantages

are the limited accuracy of the obtained results and several corrections that need to be taken in account.

In this work I give the review of the activation detectors method and I show that some known facts need to be reconsidered in our special case: corrections have to be applied if the activation detectors cannot be approximated as small and thin detectors (attenuation of neutrons in the detector material), most radioisotopes that are found by the gamma analysis are not produced only by neutrons but also by other particles resulting from the spallation, etc. I found with the help of Monte Carlo simulations that the main source of the systematical error during the irradiation is in our case the misplacement of the foils. At most experiments, the measured quantities depend strongly on the position, and the detectors should be placed with the millimeter accuracy to obtain accurate results.

After the irradiation of the activation detectors with neutrons, they are analyzed with the gamma spectrometry method, which is another source of inaccuracies. The calibration of the HPGe detectors is accurate up to few % (in the best case 5%). At closer detector to foil distances, one should count with the misplacement of the foil, which causes another 2-3% inaccuracy, as was shown with simulations. I discuss numerous other corrections which are well understood and controlled, the uncertainties caused by them should not exceed 1-2%. With the uncertainties connected with the fitting of gamma peaks, the total accuracy of the gamma spectrometry method is slightly below 10%.

5.2 Simulations of simple lead target

To obtain the information about the features of the spallation reaction in a simple lead target, the experiment with 660 MeV protons directed to such target was simulated. The setup consisted of a thick, bare, lead target irradiated with an intensive beam of 660 MeV protons and was focused on the neutrons with energies higher than 10 MeV (representing one tenth of all produced neutrons). Small activation detectors were placed around the target to obtain spatial distribution of the produced neutron field, and provided a good set of experimental data for the benchmark tests of the Monte Carlo codes. The transmutation properties of such neutron field was also tested with samples of radioactive iodine ^{129}I .

I implemented the setup in the MCNPX code and performed the simulations. By varying the setup parameters in simulations, the systematic experimental uncertainties of obtained experimental results were estimated to be around 15% with the exception of few particular detectors (detectors

around the 30th cm, the place where the proton beam exits the target due to multiple scattering). I found out that the beam position has the biggest impact on the systematic uncertainties, and should therefore be controlled as precisely as possible in similar experiments. Finally, the studies showed that the experiment provided reliable data about the high energy neutron (proton) production and transport. The results concerning the transmutation properties of ¹²⁹I in high energy neutron field are less accurate, because of geometrical and material uncertainties of the samples.

For the comparison with the simulations, I analysed the experimental data and determined the production rates $B(A)$ in all used activation foils. The analysis, the corrections and the determination of the systematic uncertainties were based on the studies from the spectroscopy part of this work.

I checked the experimental data against the predictions of several spallation models included in the MCNPX code package and the FLUKA code. The codes successfully predict the general trends of the experimental data and with some exceptions also the absolute values. The differences between the codes are minimal in the prediction of the production isotopes with lower threshold, but they become significant for some isotopes with threshold above 30 MeV. From the comparison with experimental data, it seems that the FLUKA code and the INCL4/ABLA models from the MCNPX code describe the neutron/proton spectrum after the 10th cm better than other models included in MCNPX (eg. CEM03). Concerning the total number of produced neutrons in the setup, the calculations by various codes are in good agreement and predict 11.7-12.6 neutrons per one primary proton.

5.3 Simulations of complex setup

Several experiments that were performed on the complex Energy Plus Transmutation setup (a thick, lead target in an uranium blanket, the target-blanket assembly is surrounded with the polyethylene box) provided a large set of experimental data (the analysis of the experimental data was performed by A. Krasa and O. Svoboda). Again, I implemented the setup in the MCNPX code and exploited the simulations to define the systematical uncertainties of the experimental results and provide a deeper understanding of the setup functioning.

I studied the effect of the polyethylene box and found out that the experimental data for higher energies ($E > 10$ MeV) are not influenced (within the accuracy of 5%) by the box (neither by the material of different holders, other construction details, or other detectors). According to simulations, the moderation and scattering of the spallation neutrons in the polyethylene box

5. SUMMARY

is the dominant source of an almost homogenous low energy neutron field ($E < 0.1$ MeV) at the place of the target-blanket assembly. The polyethylene box, which was primarily designed as the biological shielding decreases the number of neutrons emitted to the environment from the target-blanket around 5 times. I recommended the modification of the box (adding the front and back wall and outer cadmium layer) which could reduce the number of emitted neutrons for 20 times and thus improved the shielding function of the box.

With simulations I estimated the systematic uncertainties of obtained experimental data and found that they depend again mostly on the beam and detector displacement - the accuracy used at the experiments means ca. 30% systematic uncertainty in the production rates of the threshold activation detectors.

I also simulated the global parameters of the setup. The number of the produced neutrons per one primary proton and per unit of the beam energy reaches its maximum at around 1 GeV where it is around 30 neutrons per one primary proton. The k_{eff} of the setup was simulated to be 0.202.

I compared the experimental results with the MCNPX and FLUKA (implementation to FLUKA by A. Potapenko) code predictions and showed that the disagreements are within the systematical uncertainties for most experiments (0.7, 1 GeV protons, 1.6, 2.52 GeV deuterons). It seems that INCL4/ABLA models from the MCNPX code and the FLUKA code predict results for activation detectors better than CEM03 model (similar as for the simulations of the spallation on the simple, lead target).

Bibliography

- [1] R.L. Kustom, et al., (2000), An Overview of the Spallation Neutron Source Project, Proc. LINAC2000, 21-25 August 2000, Monterey, California; also White, M. (2002), Spallation Neutron Source, Proc. LINAC2002, 19-23 August 2002, Gyeongju, South Korea.
- [2] G.S. Bauer, et al., *Physica B* **234-236** (1997) 1214-1219.
- [3] H. Ait Abderrahim, et al., Recent Advances in the Design of a Cyclotron-Driven, Intense, Subcritical Neutron Source, Proc of EPAC-96, p. 369
- [4] H.W. Bertini, *Phys.Rev.* **131** (1963) 1801.
- [5] C.D. Bowman, et al, *Nucl. Instr. and Meth. in Phys. Res.* **A 230** (1992) 336-367.
- [6] C. Rubbia, et al., Conceptual design of a fast neutron operated high power Energy Amplifier, CERN/AT/95-44 ET (1995); see also C. Rubbia, A high gain energy amplifier operated with fast neutrons, AIP Conference Proc. 346, Int. Conf. on ADT Technologies and Applications, Las Vegas, 1994.
- [7] R. Klapisch, *Europhysics News* **31** (2000) 26-28.
- [8] "CLEFS CEA - N846 - Printemps 2002", Commissariat Inergie Atomique (CEA), France, 2002.
- [9] Accelerator and Spallation Target Technologies for ADS Applications, A Status Report, Nucl. Sci. ISBN 92-64-01056-4
- [10] T. Stammbach, et al., The Cyclotron as a Possible Driver for an ADS, OECD/NEA Proc. 2nd International Workshop on Utilisation and Reliability of High-Power Proton Accelerators, 22-29 November 1999, Aix-en-Provence, France; and PSI Annual Report, Annex IV, 1998.

BIBLIOGRAPHY

- [11] Fifth framework programme of the European Community for research, technological development and demonstration activities (1998 - 2002), <http://ec.europa.eu/research/fp5/fp5-intro>.
- [12] J. Schlaepfer-Miller, MEGAPIE leads the way to waste transmutation *CERN Courier* (April 2007), 29.
- [13] T. Mukaiyama, Status of Partitioning&Transmutation R&D, and Research Needs for ATW from JAERI Perspective, International Accelerator Transmutation of Waste Workshop, Washington DC, February 17-18 (1999).
- [14] M. Hugon, The EU Research Activities on Partitioning and Transmutation: from The 4th to The 5th Framework Programme, 5th Int. Inf. Exch. Meeting on Partitioning and Transmutation, Ml, Belgium, November 25-27 (1998).
- [15] V. E. Aleksandryan, et al., *Yad. Fiz.* **59** (1996) 592; see also *Phys. At. Nucl.* **59** (1996) 560.
- [16] J. Adam, et al., *J. Nucl. Sci. Technol.* **S2** (2002) 272-275.
- [17] J. Adam, et al., *Kerntechnik* **68** (2003) 214-218.
- [18] W. Westmeier, et al., *Radiochimica Acta* **93** (2/2005) 65-75.
- [19] M.I. Krivopustov, et al., *Kerntechnik* **68** (2003) 48-54.
- [20] S.R. Hashemi-Nezhad, et al., *Nucl. Instr. and Meth. in Phys. Res. A* **591** (2008) 517-529
- [21] F. Křížek, et al, *Czech. J. of Phys.* **56** (2006) 243.
- [22] W. Gudowski, et al., The Subcritical Assembly in Dubna (SAD) Part II: Research program for ADS-demo experiment, *Nucl. Instr. and Meth. in Phys. Res. A* **562** (2006) 887-891.
- [23] Cugnon J, Cascade Models and Particle Production: A comparison, Particle Production in Highly Excited Matter, *NATO Science Series B* **303** (1993) 271-293, ISBN 0-306-44413-5
- [24] Feshbach, et al., *Phys. Rev.* **90** (1953) 166.
- [25] Adair, et al., *Phys. Rev* **94** (1954) 737.
- [26] R. Serber, et al., *Phys.Rev.* **72 N 11** (1947) 1114.

- [27] H.W. Bertini, et al., *Phys.Rev.* **188** (1969) 1711.
- [28] J. Cugnon, *Nucl.Phys.* **A 389** (1982) 191c.
- [29] J. Cugnon, M.-C. Lemaire, *Nucl.Phys.A* **489** (1988) 781.
- [30] *Les annales de la physique* **Vol.25 Nr.2** (2000) 93-113.
- [31] L.W. Dresner, et al., EVAP-A Fortran Program for Calculating the Evaporation of Various Particles from Excited Compound Nuclei, *Report ORNL-TM-196* (1961).
- [32] A.R. Junghans, et al., *Nucl. Phys.* **A 629** (1998) 635.
- [33] J. Barish, et al., Oak Ridge National Laboratory Report *ORNL-TM-7882* (July 1981).
- [34] F. Atchison, et al., Targets for Neutron Beam Spallation Sources, Jul-Conf-34, Kernforschunganlage Julich GmbH, (Jnuary 1980).
- [35] M. B. Chadwick, et al., *Nucl. Sci. and Eng.* **131** Number 3 (March 1999) 293.
- [36] A. J. Koning, et al., *Proceedings of the International Conference on Nuclear Data for Science and Technology*, Santa Fe, USA, (2004) Sep.26-Oct.1.
- [37] M. Blann, et al., International Code Comparison for Intermediate Energy Nuclear Data (Organization for Economic Cooperation and Development Nuclear Energy Agency, Paris, 1994), pp. 1-206.
- [38] Group X-6, MCNPX 2.3.0 - Monte Carlo N-Particle Transport Code System for Multiparticle and high Energy Applications. LANL, Los Alamos, New Mexico (2002).
- [39] R. E. Prael, H. Lichtenstein, User Guide to LCS: The LAHET Code System, LA-UR-89-3014 (September 1989).
- [40] J. F. Briesmeister, Ed. "MCNP - A General Monte Carlo N-Particle Transport Code, Version 4C," LA-13709-M (April 2000).
- [41] M.B. Chadwick, et al., ENDF/B-VII.0: Next Generation Evaluated Nuclear Data Library for Nuclear Science and Technology, *Nuclear Data Sheets* **107** (2006) 2931-3060
- [42] OECD/NEA Data Bank, *JEFF Report* **19** (2005).

BIBLIOGRAPHY

- [43] K. Shibata et al., *J. Nucl. Sci. Technol.* 39 (2002) p. 1125.
- [44] R. E. MacFarlane and R. M. Boicourt, NJOY: A Neutron and Photon Processing System, *Trans. Am. Nucl. Soc.* **22** (1975) 720.
- [45] Y. Yariv and Z. Fraenkel, *Phys. Rev. C* **20** (1979) 2227.
- [46] Y. Yariv and Z. Fraenkel, *Phys. Rev. C* **24** (1981) 488.
- [47] K. K. Gudima, S. G. Mashnik, and V. D. Toneev, *Nucl. Phys* **A401** (1983) 329.
- [48] S.G. Mashnik, et al., *Nucl. Radiochem. Sci.* 6 **2** (2005) A1-A19.
- [49] J. Cugnon et al., *Nucl. Phys.* **A620** (1997) 475.
- [50] R. E. Prael et al., Adaptation of the Multistage Pre-equilibrium Model for the Monte Carlo Method (I), LA-UR-88-3238 (September 1998).
- [51] A. Fasso et al., *CERN-2005-10* (2005) INFN/TC 05/11, SLAC-R-773
- [52] A. Fasso et al., Computing in High Energy and Nuclear Physics 2003 Conference (CHEP2003),
- [53] A. Ferrari, P.R. Sala, *Proc. MC93 Int. Conf. on Monte Carlo Simulation in High Energy and Nuclear Physics, Tallahassee (Florida)*, 22-26 February 1993. Ed. by P. Dragovitsch, S.L. Linn, M. Burbank, World Scientific, Singapore 1994, p. 277-288
- [54] A.J. Koning, S. Hilaire and M.C. Duijvestijn, TALYS-1.0, *Proceedings of the International Conference on Nuclear Data for Science and Technology - ND2007*, April 22-27 2007 Nice France (2008).
- [55] K. van der Meer, et al., *Nucl. Instr. and Meth. in Phys. Res.* **B217** (2004) 202.
- [56] S. Leray et al., *Phys. Rev.* **C65** (2002) 044621.
- [57] G. Gilmore, Practical Gamma-ray Spectroscopy, CHIPS, 2008.
- [58] D.S. Andreew, et al., *Instr. Exp. Tech.* **15** (1972) 1358.
- [59] F. de Corte, *The k_0 -standardization method* (1987) p.75.
- [60] T.M. Semkow, et al., *Nucl. Instr. and Meth. in Phys. Res.* **A290** (1990) 437-444.

- [61] S.Y.F. Chu, et al., WWW Table of Radioactive Isotopes, v.2/28/1999, <http://nucleardata.nuclear.lu.se/nucleardata/toi>.
- [62] K. Siegbahn, Alpha-, beta- and gamma-ray spectroscopy, North-Holland publishing company Amsterdam (1965).
- [63] Vénos Drahoslav, dissertation p.62, personal communication.
- [64] M. Majerle et al., *JINR preprint E15-2008-94* Dubna 2008.
- [65] M. Majerle et al., *JINR preprint E15-2007-72* Dubna 2007.
- [66] M.Abdesselam, et al., *Nucl. Instr. and Meth. in Phys. Res.* **B72** 7.
- [67] H.H.Heckman, et al., *Phys. Rev.* **A36** 3654.
- [68] V. Henzl et al., *J. of Nucl. Sci. and Tech. Supplement 2* (August 2001) p.1248.
- [69] EXFOR: Experimental Nuclear Reaction Data (EXFOR/CSISRS), OECD/NEA Data Bank, <http://www.nea.fr/html/dbdata/x4/welcome.html>.
- [70] ICRU (1993). International Commission on Radiation Units and Measurements. *ICRU Report 49*, Stopping Powers and Ranges for Protons and Alpha Particles.
- [71] M.I. Krivopustov, et al., *JINR Preprint E1-2004-79* Dubna 2004.
- [72] Igor Zhuk - personal communication
- [73] Matthew A. Griffin - personal communication
- [74] A. Krasa, et al., *JINR Preprint E15-2007-081* Dubna 2004.
- [75] M.I. Krivopustov, et al., *JINR Preprint E1-2007-7* Dubna 2004.
- [76] A. Krasa, Dissertation thesis, Czech Technical University in Prague, 2008.

Appendix

Phasotron experiment - experimental values

Table 1: The integral proton flux results from different radioisotopes produced in Al and Cu foils.

	Isotope	σ [mbarn]	$\Delta\sigma/\sigma$ [%]	I_p [10^{15} protons]
Copper foils				
1	^{55}Co	1.51	6	1.46 ± 0.09
2	^{56}Co	9.4	10	1.57 ± 0.16
3	^{57}Co	25.0	8	1.67 ± 0.13
4	^{58}Co	30	15	1.64 ± 0.25
5	^{60}Co	11.0	15	1.92 ± 0.29
6	^{52}Mn	9.6	6	1.40 ± 0.08
7	^{54}Mn	19.7	7	1.69 ± 0.12
8	^{57}Ni	0.99	8	1.56 ± 0.12
9	^{52}Fe	0.210	8	1.61 ± 0.13
10	^{59}Fe	1.65	10	1.75 ± 0.18
11	^{51}Cr	22.6	6	1.75 ± 0.11
12	^{48}V	10.7	6	1.51 ± 0.09
13	^{44m}Sc	3.63	6	1.78 ± 0.11
14	^{46}Sc	5.0	8	1.71 ± 0.14
15	^{47}Sc	2.29	8	1.64 ± 0.13
16	^{48}Sc	0.460	6	1.91 ± 0.11
17	^{42}K	1.69	6	1.74 ± 0.10
18	^{43}K	0.65	6	1.88 ± 0.11
Aluminium foils				
19	^7Be	5.37	7	1.23 ± 0.09
20	^{22}Na	14.5	8	1.30 ± 0.10

APPENDIX

Table 2: Experimental production rates in the Au foils along the target. $X[\text{cm}]$ is the distance of the foil center from the beginning of the target. The production rates $B(A)[\text{g}^{-1} \text{proton}^{-1}]$ are multiplied with 10^8 .

$X[\text{cm}]$	^{198}Au	^{196}Au	^{194}Au	^{193}Au	^{192}Au	^{191}Au
1	1453 ± 5	508.9 ± 2.9	125.5 ± 2.3	58.2 ± 1.1	54.2 ± 0.6	26.9 ± 0.7
3	1494 ± 9	565 ± 3	155 ± 3	71.5 ± 1.2	74.5 ± 0.9	36.8 ± 0.9
5	1548 ± 11	575 ± 5	164 ± 3	85.7 ± 1.3	84.4 ± 1.2	40.3 ± 1.2
7	1508 ± 16	535 ± 8	168 ± 4	98.2 ± 1.4	91.9 ± 1.2	42.3 ± 1.4
9	1618 ± 6	516.4 ± 2.3	162.5 ± 2.7	84.5 ± 1.1	87.3 ± 2.1	46.3 ± 1.5
11	1501 ± 17	465 ± 7	151 ± 4	92.4 ± 1.7	86.9 ± 0.9	42.3 ± 1.1
13	1434 ± 9	434 ± 3	137 ± 3	78.1 ± 1.2	81.0 ± 1.0	42.0 ± 1.3
15	1352 ± 13	387 ± 3	133 ± 4	86.7 ± 1.5	73.3 ± 0.6	47.0 ± 1.4
17	1353 ± 9	356.3 ± 2	120 ± 3	70.9 ± 1.2	83.7 ± 1.5	34.6 ± 1.1
19	1377 ± 9	314 ± 4	110.2 ± 2.9	75.7 ± 1.5	69.5 ± 0.7	39.6 ± 1.4
21	1341 ± 7	279.3 ± 1.7	102.9 ± 2	61.0 ± 1.0	82.3 ± 0.8	32.9 ± 0.9
23	1251 ± 13	235 ± 3	88 ± 3	60.0 ± 1.1	71.0 ± 1.9	48.6 ± 1.5
25	1168 ± 7	201.0 ± 1.7	81.2 ± 2.3	64.0 ± 1.2	58.4 ± 1.3	36.9 ± 0.8
27	1060 ± 8	171.1 ± 1.9	77.1 ± 2.7	71.4 ± 1.7	83.4 ± 0.8	42.7 ± 2
29	1056 ± 10	140.5 ± 0.9	71.5 ± 2.1	65.5 ± 1.4	104.0 ± 1.1	57.0 ± 1.4
31	1018 ± 11	105.0 ± 1.3	48.9 ± 2.4	54.3 ± 0.9	66.8 ± 0.7	41.0 ± 1.4
33	1039 ± 10	63.2 ± 0.4	28.1 ± 1.1	24.9 ± 0.5	38.3 ± 0.4	17.0 ± 0.4
35	1048 ± 6	42.1 ± 0.5	19.7 ± 1.1	15.2 ± 0.4	16.3 ± 0.23	11.1 ± 0.6
37	1060 ± 5	27.4 ± 0.3	14.1 ± 0.7	8.1 ± 0.4	9.65 ± 0.14	6.0 ± 0.4
39	1076 ± 4	21.0 ± 0.4	11.8 ± 1.6	9.3 ± 0.6	8.34 ± 0.2	4.7 ± 0.6
41	1101 ± 3	17.1 ± 0.4	9.4 ± 0.7	5.7 ± 0.5	5.5 ± 0.3	3.7 ± 0.6
43	1169 ± 3	14.6 ± 0.5	9.1 ± 0.9	5.7 ± 0.5	5.06 ± 0.17	2.5 ± 0.5
45	1086 ± 3	12.0 ± 0.4	6.9 ± 0.6	4.5 ± 0.4	4.47 ± 0.14	1.9 ± 0.5

Table 3: Experimental production rates in the Al and Bi foils along the target. X[cm] is the distance of the foil center from the beginning of the target. The production rates $B(A)[\text{g}^{-1} \text{proton}^{-1}]$ are multiplied with 10^8 .

X[cm]	^{24}Na	^{206}Bi	^{205}Bi	^{204}Bi	^{203}Bi	^{202}Bi	^{201}Bi
1	255.9 ± 1.3	124.5 ± 0.4	84.8 ± 0.9	51.3 ± 0.2	35.2 ± 0.3	21.68 ± 0.23	11.1 ± 0.4
3	300.16 ± 1.2						
5	304.7 ± 1.6						
7	305.16 ± 1.3						
9	279.6 ± 1.5	155.2 ± 0.8	120.3 ± 1.5	78.8 ± 0.3	56.3 ± 0.5	39.9 ± 0.4	21.2 ± 0.5
11	263.8 ± 1.1						
13	240.4 ± 1.2						
15	218.9 ± 0.9						
17	192.8 ± 1.0						
19	173.9 ± 0.8						
21	154.5 ± 0.8	103.6 ± 0.6	85.7 ± 1.0	59.07 ± 0.25	46.6 ± 0.4	35.0 ± 0.4	20.3 ± 0.6
23	139.6 ± 0.6						
25	116.9 ± 0.8						
27	102.8 ± 0.5						
29	82.5 ± 0.5						
31	59.8 ± 0.3	61 ± 0.3	75.8 ± 1.2	63.93 ± 0.28	54.3 ± 0.5	46.8 ± 0.5	23.5 ± 0.6
33	36.29 ± 0.26						
35	24.6 ± 0.18						
37	16.35 ± 0.16						
39	12.4 ± 0.12						
41	9.96 ± 0.10						
43	8.22 ± 0.09	7.59 ± 0.05	6.41 ± 0.15	4.305 ± 0.028	3.69 ± 0.05	3.04 ± 0.09	1.80 ± 0.18
45	7.06 ± 0.09						

Table 4: Experimental production rates in the iodine samples. The production rates $B(A)[\text{g}^{-1} \text{proton}^{-1}]$ are multiplied with 10^8 .

9 th cm	^{127}I	^{129}I
^{130}I		269.3 ± 0.4
^{128}I	349.2 ± 1.7	158.2 ± 1.6
^{126}I	287.4 ± 0.8	111.5 ± 2.3
^{124}I	77.5 ± 0.4	39 ± 3
^{123}I	59.96 ± 0.23	32.04 ± 0.22
^{121}I	17.0 ± 0.10	9.18 ± 0.14
^{120}I	9.54 ± 0.19	9.1 ± 2.1
^{119}I	4.31 ± 0.11	2.39 ± 0.24
^{118}I	1.37 ± 0.07	
21 st cm	^{127}I	^{129}I
^{130}I		368.0 ± 0.5
^{128}I	220.0 ± 1.2	250 ± 3
^{126}I	160.0 ± 0.4	157.9 ± 2.1
^{124}I	51.3 ± 0.4	53 ± 4
^{123}I	47.09 ± 0.17	36.9 ± 0.4
^{121}I	14.22 ± 0.07	8.86 ± 0.19
^{120}I	9.81 ± 0.18	7 ± 4
^{119}I	4.4 ± 0.10	2.5 ± 0.5
^{118}I	1.73 ± 0.07	

EPT experiment with 1 GeV protons - experimental values

Table 5: Experimental production rates in the gold foils. The production rates $B(A)$ are multiplied with 10^8 .

rad. distance	isotope	front	1 st gap	2 nd gap	3 rd gap	back
3 cm	Au-196		2017 ± 17			
	Au-194		609 ± 8			
	Au-193		586 ± 27			
	Au-192		411 ± 16			
	Au-191		188 ± 19			
6 cm	Au-196	437 ± 6	772 ± 9	422 ± 8	212 ± 6	75.3 ± 2.8
	Au-194	92.6 ± 2.2	212 ± 5	133 ± 4	71.5 ± 2.6	33.4 ± 1.7
	Au-193	57 ± 7	172 ± 10	102 ± 12	62 ± 8	29 ± 7
	Au-192	37.7 ± 1.8	110 ± 3	72 ± 4	41.1 ± 2.3	20.3 ± 1.6
	Au-191	13 ± 4	46 ± 6	44 ± 6	25 ± 4	11 ± 2.8
8.5 cm	Au-196		389 ± 7			
	Au-194		113 ± 3			
	Au-193		89 ± 13			
	Au-192		51.2 ± 2.5			
	Au-191		27 ± 5			
10.7 cm	Au-196		239 ± 7			
	Au-194		70 ± 3			
	Au-193		67 ± 16			
	Au-192		33 ± 2.2			
	Au-191		23 ± 6			